GRACE 327-750

Gravity Recovery and Climate Experiment

Product Description Document for AOD1B Release 06

(Rev. 6.1, October 19, 2017)

Henryk Dobslaw, Inga Bergmann-Wolf, Robert Dill,
Lea Poropat, Frank Flechtner

GFZ German Research Centre for Geosciences
Department 1: Geodesy

Contents

Document Changes Log

Issue	Date	Section	Description of Change
3.1	Apr 13, 2007		Last version that describes Releases 00 – 04 in full detail.
4.4	Dec 14, 2015		Last version that describes Release 05 in full detail as well as the various GAx Level-2 products required to account for offsets in AOD1B introduced by several ECMWF model changes.
6.0	Dec 8, 2016		Fully revised document version describing Release 06.
6.1	Oct 19, 2017	1.1	Citation to reference paper for Release 06 added.
		3.3	Clarification of post-processing sequence for ocean bottom pressure.
		5.1	Clarification: annual modulations are considered for S_1, S_2, and S_3; whereas monthly modulations are considered for M_2.
		5.1	Relation between mean solar time t and mean lunar time τ at Greenwich added.
		7.3	Clarification: GLO coefficients are obtained from adding ATM and OCN at coefficient level.
		8	New chapter on user recommendations added.
		A	Download link for non-tidal coefficients added.
		B	Download link for tidal coefficients added.

Chapter 1

Introduction

1.1 Overview on AOD1B Release 06

The Atmosphere and Ocean De-Aliasing Level-1B (AOD1B) product provides a priori information about temporal variations in the Earth's gravity field caused by global mass variability in atmosphere and ocean. It is based on analysis and forecast data out of the operational high-resolution global numerical weather prediction (NWP) model from the European Centre for Medium-Range Weather Forecasts (ECMWF) and ocean bottom pressure from an unconstrained simulation with the global ocean general circulation model MPIOM (Jungclaus *et al.*, 2013) that is consistently forced with ECMWF atmospheric data.

AOD1B provides fully normalized Stokes coefficients (Heiskanen & Moritz, 1967) of the anomalous external gravity field of the Earth caused by the mass variability predicted from those numerical models. It contains four different sets of coefficients: The effect of the atmosphere (**ATM**) that includes the contribution of atmospheric surface pressure over the continents; the static contribution of atmospheric pressure to ocean bottom pressure elsewhere; and the much weaker contribution of upper-air density anomalies above both continents and oceans. Further, the dynamic ocean contribution to ocean bottom pressure (**OCN**) is provided, and the sum of ATM and OCN are given as the so-called **GLO** coefficients, which are typically applied as a background model in precise orbit determination. For particular oceanographic applications, a fourth set of coefficients **OBA** is additionally included, which is zero over the continents and provides the simulated ocean bottom pressure that includes air and water contributions elsewhere. Thus, OBA deviates from GLO over the ocean domain only by disregarding the small contribution of upper-air density anomalies to the external gravity field. All anomalous signals given in AOD1B refer to corresponding long-term mean fields empirically estimated over the period 2003 – 2014 that approximately matches the length of one full solar cycle.

The AOD1B product has a temporal sampling of 3 hours. Starting on Jan 1st, 1976, atmospheric and oceanic pressure anomalies are expanded into Stokes coefficients up to degree and order (d/o) 100 to allow for a consistent processing of LAGEOS and all other geodetic satellite missions equipped with laser retro-reflectors. Since January 1st, 2000, AOD1B is expanded to d/o=180 and considers the gravitational effects of upper-air density anomalies in addition to the atmospheric surface pressure variability to account for the higher orbit accuracy requirements for low-Earth orbiting satellite missions specifically designed to observe various aspects of the Earth's gravity field, most notably the CHAMP (Reigber *et al.*, 2002), GRACE (Tapley *et al.*, 2004), and GOCE (Rummel *et al.*, 2011) missions.

Periodic signals related to tides in the atmosphere and its corresponding oceanic response have been empirically estimated and removed from the non-tidal time-series of AOD1B RL06. This includes

the solar tides S_1, S_2, and S_3, and additionally the main lunar semi-diurnal tide M_2, each together with two side-bands to account for potential modulations. It is suggested to treat atmospheric tides in precise orbit determination in a similar manner as tides in the ocean and solid Earth, and the tidal signals removed are therefore provided as separate sets of coefficients (Appendix B).

The non-tidal AOD1B coefficients are routinely updated every day and all files are made available via the GRACE data archives. Up-to-date information on AOD1B is provided via the web-page http://www.gfz-potsdam.de/en/esmdata. The current release of AOD1B has been extensively validated by means of in situ ocean bottom pressure observations and high-pass filtered satellite altimetry-based sea-level anomalies. Details are provided in the following research article that should also be used for referencing AOD1B:

- Dobslaw, H., Bergmann-Wolf, I., Dill, R., Poropat, L., Thomas, M., Dahle, C., Esselborn, S., König, R., Flechtner, F. (2017). A New High-Resolution Model of Non-Tidal Atmosphere and Ocean Mass Variability for De-Aliasing of Satellite Gravity Observations: AOD1B RL06. Geophys. J. Int., 211, 263–269.

1.2 Relevance of AOD1B for Satellite Gravimetry

Gravity field determination from low Earth-orbiting satellites is generally affected by time-changes in the external gravitational field and its underlying mass distribution within the atmosphere, at the surface, and in the Earth's interior. Due to sampling limitations of polar-orbiting satellite missions, observations are typically accumulated over a certain time-period in order to be able to solve for a global gravity field solution with reasonably high spatial resolution. For the GRACE mission, typical accumulation times range between 7 and 30 days.

Besides tidal signals that are particularly present in the oceans and in the solid Earth, there are also substantial non-tidal mass variations at periods below 30 days that take place in the vicinity of the Earth's surface. Evolving synoptic weather systems with horizontal dimensions of several 100 km that are advected with the mean flow cause surface pressure changes of a few ∼10 hPa at moderate latitudes. Heavy precipitation events associated with convective processes might cause occasionally a rapid increase of the amount of water stored on the continents, and surface winds associated with cyclonic pressure systems lead to a redistribution of oceanic water masses, and thus changes in ocean bottom pressure.

Failure to account for those high-frequency signals within the gravity field retrieval process causes temporal aliasing of such signals into the estimated monthly-mean gravity fields, a process that contributes to the systematic meridional striations common to all un-regularized GRACE gravity field solutions. Although this high-frequency variability is also affecting gravity field models from CHAMP and GOCE satellite observations, the GRACE mission, dedicated to the observation of time-variable mass transport phenomena, is particularly affected up to intermediate spatial wavelengths of several ∼100 km.

Satellite gravimetry is set apart from all other currently operating satellite remote sensing systems by the fact that it is not only sensitive to the atmospheric composition or some surface properties of the Earth, but to changes in the global mass distribution independently of its surface exposure. GRACE is therefore able to provide quantitative estimates of in particular water mass anomalies in all possible storage compartments including surface water, snow pack, continental ice, soil moisture, and the deep aquifers. At the same time, GRACE is inherently insensitive to discriminate vertically between those storages: in order to separate between mass anomalies in the atmosphere and underneath, prior information on atmospheric mass variability is required.

To meet those two purposes – the removal of high-frequency mass variability to avoid temporal aliasing, and the provision of prior information on atmospheric mass variability to allow for signal separation over the continents – AOD1B should fulfill the following minimal requirements:

- AOD1B needs to be provided with very high temporal and spatial resolution to properly represent transient atmospheric weather systems and their associated pressure and mass signatures.
- AOD1B needs to be stable on long time-scales from years to decades in order to avoid the introduction of spurious low-frequency signals or discontinuities into the GRACE gravity fields that are subsequently prone to be interpreted errorneously in an entirely different geophysical context.

1.3 History of Available AOD1B Releases

Release 00 of AOD1B is available for the period July 2000 until April 2003 and incorporates operational ECMWF analysis data and ocean bottom pressure simulated with the barotropic ocean model PPHA (Hirose *et al.*, 2001). Only the combined effect of atmospheric and oceanic mass variability is provided, and a mean field calculated over the year 2001 has been subtracted. Signals from atmospheric tides and the simulated oceanic response are fully retained in those coefficients.

Release 01 is available for the period July 2000 until June 2007 and is identical with release 00 except for the fact that separate coefficients for atmosphere and ocean are now provided.

Release 02 consists of a short test series of ocean bottom pressure from an improved version of PPHA that has been calculated for only eight selected months within the period May 2003 until January 2005. The signature of the atmospheric tide S_2 has been removed from the surface pressure grids based on a climatology provided by Ray & Ponte (2003) before forcing PPHA in order to avoid a double book-keeping of the oceanic S2 which is also part of the ocean tide background model typically applied in the GRACE orbit determination. The S_2 signal in the atmosphere, however, is still included in the 6 hourly coefficients, even though it is partially aliased into a standing wave pattern. All anomalies given in AOD1B RL02 do now refer to mean values estimated over the period 2001 – 2002.

Release 03 is based on an early simulation with an OMCT configuration discretized on a 1.875° latitude-longitude grid (Thomas & Dobslaw, 2004). The ocean simulation also predicts seasonal variations in total ocean mass and thus barystatic sea-level changes during 2002 – 2004, which have been found to be less reliable when compared to observations. Since January 1st, 2005, total ocean mass in RL03 is therefore fixed to a constant at all time-steps. Users of GRACE gravity fields from GFZ RL03 and JPL RL02 are referred to GRACE Technical Note #4 (Bettadpur *et al.*, 2006) for further information. Release 03 AOD1B is available until January 2007.

A first long-term simulation from OMCT with updated momentum transfer parameterization is the basis for AOD1B **release 04** (Dobslaw & Thomas, 2007). OMCT has been forced with ERA-40 atmospheric re-analysis data (Uppala *et al.*, 2005) for the time-period January 1976 until December 2000, followed by simulations forced with operational ECMWF analyses so that it is also suitable for the consistent re-processing of historical satellite laser ranging observations (Flechtner *et al.*, 2008). The product contains for the first time an additional set of coefficients of ocean bottom pressure variability (OBA) that disregards the contribution of upper-air density anomalies for oceanographic applications. The mean fields removed are once more calculated from the years 2001 and 2002. Release 04 has been processed until April 2012.

The **release 05** was introduced in 2012. The series is based on OMCT discretized on a 1.0° latitude-longitude grid (Dobslaw *et al.*, 2013), that has been integrated with ERA-Interim reanalysis data (Dee *et al.*, 2011) for the time-period January 1979 to December 2000, followed by simulations forced with operational ECMWF analyses. The atmospheric data processing has not been changed since release 04. Corresponding mean fields calculated over the years 2001 – 2002 are once more subtracted. Until release 05, all versions of AOD1B have 6 hourly temporal resolution and are expanded up to d/o = 100. Release 05 is available until the end of the year 2017.

The present document is describing AOD1B **release 06** that was introduced in the year 2016 (Dobslaw *et al.*, 2017). For further information on older versions of AOD1B, please refer to the revisions 4.4 (for release 05) and 3.1 (for releases 01 to 04) of the AOD1B Product Description Document that are still available from the GRACE archives.

Chapter 2

Atmospheric Surface Pressure Variability

2.1 Atmospheric Data-Sets Available from ECMWF

The atmospheric component of AOD1B is based on operational and re-analysis data from the ECMWF. The latest re-analyses available that cover our period of interest are ERA-40 (Uppala *et al.*, 2005) for 1976 – 1978, and ERA-Interim (Dee *et al.*, 2011) since 1979. Operational NWP data-sets are available for the whole time-period as well, but their quality is drastically improving in particular in the most recent years due to increased spatial resolution, improved representation of physics in the model, and tremendous progress in data assimilation due to the computing ressources available today.

Analysis data is assumed to be the most precise representation of the state of the atmosphere, but it is typically disseminated every 6 hours only. In order to provide AOD1B at 3 hourly resolution, we make use of short-term forecasts that are available with 3 hourly sampling from the re-analyses, and even hourly sampling for the most recent years of the operational ECMWF forecasts. The combination between analysis and forecasts is performed as suggested by Dobslaw & Thomas (2005).

In the following sections, only the contribution of atmospheric surface pressure to changes in the external gravity field of the Earth is considered. Effects of density anomalies in upper-air layers of the atmosphere are calculated separately as described in Ch. 4.

2.2 Reduction of Pressure to Reference Orography

Atmospheric pressure decreases with altitude. As a rule of thumb, surface pressure at mean sea-level changes by 1 hPa – which approximately corresponds to 1 cm equivalent water height – every 8 m. Thus, atmospheric surface pressure from different numerical models need to refer to the same geopotential height before it can be compared to each other or combined into one time-series.

For the reduction of atmospheric surface pressure to a reference orography, we make use of ECMWF's sea-level pressure diagnostic that has been kindly made available in form of a set of FORTRAN routines, that we have adapted in order to run it independently of ECMWF's Integrated Forecast System (IFS). Within those routines, mean sea-level pressure p_{msl} is calculated as follows (Yessad, 2015):

$$p_{\mathrm{msl}} = p_s \exp\left\{\frac{\Phi_s}{R_d T_s}\left[1 - \frac{\alpha\Phi_s}{2R_d T_s} + \frac{1}{3}\left(\frac{\alpha\Phi_s}{R_d T_s}\right)^2\right]\right\}. \tag{2.1}$$

Here, p_s is atmospheric surface pressure, Φ_s is the surface geopotential, R_d is the gas constant for dry air, and T_s the surface virtual temperature extrapolated from the lowest model level nlev according to

$$T_s = T_{\mathrm{nlev}} + \alpha T_{\mathrm{nlev}}\left(\frac{p_s}{p_{\mathrm{nlev}}} - 1\right), \tag{2.2}$$

with a temperature reduction factor α,

$$\alpha = \Gamma R_d / g_{\mathrm{WMO}}, \tag{2.3}$$

where $\Gamma = 6.5$ K/km is the standard temperature lapse rate, and $g_{\mathrm{WMO}} = 9.80665$ m/s^2 the standard gravity acceleration according to the definitions of the World Meteorological Organization. Both surface temperatures and the temperature lapse rate are slightly modified for altitudes above 2000 m and extreme surface temperatures in order to avoid extrapolation to too low pressures over high and warm surfaces, and also to too high pressures over very cold surfaces; the details are given in Yessad (2015).

In addition to reducing atmospheric surface pressure to mean sea-level, the algorithm is generally applicable to extrapolate pressure vertically to arbitrary heights. For AOD1B RL06, the orography of IFS version 41r1 – which was in operation at ECMWF between May 12th, 2015 and March 8th, 2016 – is chosen as a reference orography, where all surface pressure data-sets are reduced to. In case that this reference orography is locally higher than the model orography, pressure is interpolated from the nearest model levels that are obtained from integrating virtual temperatures and thus geopotential heights vertically upwards.

To demonstrate the efficacy of our approach, analysis data over 14.5 years of surface pressure out of both the operational ECMWF weather prediction model and ERA-Interim have been mapped to a common reference orography (Dobslaw, 2016). Relative biases and residual variability between both data-sets are reduced by about one order of magnitude, thereby allowing to achieve a consistency among both data-sets at the level of about 1 hPa. Remaining differences rather reflect temperature biases and also resolution limitations of the re-analysis data-set, but are not anymore related to the local roughness in orography or to changes in the spatial resolution of the operational model. The analysis of yearly biases between ECMWF and ERA-Interim revealed best coincidence in the year 2007 (see Tab. 1 of Dobslaw, 2016). Since moreover ERA-Interim uses the IFS cycle 31r2 – which has been in operations at ECMWF between Dec 12th, 2006 and June 5th, 2007 – we decided to use ECMWF operational data for AOD1B only from January 1st, 2007 onwards, and rely on ERA-Interim re-analysis data for all previous years.

2.3 ECMWF Model Changes Relevant for AOD1B

As discussed above, operational model data from ECMWF is used to compute AOD1B RL06 coefficients from January 1st, 2007 onwards. At this time, cycle 31r2 was in operation, wheras at the time of publication of AOD1B RL06 it was already cycle 41r2. A full documentation of changes to the operational NWP model from ECMWF is available from `www.ecmwf.int/en/forecasts/documentation-and-support/changes-ecmwf-model` and we briefly mention a subset of modifications only that are most relevant for AOD1B.

- **January 1st, 1976**: ERA-40 is used to process the AOD1B coefficients. It utilizes cycle 23r4 of the IFS with a spectral T159 spatial resolution and 60 vertical sigma layers. Analysis data is obtained from four 3D-Var assimilation windows with a length of six hours each day.
- **January 1st, 1979**: ERA-Interim is introduced that utilizes IFS cycle 31r2 with a spectral T255 model (∼79 km) with again 60 sigma levels in the vertical. A twelve-hour 4D-Var assimilation window is used in this re-analysis.
- **January 1st, 2007**: Operational ECMWF data is employed for AOD1B RL06 for the first time. Cycle 31r2 with a horizontal resolution of T799 (∼25 km) is used, the vertical resolution is 91 sigma levels. Data assimilation is still based on 12-hourly 4D-Var windows.
- **January 26th, 2010**: Cycle 36r1 increases the horizontal resolution towards T1279 (∼16 km).
- **June 25th, 2013**: Cycle 38r2 increases the vertical resolution to 137 levels, the horizontal resolution remains unchanged.
- **May 12th, 2015**: Cycle 41r1 introduces a fully revised surface orography at an otherwise unchanged horizontal and vertical resolution.
- **March 8th, 2016**: Introduction of the new octahedral horizontal grid O1280 (∼8 km). The vertical resolution remains at 137 levels.

2.4 Static Contribution of the Atmosphere to Ocean Bottom Pressure

Ocean-bottom pressure is commonly regarded as the summarized effect of the hydrostatic pressure from both the atmospheric and oceanic masses situated along the plumb line above a certain position of the sea-floor. For the representation of global bottom pressure in model data-sets, those masses are traditionally separated into an atmospheric and an oceanic contribution. The local sea-surface, however, reacts rapidly to changes in atmospheric surface pressure. As evidenced from the analysis of global sea-level variations observed with satellite altimetry, the ocean is adjusting almost perfectly to surface pressure changes at periods of a few days and longer (Wunsch & Stammer, 1997). Thus, atmospheric and oceanic contributions to ocean-bottom pressure are highly anti-correlated, and largely cancel each other when summarized.

To remove the correlation between the atmospheric and oceanic components of ocean-bottom pressure, we only include the static contribution to ocean bottom pressure into the ATM coefficients. Technically, this implies replacing the surface pressure at every grid point over the oceans with the area-mean surface pressure averaged over the whole ocean domain as defined by the AOD1B land-sea mask:

$$p'_s(\theta,\phi) = \begin{cases} p_s(\theta,\phi) & \text{at the continents} \\ \dfrac{1}{A_{\text{Oceans}}} \iint\limits_{\text{Oceans}} p_s(\theta,\phi)\,dA & \text{over the oceans} \end{cases} \tag{2.4}$$

The C_{00} estimates of ATM are not affected by this inverse-barometric (IB) correction, but the temporal variability of several low-degree spherical harmonics reduces substantially. Note that tidal signals in the atmosphere at S_1, S_2, S_3, and M_2 frequencies and their associated modulations have been estimated and subtracted prior to the replacement of pressure with its area-mean value over the oceans. Further details on the handling of atmospheric tides in AOD1B are provided in Ch. 5.

2.5 Atmospheric Surface Pressure Contributions to the Time-Variable Gravity Field

Fundamentals

We rely in the following on the formalism of Boy & Chao (2005) that itself builds on previous work of Wahr *et al.* (1998) and Swenson & Wahr (2002). The time-variable external gravity field of the Earth as expressed in terms of deviations in geoid height $\Delta\xi(\theta,\phi)$ from a certain reference state can be conveniently expanded in spherical harmonics:

$$\Delta\xi(\theta,\phi) = a_{45}\sum_{l=0}^{\infty}\sum_{m=0}^{l}\tilde{P}_{lm}(cos\theta)\{\Delta C_{lm}\cos m\phi + \Delta S_{lm}\sin m\phi\} \tag{2.5}$$

Here, a_{45} is the Earth's mean radius, θ is colatitude, ϕ longitude, $\tilde{P}_{lm}$ are normalized associated Legendre Functions, and ΔC_{lm}, ΔS_{lm} are dimensionless Stokes coefficients. Note that the time-dependency of ΔC_{lm}, ΔS_{lm} and $\Delta\xi$ has been omitted to improve readability. The Stokes coefficients are related to anomalies in the Earth's density distribution:

$$\Delta C_{lm} = \frac{3}{4\pi a_{45}\rho_E}\frac{1}{2l+1}\int_0^{2\pi}\int_0^{\pi}\Delta I_l(\theta,\phi)\tilde{P}_{lm}(\cos(\theta))\cos m\phi\,\sin\theta\,d\theta d\phi \tag{2.6}$$

$$\Delta S_{lm} = \frac{3}{4\pi a_{45}\rho_E}\frac{1}{2l+1}\int_0^{2\pi}\int_0^{\pi}\Delta I_l(\theta,\phi)\tilde{P}_{lm}(\cos(\theta))\sin m\phi\,\sin\theta\,d\theta d\phi \tag{2.7}$$

where ρ_E is the average density of the Earth, and ΔI_l denotes the change in the so-called "inner integral" over all masses in the Earth System in radial direction:

$$\Delta I_l(\theta,\phi) = \int_0^{\infty}\left(\frac{r}{a_{45}}\right)^{l+2}\Delta\rho(r,\theta,\phi)dr \tag{2.8}$$

with $\Delta\rho(r,\theta,\phi)$ denotes a density anomaly at a certain height r which might reside anywhere between the center of the Earth at $r = 0$ and the top of the atmosphere.

Radial Coordinates

The radial coordinate r of eq. 2.8 for a given mass element is taken in the following as the sum of the ellipsoidal radius $a(\theta)$, the geoid height ξ, the orthometric height of the orography h, and the orthometric height of any point above the orography $z = h + \delta r$ (Fig. 2.1):

$$\begin{aligned} r(\theta,\phi) &= a(\theta) + \xi(\theta,\phi) \quad + h(\theta,\phi) + \delta r(\theta,\phi) \\ &= a(\theta) + \xi(\theta,\phi) \qquad\qquad + z(\theta,\phi) \end{aligned} \tag{2.9}$$

For the calculation of AOD1B, the (time-invariant) geoid undulations ξ are entirely omitted since those vary globally only in the range of ±120 m. The ellipsoidal radius $a(\theta)$ is calculated from the current reference ellipsoid given in the IERS conventions 2010 (Petit & Luzum, 2010), and orthometric heights z are derived from the reference orography introduced above by means of a transformation from geopotential heights H as given by Boy & Chao (2005):

$$z = (1 - 0.002644\,\cos 2\theta)H + (1 - 0.0089\,\cos 2\theta)\frac{H^2}{6.245\cdot 10^6} \tag{2.10}$$

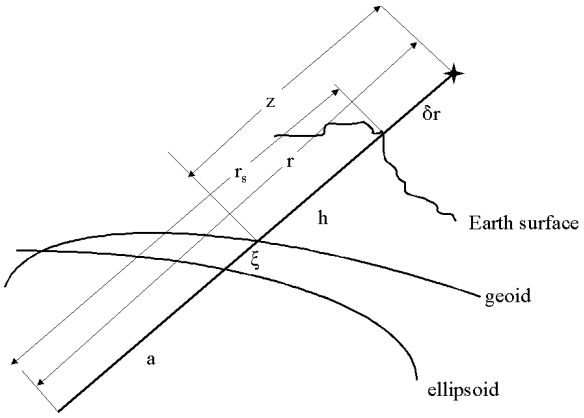

Figure 2.1: Radial coordinates employed to characterize the vertical position of pressure and density anomalies that contribute to the time-variable Earth's gravity field: ellipsoidal radius a, geoid height ξ, orthometric height of the surface of the orography h, and the orthometric height of any point above the orography $z = h + \delta r$.

Spatially Variable Gravity

In atmospheric modelling, the gravitational acceleration g is typically set to a constant value as defined by the World Meteorological Organzation (WMO):

$$g_{\mathrm{WMO}} = 9.80665\ m/s^2 \tag{2.11}$$

In the calculation of AOD1B, we employ normal gravity $g(\theta, z)$ based on the GRS80 reference system as defined in the IERS conventions (Petit & Luzum, 2010) with

$a_0 = 6378136.6\ m$ semi-major axis, and
$1/f = 298.25642$ flattening factor.

The mean radius of the Earth a_{45} introduced above is taken as the corresponding ellipsoidal radius at 45° latitude.

Thin-Layer Approximation to the Inner Integral

In the simplest case, all mass variability in the Earth's system that causes changes in the gravity field is concentrated within a shell of infinite thickness so that it can be characterized by a surface pressure anomaly. In that case, eq. 2.8 simplifies to (Swenson & Wahr, 2002):

$$I_l(\theta,\phi) = \Big(\frac{a(\theta)+h(\theta,\phi)}{a_{45}}\Big)^{l+2} \int_{\text{thin layer}} \rho dr = \Big(\frac{a(\theta)+h(\theta,\phi)}{a_{45}}\Big)^{l+2} \frac{\Delta p_s(\theta,\phi)}{g(\theta,z)}, \tag{2.12}$$

which only depends on the surface pressure anomaly $\Delta p_s(\theta,\phi)$, the vertical position of that anomaly $a(\theta) + h(\theta,\phi)$ and the corresponding gravity acceleration.

Numerical Implementation

The inner integral of eq. 2.12 is obtained from atmospheric surface pressure anomalies after mapping to a common reference orography, de-tiding, replacement of pressure at ocean grid points with its area-mean value, and subtraction of a long-term mean field as derived from the period 2003 – 2014. This (degree-dependent) field is regarded as a quasi-continuous function $f(\theta, \phi)$ on the sphere which is subsequently expanded into fully normalized spherical harmonic coefficients with the algorithm published by Wang *et al.* (2006):

$$f_{lm} = \int_{\sigma} f(\theta, \phi)\, Y^*(\theta, \phi)\, d\sigma \tag{2.13}$$

where (θ, ϕ) are colatitude and longitude and $Y^*(\theta, \phi)$ the conjugate complex surface spherical harmonics of degree l and order m:

$$Y^*_{lm}(\theta, \phi) = (-1)^m \sqrt{\frac{2\,l+1}{4\,\pi}\frac{(l-m)!}{(l+m)!}}\, P_{lm}(\cos\theta)\, e^{im\phi} \tag{2.14}$$

The approach is suitable to analyse non-smooth data with discontinous slopes that are discretized on equal-angular or Gaussian grids. Discontinuities in surface pressure anomalies may in particular occur in regions of mountain ridges or at the coastlines, so that the method is well suited for our purposes.

The data have to be given in a defined domain of $\theta_a \le \theta \le \theta_b$ and $\phi_a \le \phi \le \phi_b$ and the grid is equally spaced in longitude and latitude direction with the sampling intervals $\Delta\theta$ and $\Delta\phi$. The grid cells are defined by the node rows from 0 at $\theta = \theta_a$ to $i_{\max}$ at $\theta = \theta_b$ and the node columns from 0 at $\phi = \phi_a$ to $j_{\max}$ at $\phi = \phi_b$. Equation 2.13 is then discretized as follows:

$$f_{lm} = \sum_{i=1}^{i_{\max}} \sum_{j=1}^{j_{\max}} \int_{\sigma_{ij}} f(\theta, \phi)\, Y^*_{lm}(\theta, \phi)\, d\sigma \tag{2.15}$$

The values of $f(\theta, \phi)$ for a specific grid cell are obtained from a bilinear function:

$$f(\theta, \phi) = f(x, \phi) = A_{ij}\, x + B_{ij}\, \phi + C_{ij}\, x\, \phi + D_{ij} \tag{2.16}$$

with the notation $x = \cos\theta$. The interpolation coefficients (A_{ij}, B_{ij}, C_{ij}, and D_{ij}) are determined with function values of the four node points of each grid cell; see Wang *et al.* (2006, eq. 13) for the explicit integration coefficients. Those are included in eq. 2.15 to obtain the final equation for the analysis of the spherical harmonic coefficients:

$$\begin{aligned} f_{lm} = {} & (-1)^{m+1} \sqrt{\frac{2\,l+1}{4\,\pi}} \sum_{i=1}^{i_{\max}} \left[\int_{x_{i-1}}^{x_i} x \sqrt{\frac{(l-m)!}{(l+m)!}}\, P_{l,m}(x)\, dx \right] \sum_{j=1}^{j_{\max}} \left\{ \int_{\phi_{j-1}}^{\phi_j} (A_{ij} + C_{ij}\, \phi)\, e^{-im\phi}\, d\phi \right\} \\ & + (-1)^{m+1} \sqrt{\frac{2\,l+1}{4\,\pi}} \sum_{i=1}^{i_{\max}} \left[\int_{x_{i-1}}^{x_i} \sqrt{\frac{(l-m)!}{(l+m)!}}\, P_{l,m}(x)\, dx \right] \sum_{j=1}^{j_{\max}} \left\{ \int_{\phi_{j-1}}^{\phi_j} (D_{ij} + B_{ij}\, \phi)\, e^{-im\phi}\, d\phi \right\} \end{aligned} \tag{2.17}$$

The integration over the longitude in the curly braces is solved via the Fast Fourier Transform. The integration over the latitude in the square braces is solved by using recursion relations for the

Legendre Polynomials. Those recursion relations are stable up to degree and order 2200 for double precision calculations. A detailed description of the whole algorithm is given in Wang *et al.* (2006).

The estimated surface spherical harmonic coefficients are subsequently transformed into fully normalized surface spherical harmonics by the relation:

$$\begin{aligned} c_{l0} &= \frac{1}{\sqrt{4\,\pi}}\, f_{l0} && (m=0) \\ c_{lm} &= \frac{(-1)^m}{\sqrt{2\,\pi}}\, \mathrm{Re}(f_{lm}) && (m>0) \\ s_{lm} &= \frac{(-1)^{m+1}}{\sqrt{2\,\pi}}\, \mathrm{Im}(f_{lm}) && (m>0) \end{aligned} \tag{2.18}$$

In a last step, the potential coefficients are obtained out of the mass coefficients following Dong *et al.* (1996):

$$\left\{ \begin{matrix} C_{lm} \\ S_{lm} \end{matrix} \right\} = 4\,\pi\, \frac{a_{45}^2}{M_E} \left(\frac{1+k_l^{'}}{2\,l+1} \right) \left\{ \begin{matrix} c_{lm} \\ s_{lm}. \end{matrix} \right\} \tag{2.19}$$

In addition to the direct effect of surface masses, the elastic deformations of the solid Earth under the variable mass load are taken into account in eq. (2.19) via the Load Love numbers $k_l^{'}$. We use numerical estimates calculated by Pascal Gegout given in the Center of Mass of the Earth System (CM) frame for the PREM Earth model (Tab. 2.1). In order to properly represent degree-1 information from the atmospheric surface mass variability, we additionally calculate the k_1 Load Love number for the CF frame following Blewitt (2003):

$$\left[1+k_1^{'} \right]_{CF} = \left[-\frac{1}{3}\, h_1^{'} - \frac{2}{3}\, l_1^{'} \right]_{CM} \tag{2.20}$$

Table 2.1: Elastic Load Love Numbers $k_l^{'}$ for the PREM Earth model.

l	$k_l^{'}$
0	+0.000
1	+0.026
2	-0.305
3	-0.196
4	-0.134
5	-0.105
6	-0.090
7	-0.082
8	-0.077
9	-0.072
10	-0.069

2.6 Spatial Patterns of Trends and Variabilities

Stokes coefficients of the atmospheric surface pressure contribution to the time-variations of the Earth's gravity field have been analysed every 3 hours for the period 1976 until 2015. Subsequently, those coefficients are synthesized back onto an equi-angular grid for a series of consistency assessments as reported below. For simplicity, all anomalies in the potential are always expressed in terms of equivalent surface pressure (Wahr *et al.*, 1998):

$$\begin{aligned} p_{\mathrm{resynt}}(\theta,\phi) &= g_{\mathrm{WMO}}\Delta\sigma(\theta,\phi) \\ &= g_{\mathrm{WMO}}\frac{a_{45}\rho_{ave}}{3}\sum_{l=0}^{\infty}\sum_{m=0}^{l}\frac{2l+1}{1+k'_l}\tilde{P}_{lm}(\cos\theta)\left(\Delta C_{lm}\cos(m\phi)+\Delta S_{lm}(m\phi)\right) \end{aligned} \tag{2.21}$$

where a spherical geometry with the Earth's mean radius a_{45} and a constant gravity acceleration g_{WMO} have been applied.

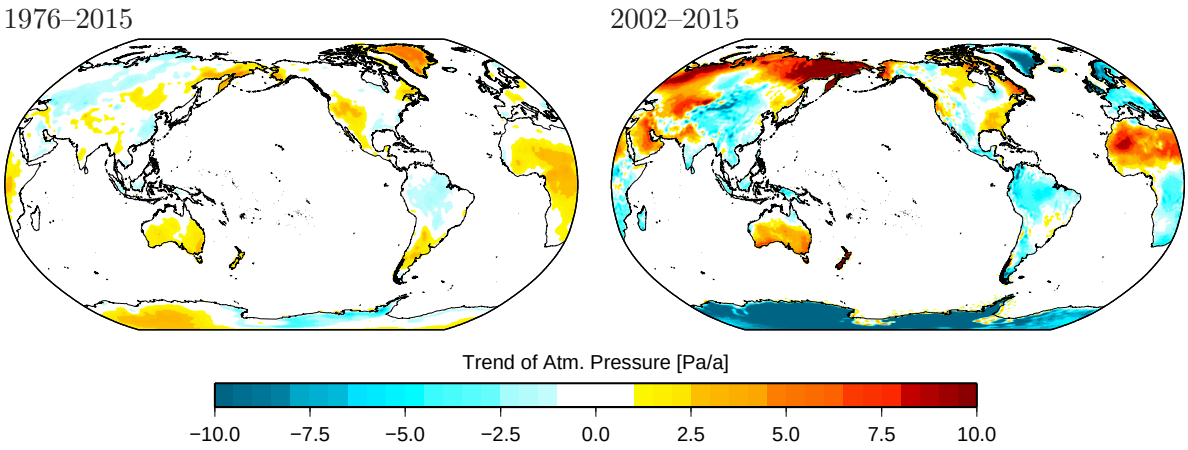

Figure 2.2: Trends in atmospheric surface pressure over the period 1976 – 2015 (left) and 2002 – 2015 (right) as included in AOD1B.

Atmospheric surface pressure variations utilized for AOD1B do not include strong trends (Fig. 2.2). During the 40-years long period between 1976 – 2015, local atmospheric pressure changes by less than 5 Pa a^{-1}, which corresponds to a change of only 5 mm water equivalent during one decade. Such tiny pressure drifts are well within the range of natural climate variability. Apparent trends estimated over the GRACE mission period 2002 – 2015 approach 10 Pa a^{-1} in several regions of the world, but are in fact not related to long-term drifts in pressure but to interannual-to-decadal climate variability.

The yearly mean signals of atmospheric surface pressure are in the range of about 5 hPa (Fig. 2.3). The spatial pattern are dominated by large-scale features as previously known from climate model simulations so that the change in spatial resolution from 78 km until 2006 to 18 km in 2015 has apparently no impact. Annual mean pressure anomalies of 3 to 5 hPa in Antarctica, however, underline once more the importance of high-quality long-term stability of AOD1B, since ice-mass change signals in that area are of similar or even smaller magnitude.

RMS variability of the 3 hourly atmospheric surface pressure anomalies calculated individually between 2004 and 2015 do not reveal systematic changes in variability during the years (Fig. 2.4). Surface pressure changes are strongest in moderate-to-high latitudes at both hemispheres. Variability pattern are clearly modified by orographic features as the Andes, Himalaya, Karakoram, or the Ural, but no apparent effects of the ECMWF model resolution changes are evident.

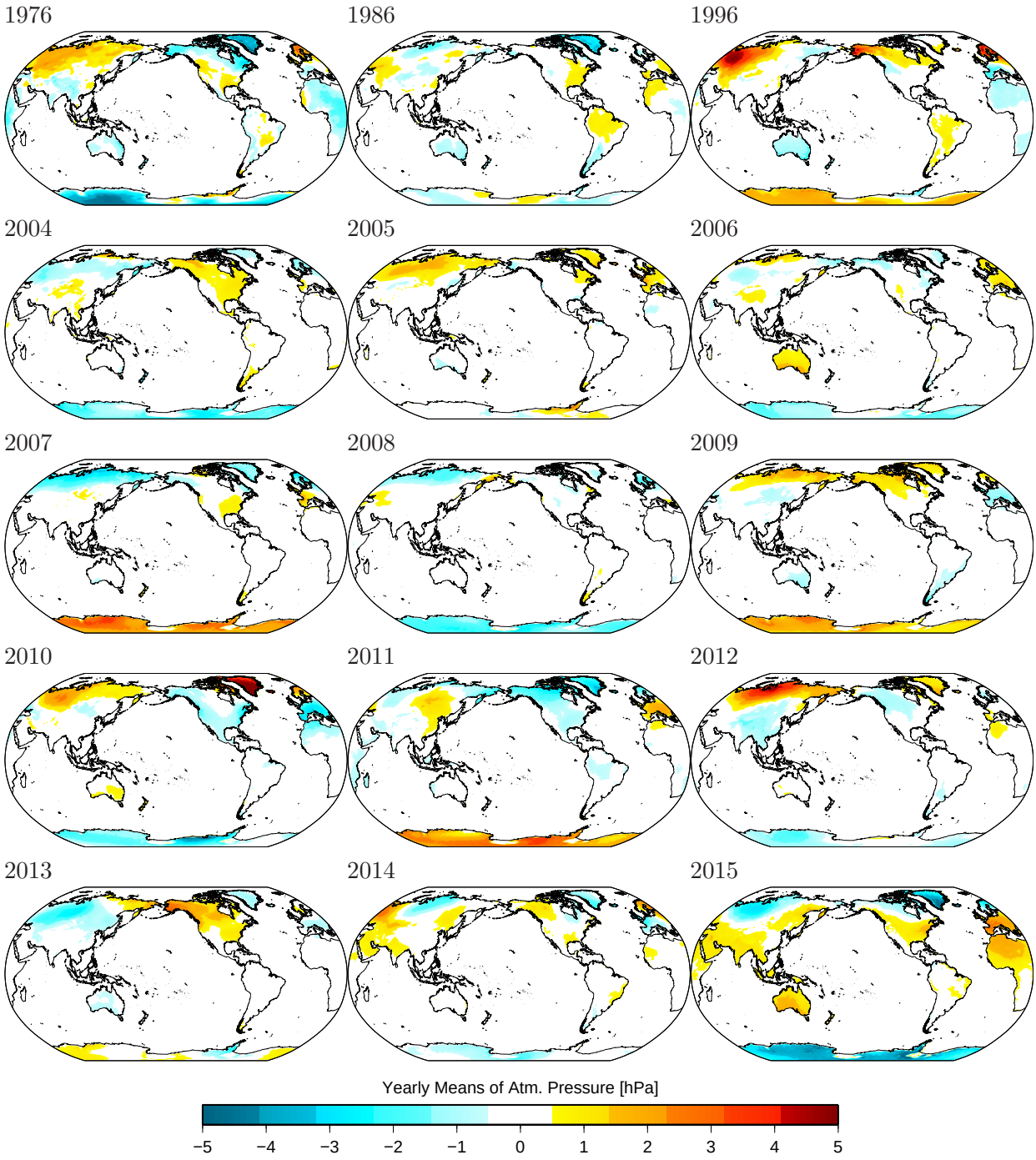

Figure 2.3: Yearly means of atmospheric surface pressure anomalies for the years 1976, 1986, 1996 and 2004 – 2015 as included in AOD1B.

2.7 Assessment of 3-Hourly Tendencies

We also calculate differences of consecutive 3-hourly time-steps of the re-synthesized anomalies in the gravity potential expressed in terms of equivalent surface pressure. Those tendencies will be particularly large at times where a jump in the series appears. However, neither the yearly RMS values of the surface pressure tendencies (Fig. 2.5) nor the time-series of area-averaged absolute values of pressure tendencies (Fig. 2.6) give evidence for such inconsistencies.

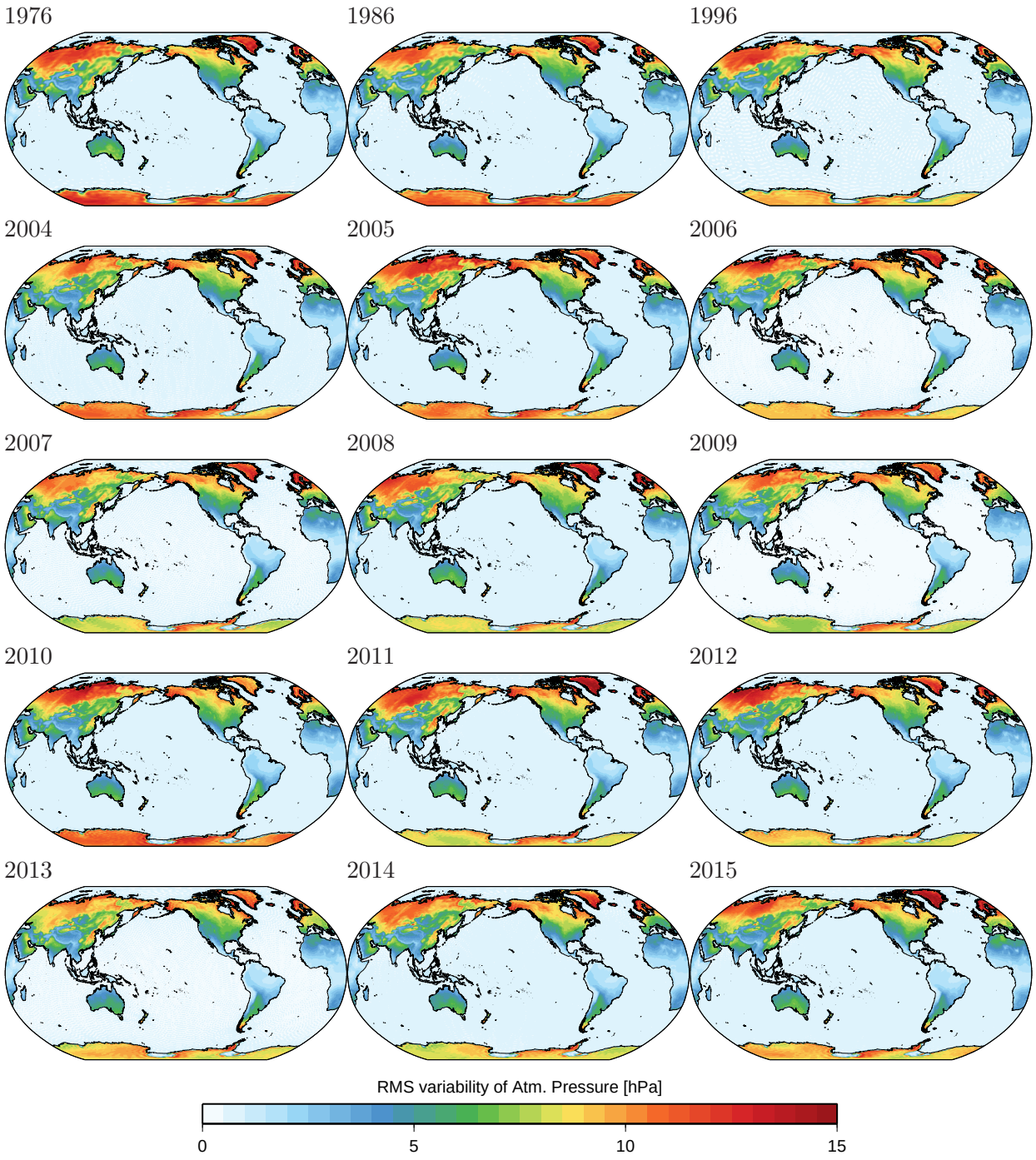

Figure 2.4: RMS variability of 3 hourly atmospheric surface pressure anomalies as included in AOD1B calculated individually for the years 1976, 1986, 1996 and 2004 – 2015.

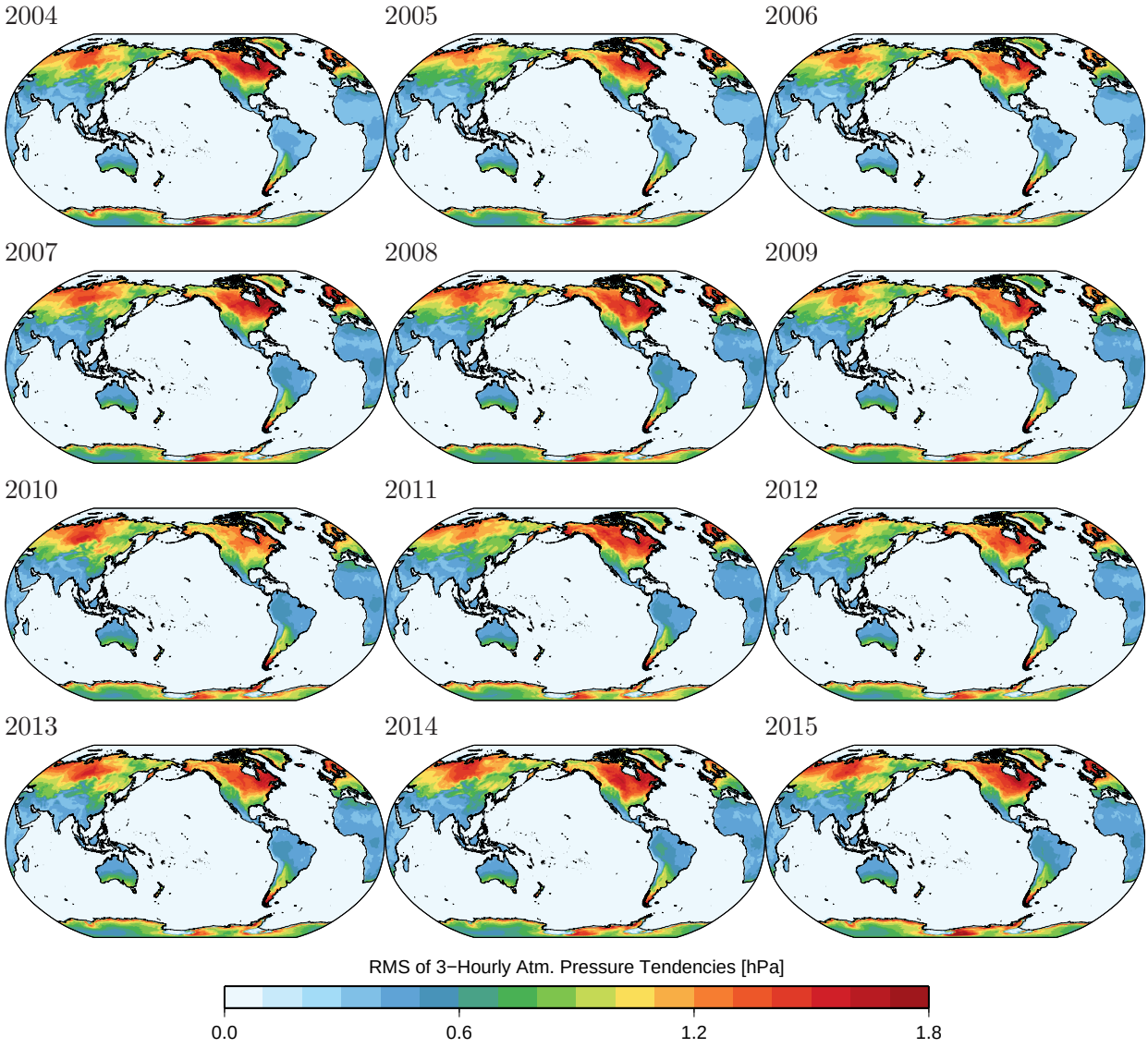

Figure 2.5: RMS variability of 3 hourly tendencies of atmospheric surface pressure as included in AOD1B.

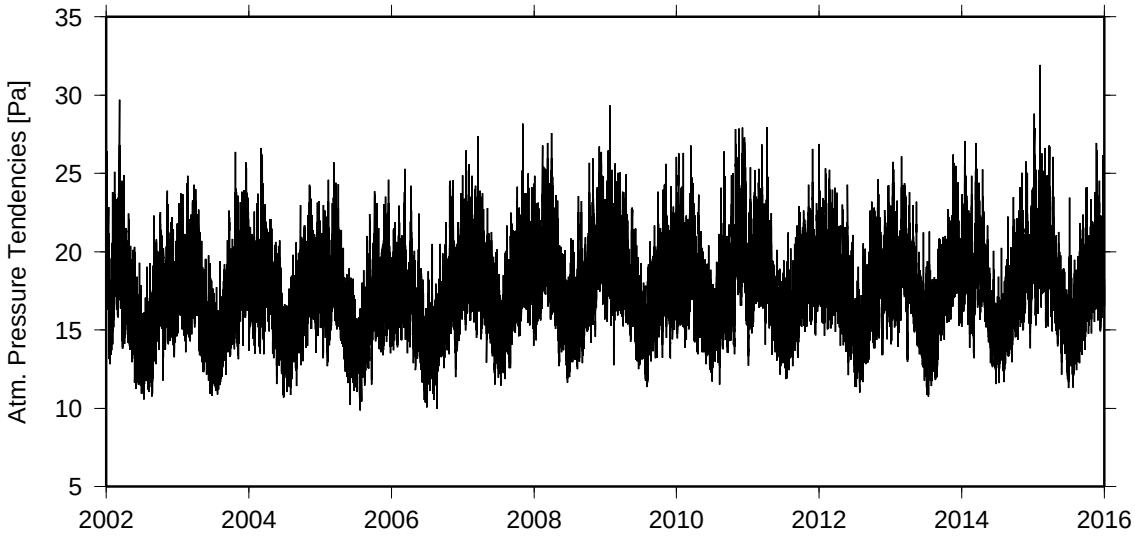

Figure 2.6: Area-weighted global mean of absolute values of 3 hourly tendencies of atmospheric surface pressure as included in AOD1B.

Chapter 3

Dynamic Ocean Contribution to Bottom Pressure Variability

3.1 OGCM Configuration

The ocean component of AOD1B is based on a numerical simulation with the Max-Planck-Institute for Meteorology Ocean Model (MPIOM; Jungclaus *et al.*, 2013). It is a general ocean circulation code discretized globally on an Arakawa C-grid in the horizontal, and a z-grid in the vertical. It includes a sea-ice module (Notz *et al.*, 2013) that utilizes the viscous-plastic rheology of Hibler (1979).

Decades-long numerical model development efforts by Ernst Maier-Reimer (1944 – 2013; Hasselmann, 2013) and his colleagues in Hamburg resulted in a series of high-quality software packages, as, e.g., the Large-Scale Geostrophic Ocean General Circulation Model (LSG; Maier-Reimer & Mikolajewicz, 1992), the Hamburg Ocean Primitive Equation Model HOPE (Drijfhout *et al.*, 1996; Wolff *et al.*, 1997), and the first release of MPIOM (Marsland *et al.*, 2003). The Ocean Model for Circulation and Tides (OMCT; Thomas *et al.*, 2001) used for previous releases of AOD1B is also a direct descendant of HOPE and thus shares many similarities in both physics and numerics with even the current version of MPIOM, which finally results in quite small differences in key ocean circulation features of the simulations used for AOD1B RL04 (Dobslaw & Thomas, 2007), RL05 (Dobslaw *et al.*, 2013), and the current version.

We employ code revision #3944 of MPIOM that was released in October 2015. A few changes have been performed to the code in order to make use of experience gained with OMCT during the most recent years in the context of simulating ocean bottom pressure variability, which in particular includes the activation of atmospheric surface pressure forcing, and some modifications to the vertical momentum transfer in response to surface winds. A medium-resolution configuration of MPIOM is used here that is discretized on a 1.0° tri-polar grid with 40 vertical layers (TP10L40). The internal time-step of the model is 90 min, and ocean state quantities and associated diagnostics as ocean bottom pressure and horizontal currents necessary to derive ocean angular momentum changes relevant for Earth rotation research (Dobslaw *et al.*, 2010) are stored every 3 hours. The model configuration currently employed for AOD1B RL06 does not simulate ocean dynamics underneath the Antarctic ice-shelves. Similarly, feedbacks on the ocean dynamics from self-attraction effects of the water column and associated deformations of the sea-floor (Ray, 1998; Kuhlmann *et al.*, 2011) are not considered yet.

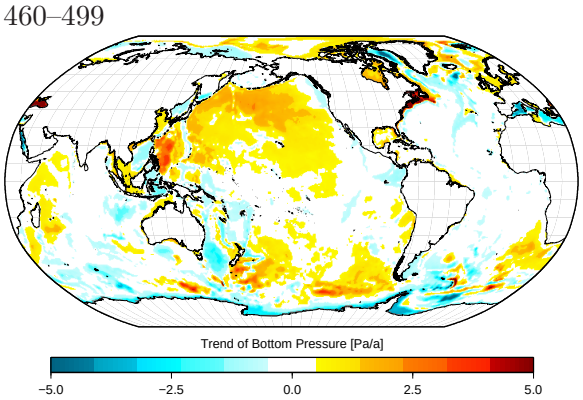

Figure 3.1: Trend in the dynamic ocean contribution to bottom pressure obtained from the years 460 - 499 of the MPIOM spin-up simulation.

3.2 Atmospheric Forcing Data

Dynamics simulated by MPIOM in our particular model experiment are driven by atmospheric forcing only, and no observational constraints are introduced into the simulation by means of data assimilation. As for previous releases of AOD1B, luni-solar gravitational tides in the oceans are not simulated, but tidal waves in response to periodically varying atmospheric pressure loading and surface winds are part of the simulated ocean bottom pressure field. Those signals are separated during the post-processing from the non-tidal AOD1B coefficients as discussed in Ch. 6.

The simulation is initialized from 3D temperature and salinity climatologies (Levitus, 2005) followed by a spin-up simulation under cyclic atmospheric forcing conditions with daily sampling as prepared for an ocean model intercomparison project (Röske, 2005). The spin-up simulation has been integrated over 499 years, remaining trends in ocean bottom pressure are less than ±3 Pa a^{-1} on regional scales, and ±12 Pa a^{-1} even for individual grid points (Fig. 3.1). The spin-up is followed by a transient simulation with 3 hourly atmospheric forcing obtained from ERA-40 for the period 1970 - 1978, from ERA-Interim during 1979 – 2006, and from the operational ECMWF data for all subsequent years.

MPIOM requires the following atmospheric forcing data-sets: atmospheric surface pressure; horizontal surface wind stress, surface wind speed, temperature as well as dew point temperature at 2 m above the surface; cloud cover, short-wave incoming radiation at the surface, and precipitation. Wind stress is derived from horizontal winds at 10 m above ground, density of air at the lowest model level as defined by temperature and specific humidity, and the Charnock parameter that characterizes the roughness of the sea-surface (Beljaars, 1997). The instantaneous horizontal wind stress components are calculated by employing FORTRAN routines provided by ECMWF that are consistent with the IFS cycle 23r1 (Anton Beljaars, pers. communication, 2004).

3.3 Post-Processing of Simulated Bottom Pressure

Ocean bottom pressure is a standard output variable of MPIOM that hydrostatically sums the contributions of air and water masses along the plumb line. For the separation of the oceanic contribution to bottom pressure, the atmospheric surface pressure applied as a forcing data-set is subtracted. In order to remove artificial fluctuations in total ocean mass induced by the Boussinesq approximation employed in the MPIOM momentum equations, the mean bottom pressure averaged

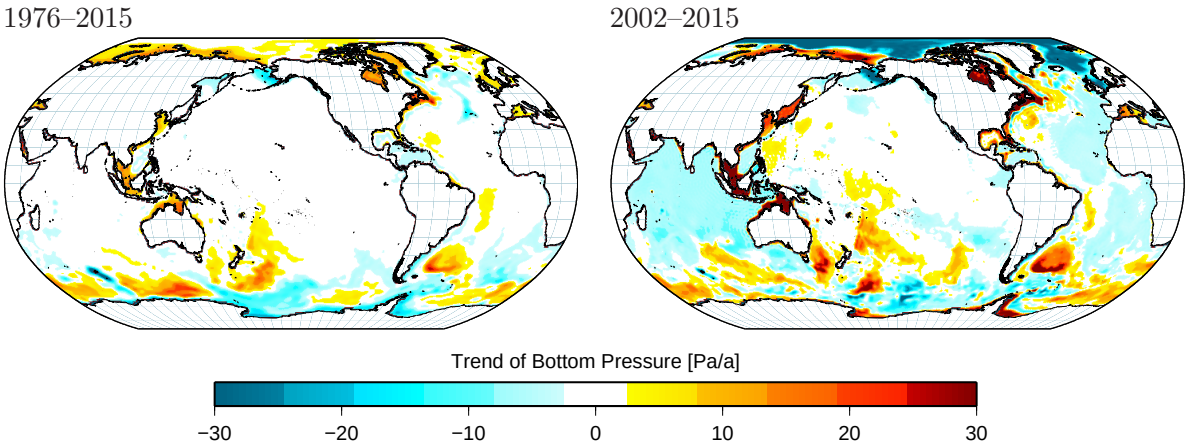

Figure 3.2: Trend in the dynamic bottom pressure over the period 1976 – 2015 (left) and 2002 – 2015 (right) as included in AOD1B.

over the whole ocean domain is removed by subtracting a homogeneous shell of mass at every time-step (Greatbatch, 1994):

$$p_b'(\theta,\phi) = p_b(\theta,\phi) - \frac{1}{A_{\text{Oceans}}} \iint\limits_{\text{Oceans}} p_b(\theta,\phi) dA \tag{3.1}$$

Subsequently, tidal fluctuations as discussed in Ch. 6 are estimated and removed, and the long-term mean ocean bottom pressure averaged over the period 2003 – 2014 is subtracted to arrive at pressure anomalies. Further, pressure anomalies are additive-inversely IB-corrected by re-adding the difference between the local atmospheric surface pressure and the mean surface pressure averaged over the whole ocean domain.

In the following, we will exclusively discuss bottom pressure anomalies that exclude the static contribution of the mean atmospheric surface pressure in all oceanic regions, which is called "dynamic contribution to bottom pressure" or "dynamic bottom pressure" in the remainder of this document. Pressure anomalies are transformed into Stokes coefficients up to d/o = 180 as described in Sect. 2.5 by assuming that all mass variability takes place at the surface of the reference ellipsoid, which implies that both ξ and h are assumed to be zero over the oceans.

3.4 Spatial Patterns of Trends and Variabilities

Stokes coefficients of the dynamic ocean contribution to the time variations of the Earth's gravity field are resynthesized back onto an equi-angular grid for a series of consistency checks as reported below. Long-term trends obtained from the years 1976 – 2015 are in the range of 10 Pa a^{-1} regionally. They mostly take place in the surroundings of the ACC and therefore reflect adjustment of the ocean dynamics to the ECMWF-based wind forcing. Trend pattern are, however, largely different when compared to the trends obtained from the spin-up run, thereby indicating that the remaining trends are not related to ongoing deep-sea adjustment processes or artificial drift in the model. In addition, trends are only slightly larger than corresponding atmospheric trends, which is an acceptable level of accuracy in view of the currently available length of the satellite gravimetry data record.

Yearly means of ocean bottom pressure reveal signals of a few hPa in particular in the Southern Ocean (Fig. 3.3) that are primarily related to large-scale changes in surface winds and thus time-

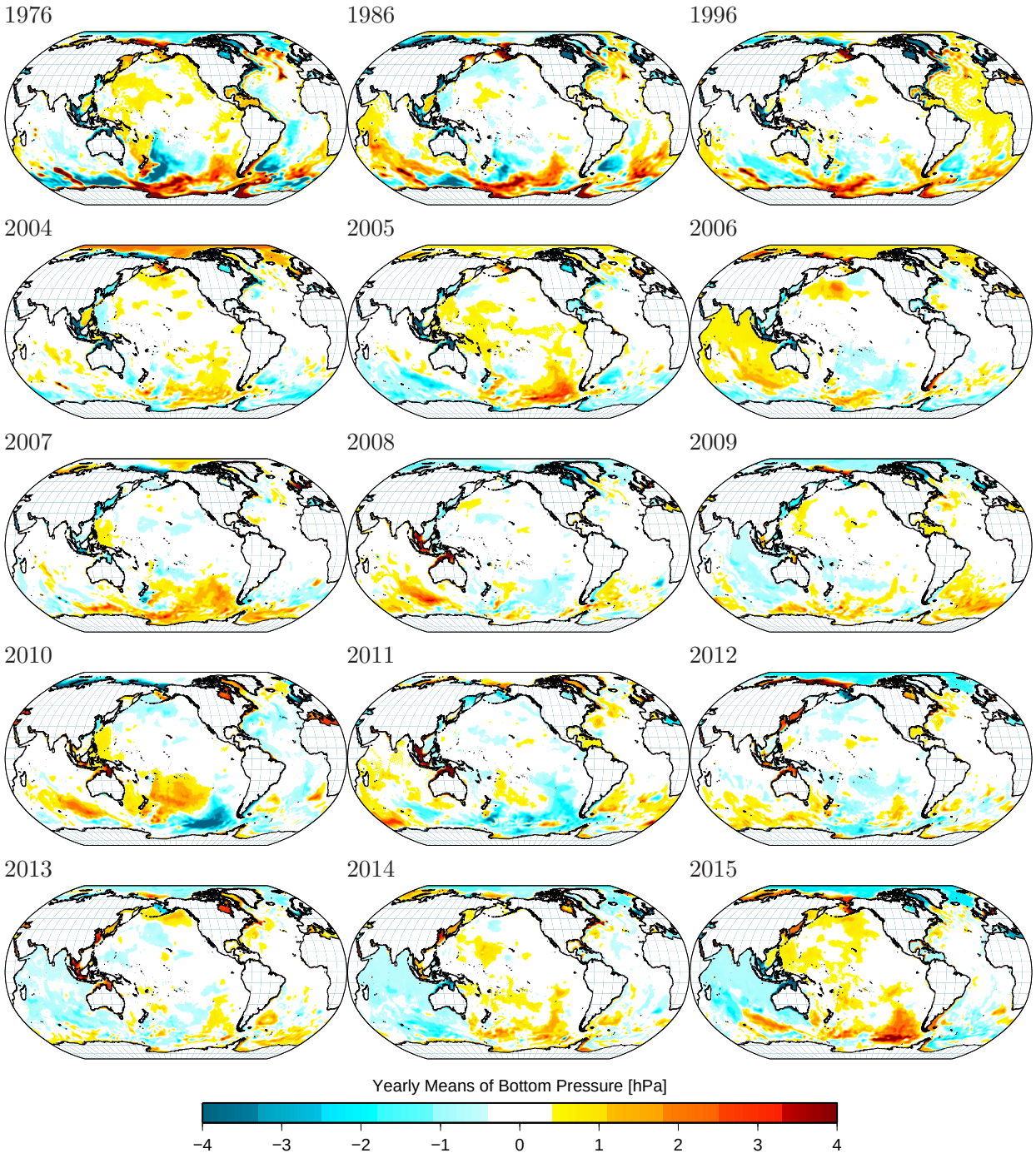

Figure 3.3: Yearly means of dynamic ocean bottom pressure for the years 1976, 1986, 1996 and 2004 – 2015 as included in AOD1B.

varying transports in the Antarctic Circumpolar Current (Bergmann & Dobslaw, 2012). Signals of comparable magnitude are also present in the Arctic Ocean, whereas low frequency variability in all other oceanic regions apart from the semi-enclosed seas are much smaller.

Variability in simulated dynamic ocean bottom pressure is fairly consistent throughout the years despite of the fact that atmospheric forcing from ERA-40, ERA-Interim, and the operational ECMWF model is considered (Fig. 3.4). Strongest variability takes place close to the coasts and within semi-enclosed seas as the North Sea or within the Indonesian Archipelago, whereas open-ocean signals

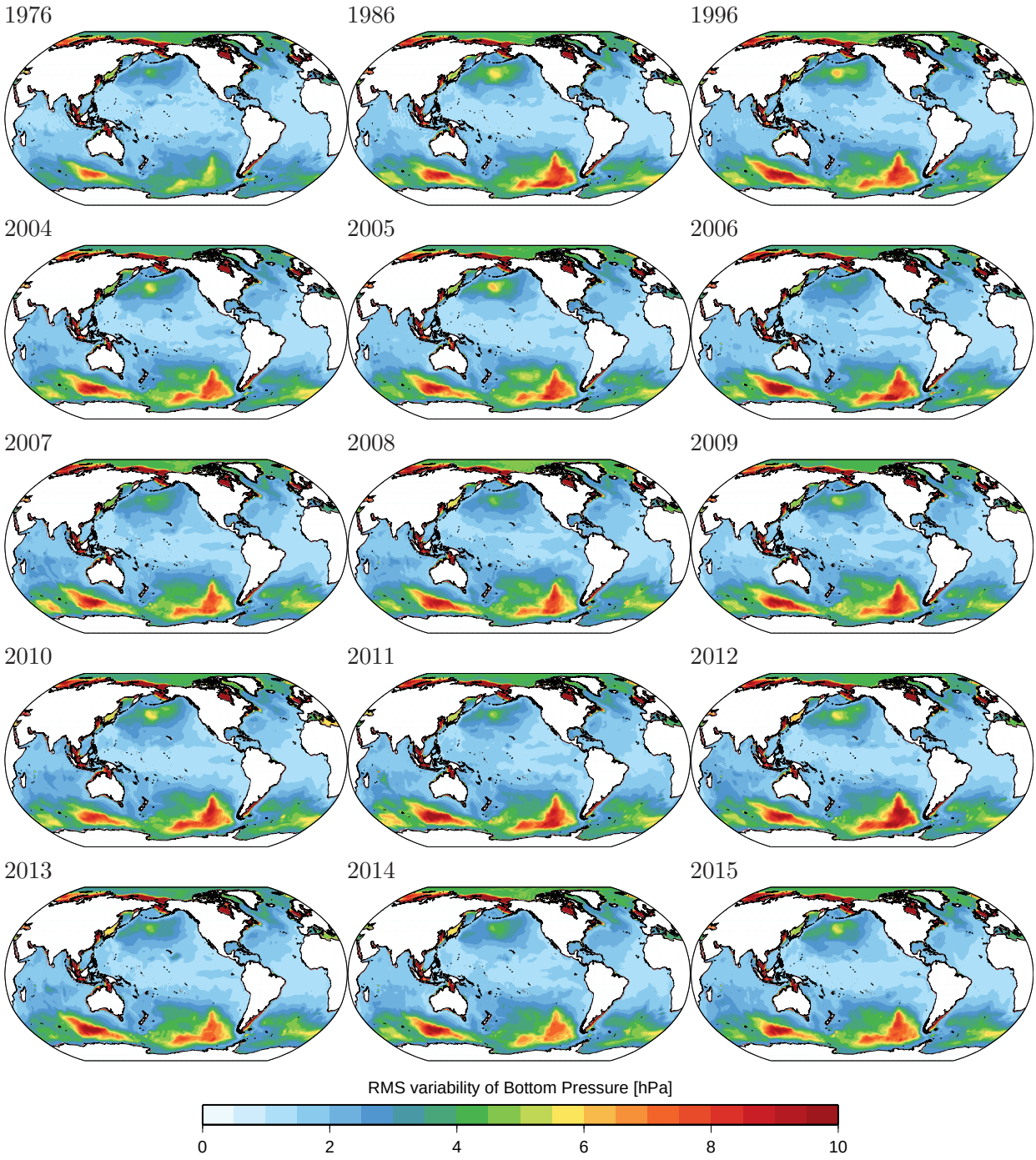

Figure 3.4: RMS variability of 3 hourly dynamic ocean bottom pressure anomalies as included in AOD1B calculated individually for the years 1976, 1986, 1996 and 2004 – 2015.

are strongest in the surroundings of the Antarctic Circumpolar Current.

3.5 Assessment of 3-Hourly Tendencies

We also calculate differences of consecutive 3-hourly time-steps of the re-synthesized anomalies in the gravity potential expressed in terms of equivalent bottom pressure. Those tendencies will be particularly large at times where a jump in the series appears. However, neither the yearly RMS

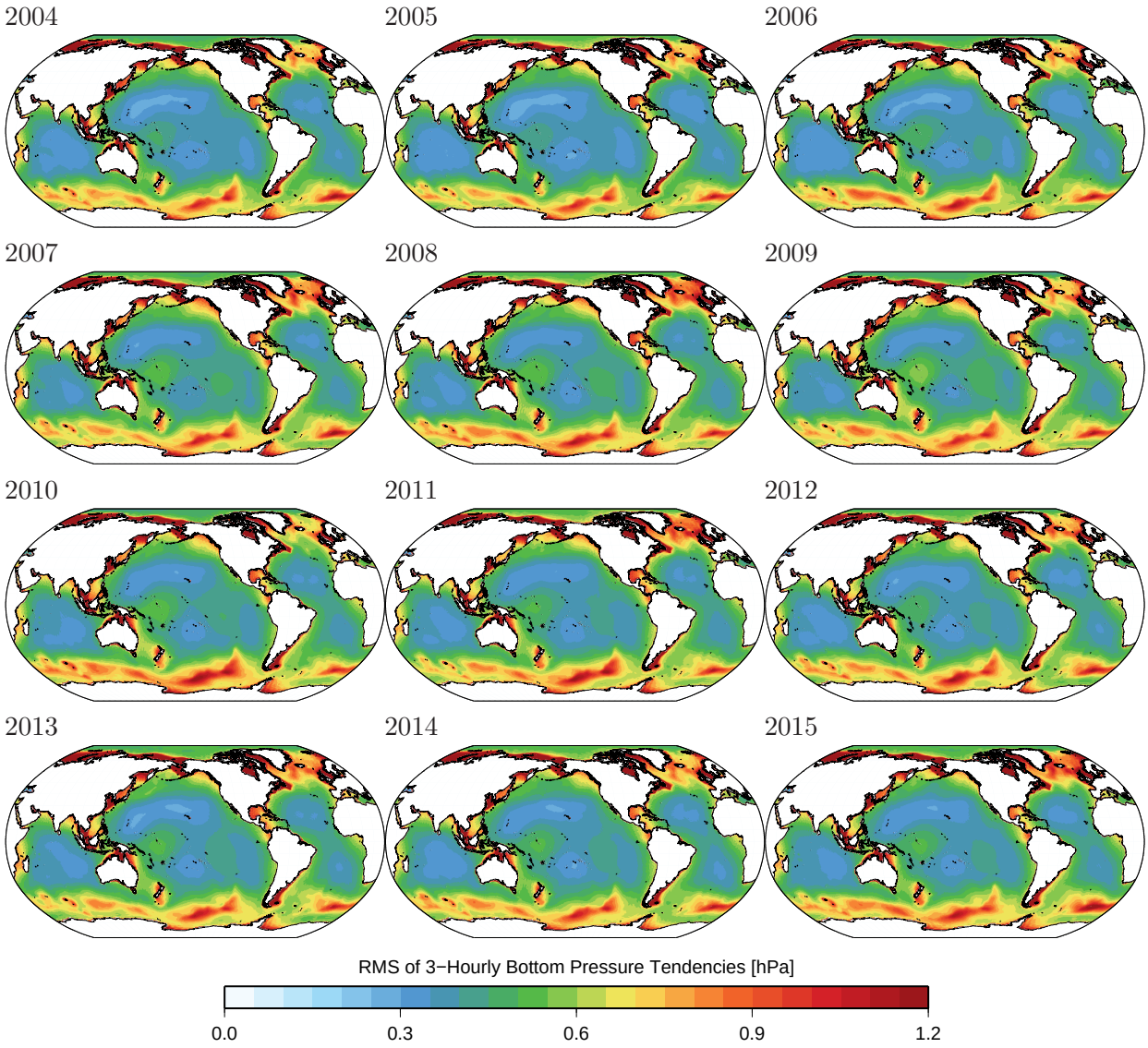

Figure 3.5: RMS variability of 3 hourly tendencies of dynamic ocean bottom pressure as included in AOD1B.

values of the bottom pressure tendencies (Fig. 3.5) nor the time-series of area-averaged absolute values of pressure tendencies (Fig. 3.6) give evidence for such inconsistencies. We note, however, a small increase of the average global tendencies at the beginning of the year 2007 which is related to the higher spatial resolution of the operational ECMWF data and the corresponding stronger spatial gradients in the surface wind fields, but conclude that this feature does not significantly affect the consistency of AOD1B in view of its intended applications in satellite gravimetry.

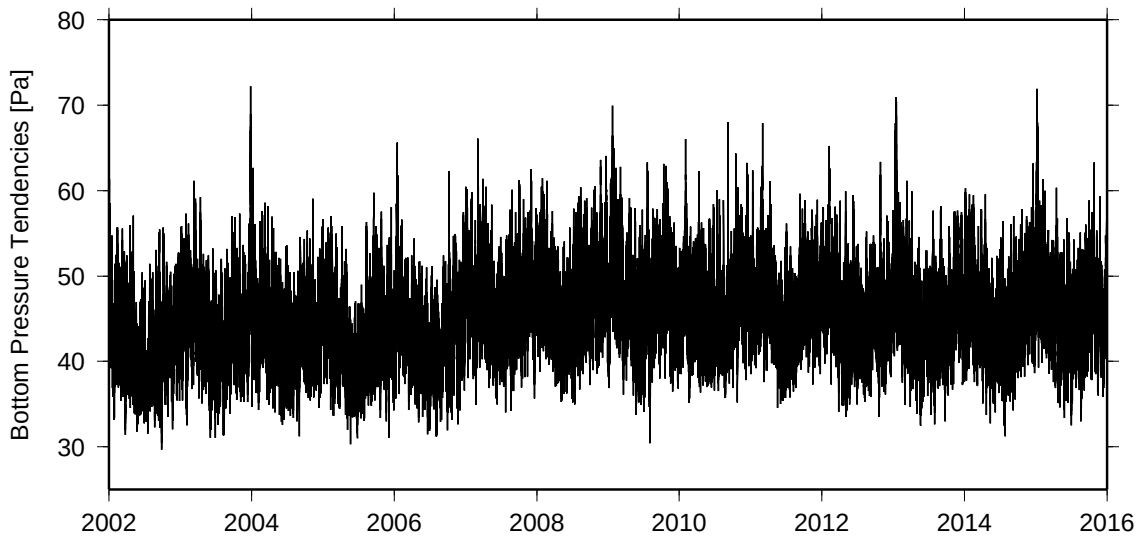

Figure 3.6: Area-weighted global mean of absolute values of 3 hourly tendencies of dynamic ocean bottom pressure as included in AOD1B.

Chapter 4

Attraction Effects of Upper-Air Density Anomalies

4.1 Atmospheric Density Data at Sigma Model Levels

Current state-of-the-art numerical weather prediction (NWP) models are discretized in the vertical at hybrid sigma levels, that smoothly follow the orography and are thus able to represent troposphere dynamics over rugged terrain more realistically. At higher altitudes, however, hybrid levels tend to align to the isobaric surfaces. The number of levels employed at ECMWF varies between k=60 (ERA-40 and ERA-Interim) and k=137 (IFS cycle 38r2). The topmost level with a pressure of typically 10 Pa is indicated by k=1, whereas $k = k_{\max}+1/2$ corresponds to the surface orography as the lower boundary of the atmosphere. Atmospheric pressure at the interface (i.e. half level) between two levels is obtained from surface pressure p_s and the coefficients $a_{k+1/2}$ and $b_{k+1/2}$ that define the vertical grid:

$$p_{k+1/2} = a_{k+1/2} + b_{k+1/2}\, p_s \tag{4.1}$$

Atmospheric density at full levels is conveniently represented by the virtual temperature T_v that can be derived from in situ temperature T and specific humidity q by incorporating the gas constants for both dry air R_d and water vapor R_v:

$$T_v = T\left(1 + \frac{1 - \dfrac{R_d}{R_v}}{\dfrac{R_d}{R_v}}\, q\right) \tag{4.2}$$

$$\approx T(1 + 0.608\, q) \tag{4.3}$$

The virtual temperatures are subsequently integrated vertically upwards to obtain the geopotential Φ at the level interfaces by starting from the surface geopotential at $k = k_{\max+1/2}$ with

$$\Phi_{k-1/2} = \Phi_{k+1/2} + \frac{R_d}{g_{\mathrm{WMO}}} T_{vk} \ln\left(\frac{p_{k+1/2}}{p_{k-1/2}}\right) \tag{4.4}$$

The geopotential heights $H_k = \Phi_k / g_{\mathrm{WMO}}$ at full model level k that represent the height of the pressure element $\Delta p_k = p_{k+1/2} - p_{k-1/2}$ are finally transformed into orthometric heights by utilizing eq. 2.10.

Finally, the full atmospheric mass distribution discretized at the model levels k forms the inner integral of eq. 2.7 as follows:

$$\Delta I_l = \int_0^{\infty} \left(\frac{r}{a_{45}}\right)^{l+2} \rho(r) dr \tag{4.5}$$

$$= \sum_{k=1}^{k_{\max}} \left(\frac{a + z_k}{a_{45}}\right)^{l+2} \frac{\Delta p_k}{g} \tag{4.6}$$

4.2 Separation of Upper-Air Density Attraction Effects

The inner integral of the 3D atmospheric masses as given in eq. 4.6 does include the summarized effect of both surface pressure and the contributions of density anomalies above ground. For AOD1B, we subtract the effect of surface pressure which has been already treated in Ch. 2:

$$\Delta I_l = \left[\sum_{k=1}^{k_{\max}} \left(\frac{a + z_k}{a_{45}}\right)^{l+2} \frac{\Delta p_k}{g}\right] - \left(\frac{a + z_{\mathrm{mdp}}}{a_{45}}\right)^{l+2} \frac{p_s}{g} \tag{4.7}$$

where the orthometric height of the mass mid-point of the air column z_{mdp} is approximated from the surface geopotential of a reference atmospheric density profile. The inner integral of residual atmospheric masses that cause an additional attraction effect on the Earth's gravity field are subsequently analyzed into spherical harmonics with eq. 2.13. Note that k'_l is set to zero in this case, since upper-air mass anomalies do not cause a deformation of the Earth's surface.

4.3 Impact of ECMWF Model Changes

In order to evaluate the potential impact of ECMWF model changes and the rather *ad hoc* approximation of the mass mid-point of the air columns employed in eq. 4.7, the atmospheric attraction effects are calculated from both ERA-Interim and the operational ECMWF data for the years 2000 – 2015 and 2007 - 2015, respectively, and the long-term mean over the period 2003 – 2014 obtained from ERA-Interim is subtracted at coefficient level. By analyzing the differences between ERA-Interim and operational ECMWW-based coefficients, we identify two major offsets introduced for the first time on January 1st, 2007 and June 25th, 2013, that have been quantified and subsequently removed by minimizing the residuals between both ECMWF data-sets over the corresponding periods 2007 – 2013 and 2013 – 2015, respectively (Fig. 4.1).

4.4 Spatial Patterns of Trends and Variabilities

Stokes coefficients of the attraction effect of upper-air density anomalies to the time-variations of the Earth's gravity field are synthesized back onto an equi-angular grid for a series of consistency assessments as reported below. Re-synthesis has been again performed with eq. 2.21 to allow for an easy cross-comparison with the effects of atmospheric surface pressure and ocean bottom pressure.

Secular trends in the effects of upper-air density anomalies on the Earth's gravity field over the period 2000 – 2015 (Fig. 4.2) in terms of equivalent surface pressure changes only amount to about 1 Pa a^{-1}, which is perceived to fit well into the range of natural climate variability and therefore does not introduce artificial drift into AOD1B.

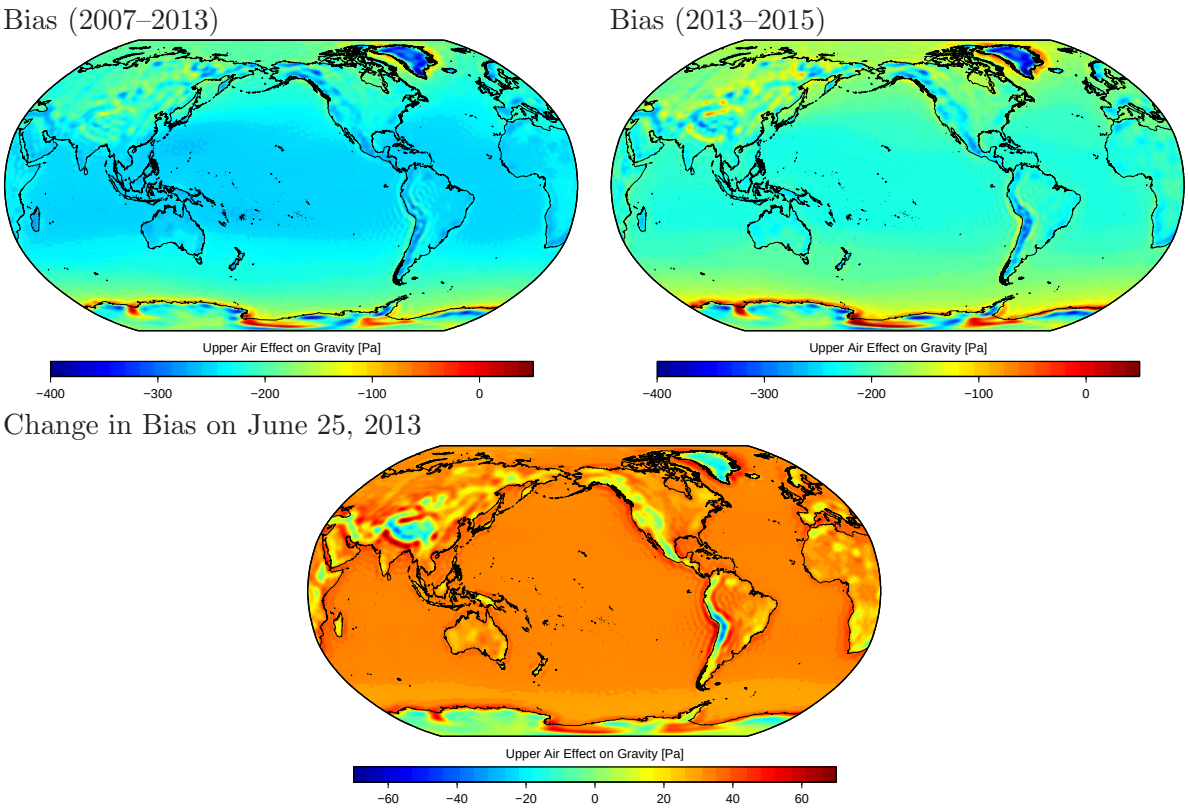

Figure 4.1: Biases removed from the atmospheric attraction effects in AOD1B due to the introduction of the operational ECMWF data on January 1st, 2007 (top left), and the increase in vertical levels in the operational ECMWF data from 91 to 137 on June 25th, 2013 (top right). In addition, the change in bias on June 25th, 2013 is shown (bottom).

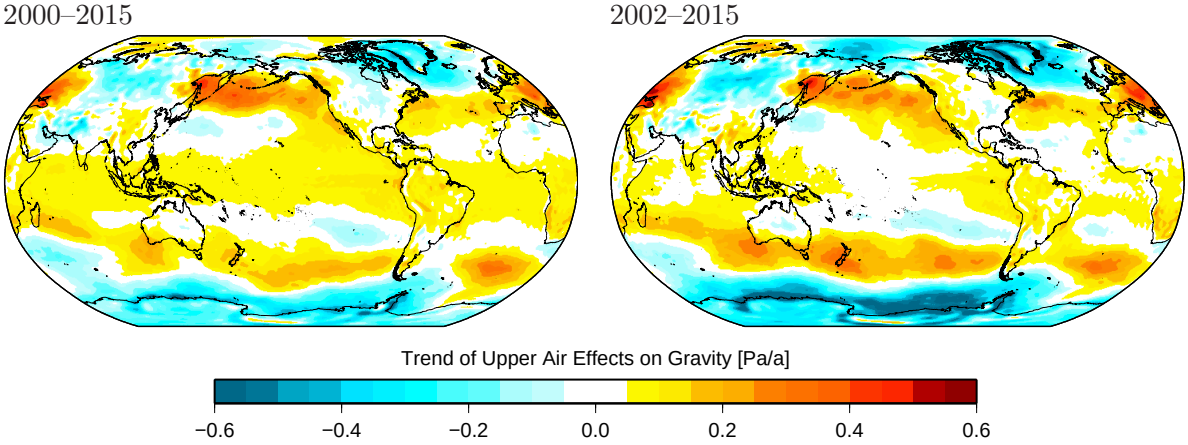

Figure 4.2: Trend in the effect of upper-air density anomalies on the Earth's gravity field as included in AOD1B over the period 2000 – 2015 (left) and 2002 - 2015 (right) as expressed in equivalent surface pressure changes at the reference orography.

Annual mean signals (Fig. 4.3) are in the range of 10 Pa and thus by a factor of 50 smaller than the contributions of atmospheric surface pressure. From an cross-comparison of the different years, no obvious jumps are discernible, indicating the removal of the empirically estimated biases as given in Fig. 4.1 was appropriate.

Similarly, the yearly RMS variability (Fig. 4.4) is homogeneous over the years considered. Signal

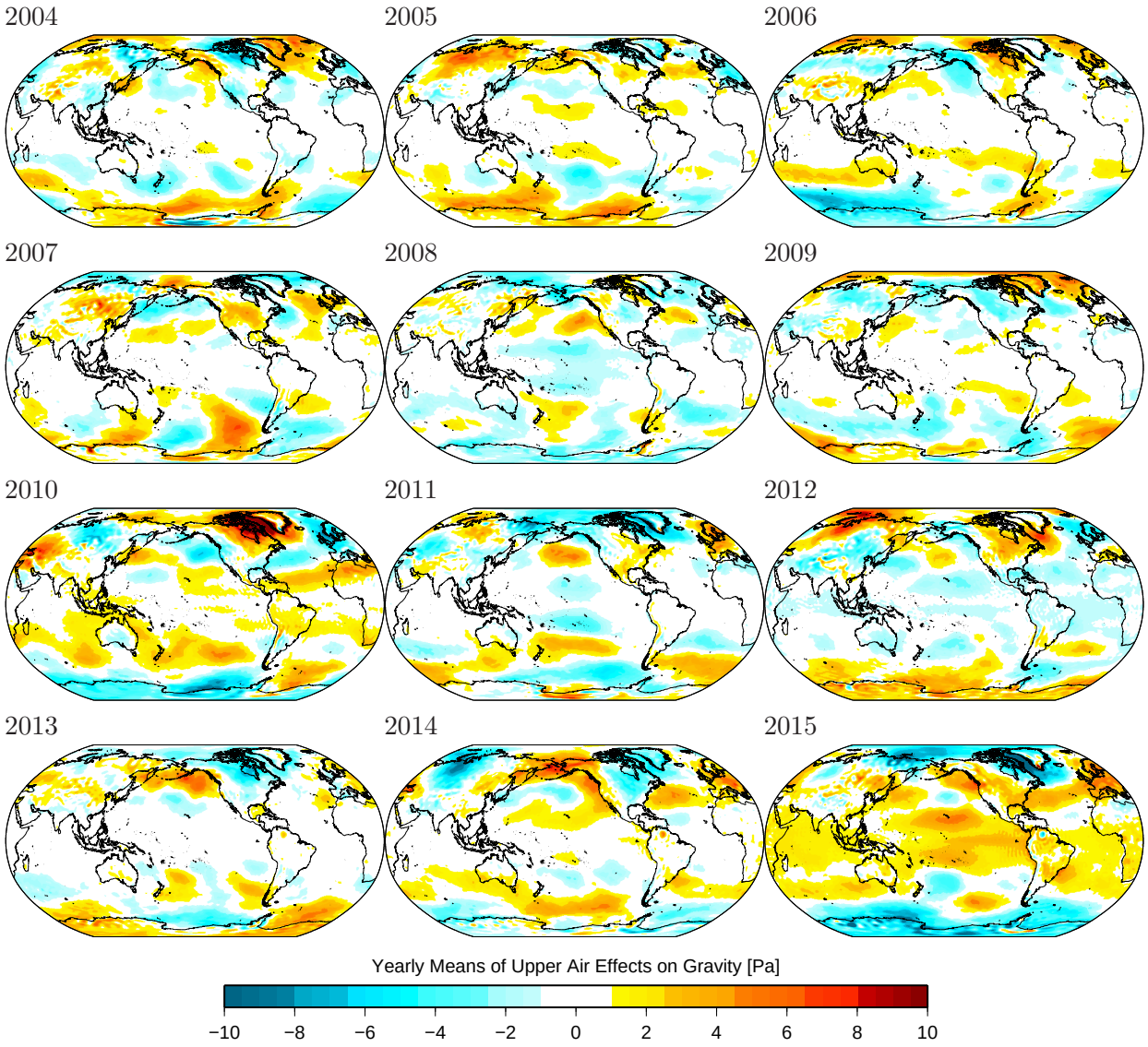

Figure 4.3: Yearly means in the effect of upper-air density anomalies on the Earth's gravity field as included in AOD1B for the period 2004 – 2015 as expressed in equivalent surface pressure changes.

variability is concentrated in the regions where the sub-polar jets show large intra-seasonal variability and thus cause anomalies in the upper-air density fields. However, variability is again much smaller than the corresponding effect of the atmospheric surface pressure discussed in Ch. 2.

4.5 Assessment of 3-Hourly Tendencies

We also calculate differences of consecutive 3-hourly time-steps of the re-synthesized anomalies in the gravity potential caused by upper-air density anomalies expressed in terms of equivalent surface pressure. Those tendencies will be particularly large at times where a jump in the series appears. However, neither the yearly RMS values of the tendencies (Fig. 4.5) nor the time-series of area-averaged absolute values of the tendencies (Fig. 4.6) give evidence for such inconsistencies. We note, however, an increase of the average global tendencies at the beginning of the year 2007 which is related to the higher spatial resolution of the operational ECMWF data. In view of the dominance of the atmospheric surface pressure contribution to changes in the Earth's gravity field,

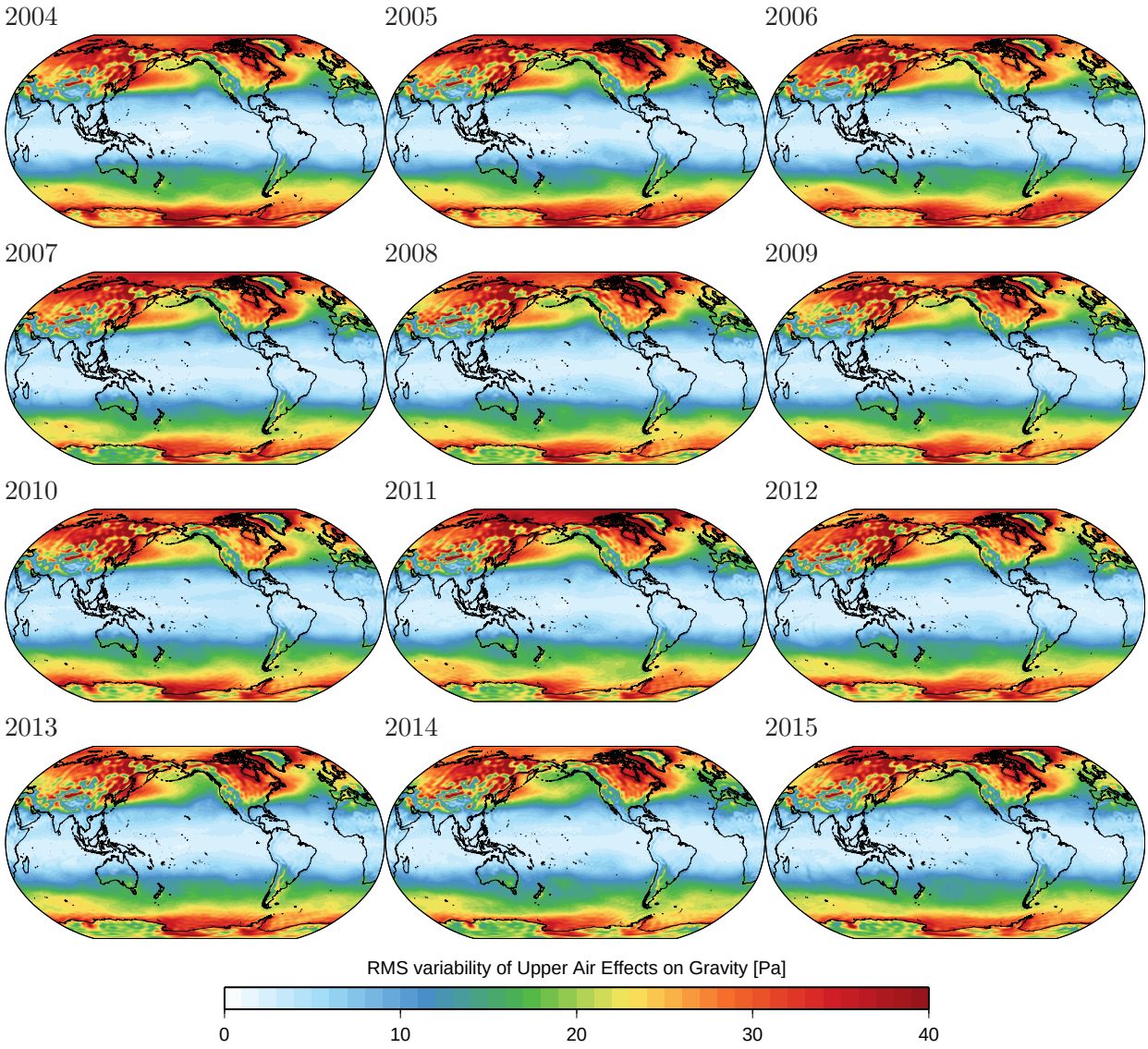

Figure 4.4: RMS variability of 3 hourly effect of upper-air density anomalies on the Earth's gravity field as included in AOD1B calculated individually for the years 2004 – 2015 as expressed in equivalent surface pressure changes.

however, we conclude that this feature does not significantly affect the consistency of AOD1B in view of its intended applications in satellite gravimetry.

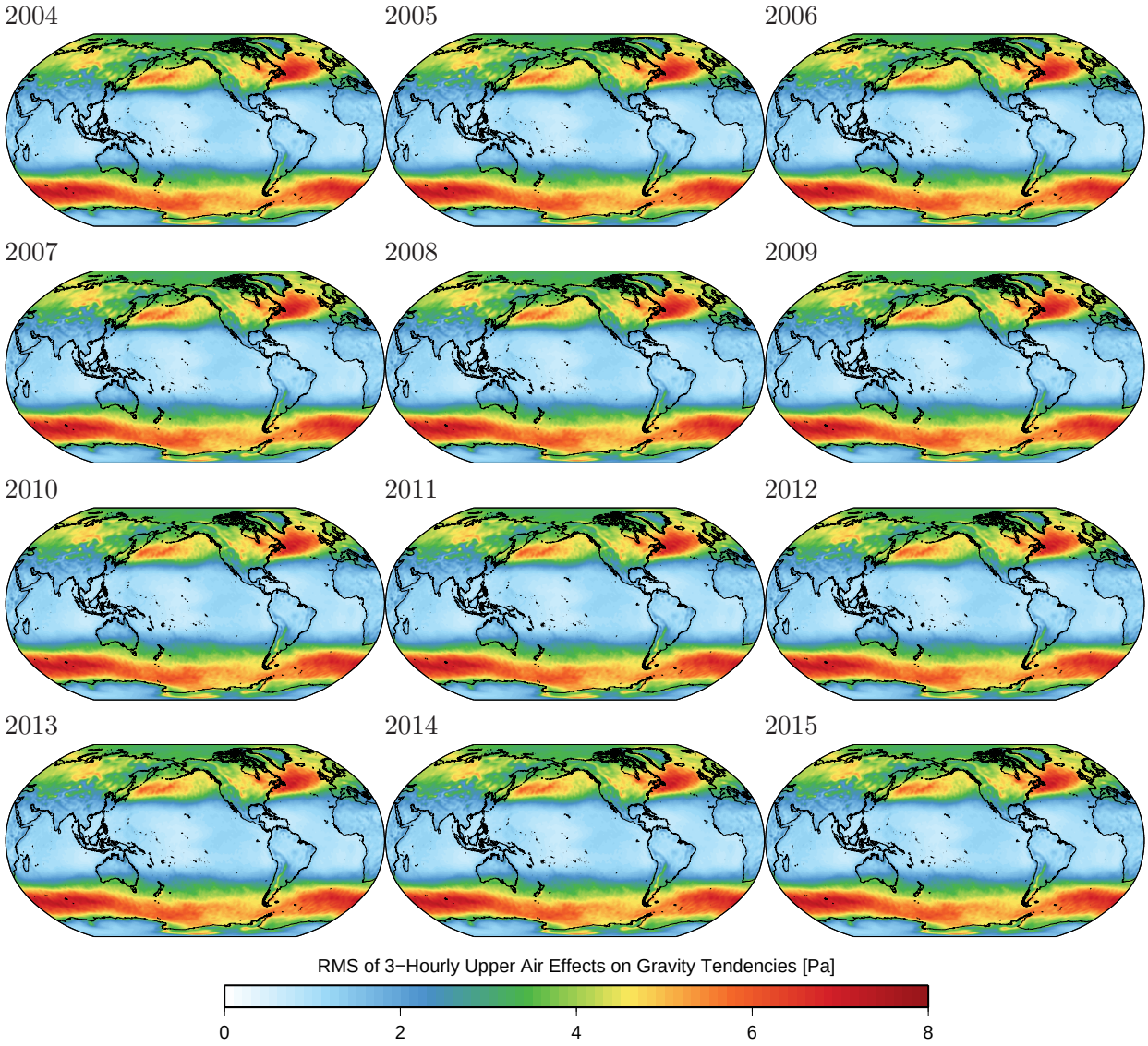

Figure 4.5: RMS variability of 3 hourly tendencies of upper air density anomalies as included in AOD1B.

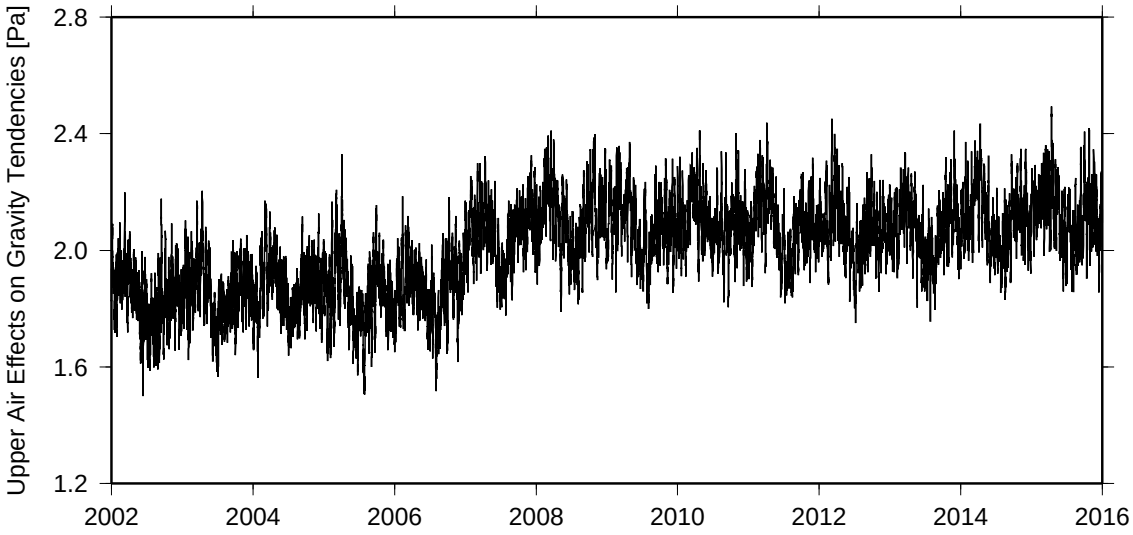

Figure 4.6: Area-weighted global mean of absolute values of 3 hourly tendencies of upper air density anomalies as included in AOD1B.

Chapter 5

Atmospheric Tides

5.1 Atmospheric Tides in ECMWF Surface Pressure

Atmospheric tides are to be understood here as periodic variations of atmospheric pressure relative to the moving surface of the Earth, which is the Earth's crustal surface in continental regions, and the ocean surface elsewhere. These tides are conventionally observed by pressure gauges attached to the ground, or tied to floating objects as buoys or ships.

Tides in the atmosphere are excited by two different mechanisms that are principally known already for decades: First, absorption of solar radiation by both water vapor and ozone creates large periodic temperature variations in the middle atmosphere that propagate vertically as approximately described by the thermal wind equations and cause large-scale variations in atmospheric surface pressure. The frequencies of this process are fundamentally governed by the incidence angle of solar radiation, so that periods of 24 hours and overtones may occur. Signals are not strictly periodic but vary in amplitude due to variations in solar insolation; changes in the atmospheric density of the lower troposphere affecting vertical wave propagation; and transient convective processes near the surface that cause periodic pressure variations at periods of 24 hours as well.

Secondly, tidal waves in the atmosphere are excited by direct gravitational attraction of atmospheric masses by the tide-generating bodies sun and moon, and – more importantly – also by periodic motions of the lower boundary of the atmosphere caused by both tides in the solid Earth and in the oceans. For this process, also secondary gravitational effects due to the modified mass distribution caused by ocean and solid Earth tides add small modifications to the signals.

The representation of surface atmospheric tides in global atmospheric model data has been validated in many aspects with the help of thoroughly screened sets of globally distributed in situ pressure gauges. Those analyses indicate that the principal frequencies S_1 and S_2 are quite well represented by ECMWF, even though a "small but probably significant overestimation of up to 18% for peak semidiurnal amplitudes" is reported (Schindelegger & Ray, 2014).

Signals of the semidiurnal lunar atmospheric tide, which corresponds in frequency to the oceanic tide M_2 have been detected in the 6 hourly atmospheric re-analysis ERA-Interim by Kohyama & Wallace (2014). Comparison against in situ pressure gauges reveals again a quite good level of agreement (Schindelegger & Dobslaw, 2016). The latter study gives also evidence that the ECMWF assimilation system favorably passes tidal variations measured by in situ pressure and wind data into the global analysis despite of the fact that the physics of in particular the lunar tides are not represented in the ECMWF model. Thus, the appearance of tides in ECMWF is somewhat affected by the evolution of the global observing system, as, for example, demonstrated by the disappearance of the M_2 tide after opening of the Panama Canal that redirected commercial shipping

Table 5.1: Tidal constituents estimated and removed from the non-tidal AOD1B coefficients.

partial tide	Argument	Frequency ($^\circ h^{-1}$)
P_1	$t - h - 90^\circ$	14.9589314
S_1	$t + 180^\circ$	15.0000000
K_1	$t + h + 90^\circ$	15.0410686
N_2	$2t - 3s + 2h + p$	28.4397295
M_2	$2t - 2s + 2h$	28.9841042
L_2	$2t - s + 2h - p + 180^\circ$	29.5284789
T_2	$2t - h + p'$	29.9589333
S_2	$2t$	30.0000000
R_2	$2t + h - p' + 180^\circ$	30.0410667
T_3	$3t - h$	44.9589300
S_3	$3t$	45.0000000
R_3	$3t + h$	45.0410700

routes and thus drastically reduced the number of observations in other parts of the world (see Schindelegger & Dobslaw, 2016, Sect. 5).

Despite of the overall good agreement between ECMWF and in situ pressure gauges, some discrepancies have been identified for M_2 in oceanic regions with strong ocean tides that move atmospheric pressure sensors attached to buoys or ships periodically to different geopotential heights: prominent examples are the signals in the Gulf of Alaska and around the British Isles. Those signals are neither present in free simulations of the lunar tide nor in global fields derived from properly corrected in situ observations (Schindelegger & Dobslaw, 2016).

To some extent, changes in the atmospheric tides on interannual to decadal scales have been also studied for both S_1 (Schindelegger *et al.*, 2016) and S_2 (Dìaz-Argandoña *et al.*, 2016). Changes from year to year are present in all global atmospheric reanalysis data sets considered, but they deviate strongly when compared to each other. Further research should be devoted to the assessment of interannual changes of atmospheric tides in particular also in the context of long-term changes in atmospheric composition and temperature, but in view of the demonstrated sensitivity of the ECMWF assimilation suite to changes in the observing system, it is likely that all the tidal variations seen in the current global atmospheric data-sets still contain systematic errors; see, e.g., Sterl (2004) for a detailed discussion of the consequences of low observation density at middle-to-polar latitudes in global atmospheric reanalyses. Moreover, spurious tidal structures may emerge when predefined assimilation techniques respond to abrupt changes in the types and volumes of observations. Robertson *et al.* (2011) provide evidence that the introduction of new satellite data typically results in perturbations of energy fluxes and modelled moisture, which are important variables in the generation of the diurnal atmospheric tide. In-situ data might be considered as the more reliable and robust source for tidal signals, yet the sampling over several critical areas (equatorial oceans, Amazon, Central Africa) is quite sparse to accurately constrain atmospheric models by an observed tide.

Based on a thorough pre-assessment of the tidal signals in the ECMWF data-set to be used for AOD1B, we selected the following strategy to cope with atmospheric tides in AOD1B RL06:

- In total 12 tidal frequencies are estimated and removed from the ECMWF surface pressure.

This includes the main solar tides S_1, S_2, and S_3 as well as the main semidiurnal lunar tide M_2. For each of the four central frequencies two additional side-bands are estimated in order to also account for potential seasonal or monthly modulations (Tab. 5.1).

- Tidal signals are estimated for the period 2007 – 2014, which is the part of the AOD1B reference period where ECMWF operational model data at a spatial resolution of T799 or better has been used. Tidal signals estimated from that period are subtracted from all atmospheric surface pressure grids of the years 2007 and later. The fitted atmospheric tidal signals are, however, provided as separate sets of coefficients, so that any of the removed signals might be restored.

- Since interannual variations in atmospheric tides have been found to be less reliable in older years, tidal signals at the 12 selected frequencies have been estimated and removed for each year separately before 2007.

5.2 Removed Tidal Signals From a Fit Over 2007 – 2014

In total, 12 frequencies are considered to be relevant for the removal of atmospheric tides. Here, we employ standard oceanographic naming conventions introduced by Arthur Thomas Doodson, which consequently implies to label the main semi-diurnal lunar tide as M_2. Note that in the meteorologic or aeronomic literature, this frequency is often labelled as L_2. For the naming conventions of S_3 modulations, we follow the suggestions by Ray & Poulose (2005), phase conventions applied for S_1 are consistent with Ray & Egbert (2004). The tidal arguments applied are given in Tab. 5.1 where t is mean solar time at Greenwich, s mean longitude of the moon, h mean longitude of the sun, p longitude of the moon's mean perigee, and p' the longitude of the sun's mean perigee. Note that mean solar time t is related to the frequently considered mean lunar time τ via $t = \tau + s - h$ (Sidorenkov, 2009, p. 70).

In preparation of the tidal analysis, atmospheric surface pressure anomalies over the period 2007 – 2014 are highpass-filtered with a 3rd order Butterworth filter with a cutoff period of 3 days and sine and cosine components for each frequency are estimated from a least-squares fit (Fig. 5.1). Tidal signals of S_1 and S_2 exceed 1 hPa in many regions and are largely consistent with previous knowledge on atmospheric tides both based on alternative numerical models and in situ observation compilations (Fig. 5.1). Signals for both S_3 and M_2 are substantially smaller and reach amplitudes of about 10 Pa only. Similar amplitudes are also obtained for the side-bands, where in particular T_3 and R_3 reveal coherent global pattern.

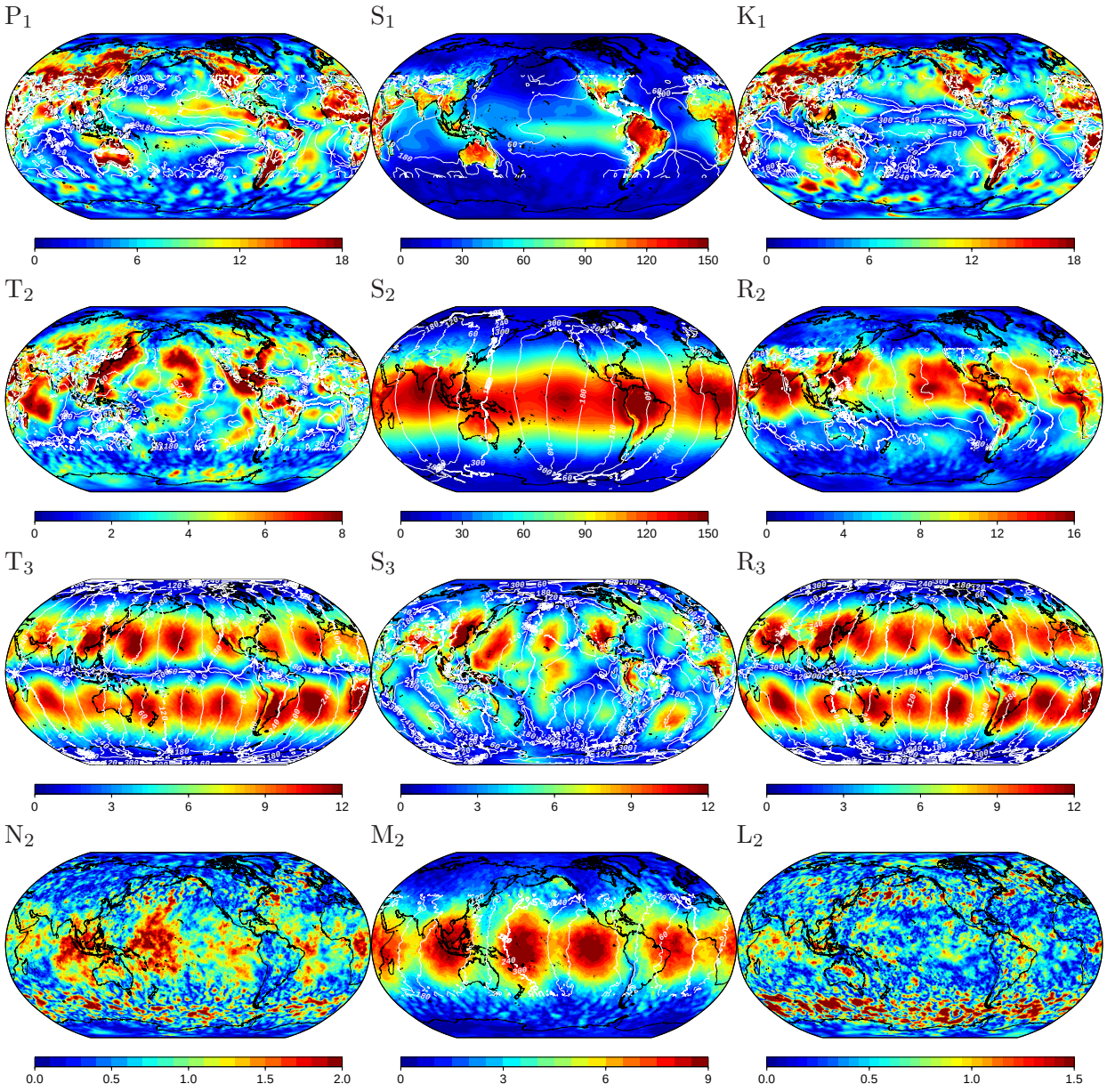

Figure 5.1: Surface pressure signals of atmospheric tides [Pa] for the triplets (P_1-S_1-K_1), (T_2-S_2-R_2), (T_3-S_3-R_3), and (N_2-M_2-L_2) removed from AOD1B as estimated over the period 2007 – 2014.

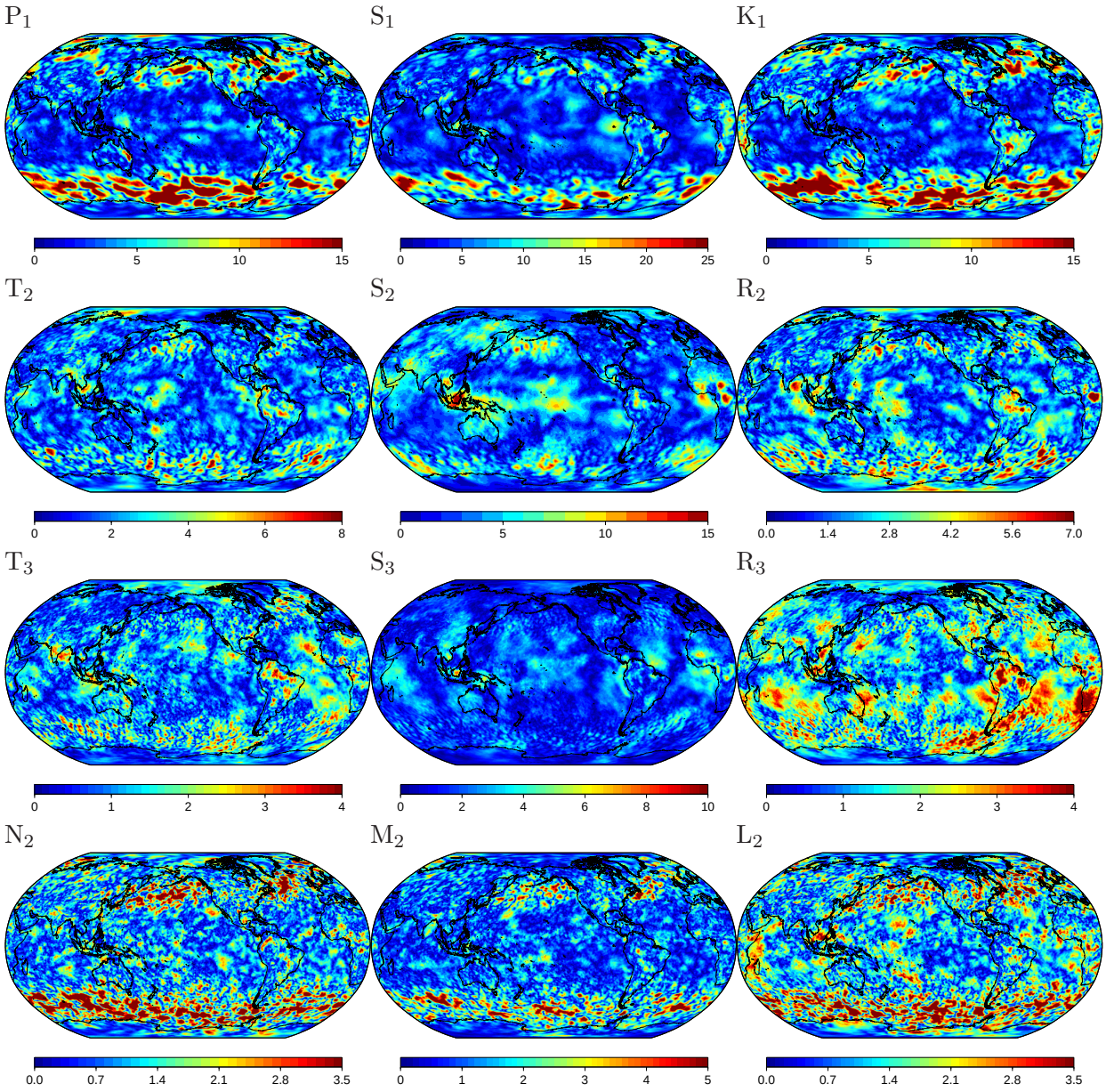

Figure 5.2: Residual surface pressure signals of atmospheric tides [Pa] for the triplets (P_1-S_1-K_1), (T_2-S_2-R_2), (T_3-S_3-R_3), and (N_2-M_2-L_2) contained in AOD1B as estimated over the year 2007.

5.3 Residual Tidal Amplitudes in 2007 and 2015

To test the efficacy of our selected approach to estimate and remove tides, we repeat the tidal analysis on the de-tided pressure grids for the years 2007 (Fig. 5.2) and 2015 (Fig. 5.3) separately. Residual tidal variability is now well below 30 Pa for all frequencies considered and is concentrated in regions of strong high-frequency non-tidal variability. We therefore perceive this remaining variability in the non-tidal AOD1B coefficients as plausible variations in the air tides from year to year. Note that residual tidal signals for years prior to 2007 are larger (not shown), so that removing tidal signals for each year individually was indeed necessary.

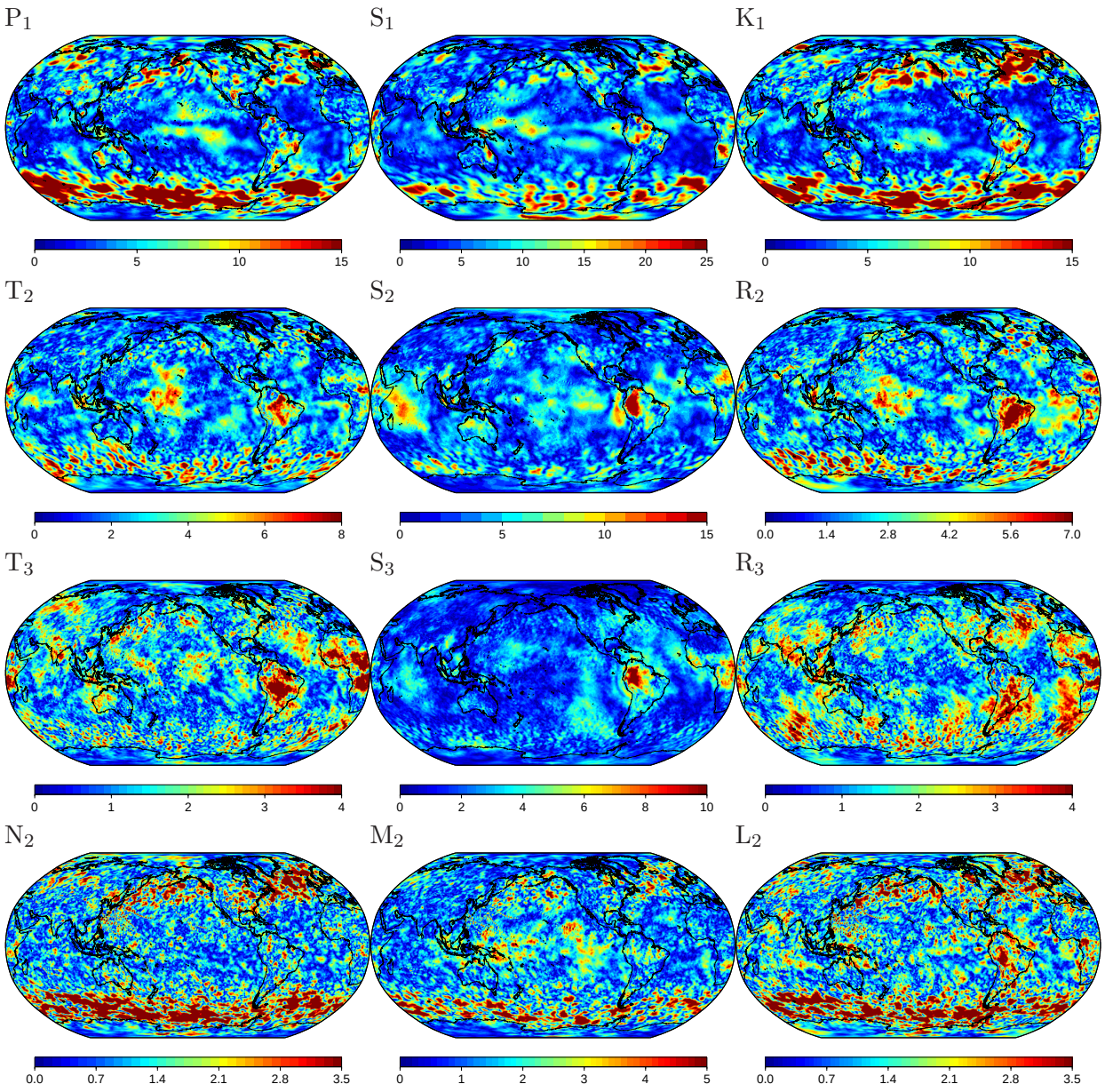

Figure 5.3: Residual surface pressure signals of atmospheric tides [Pa] for the triplets (P_1-S_1-K_1), (T_2-S_2-R_2), (T_3-S_3-R_3), and (N_2-M_2-L_2) contained in AOD1B as estimated over the year 2015.

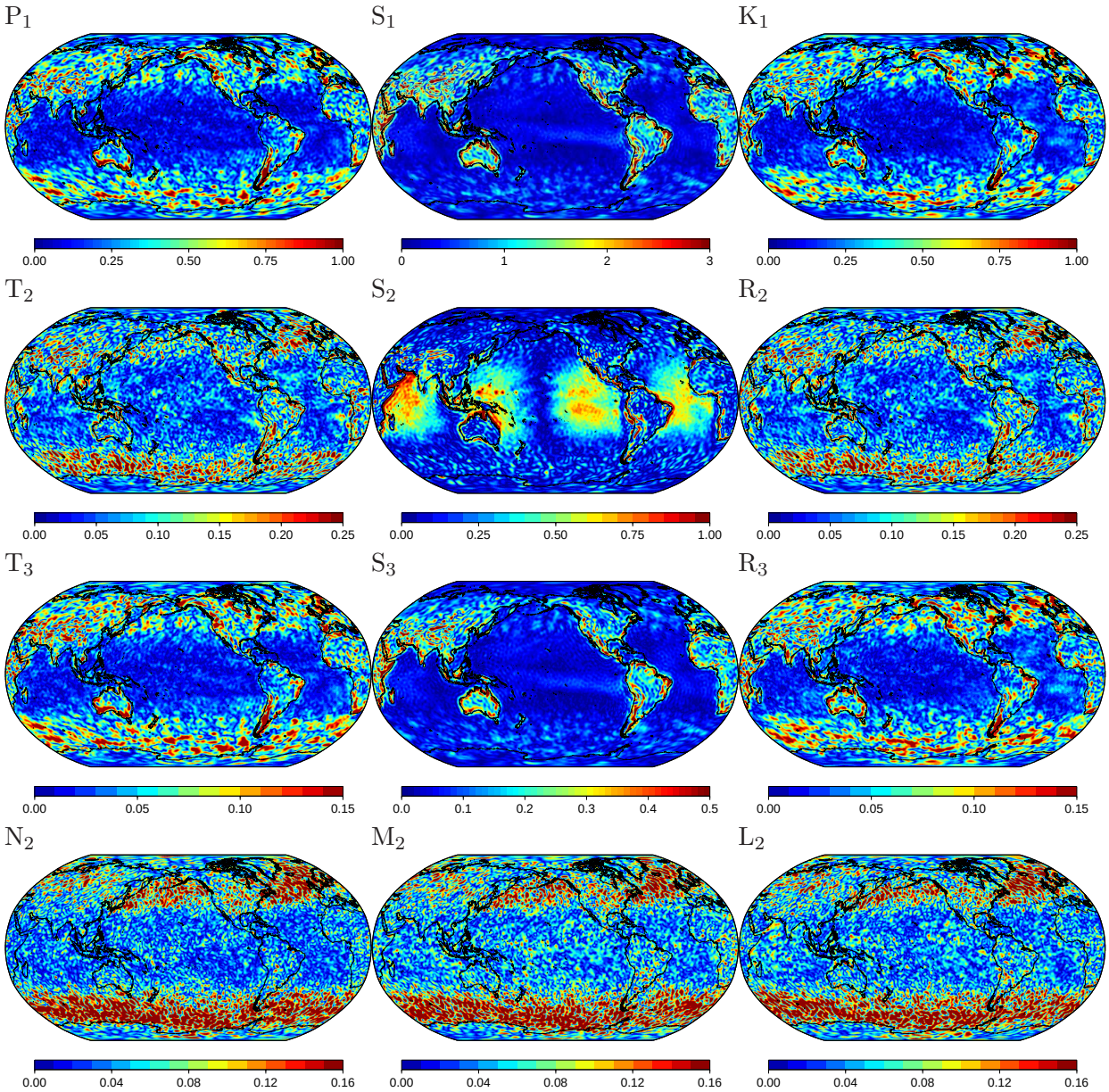

Figure 5.4: Residual signals of atmospheric tides contained in upper-air density anomalies as expressed in equivalent surface pressure [Pa] for the triplets (P_1-S_1-K_1), (T_2-S_2-R_2), (T_3-S_3-R_3), and (N_2-M_2-L_2) contained in AOD1B as estimated over the year 2015.

5.4 Tidal Signals caused by Upper-Air Density Anomalies

For completeness, we also test for the presence of tidal signals in the contributions of upper-air density anomalies to changes in the Earth's gravity field (Fig. 5.4) as introduced in Ch. 4. Tidal signals in the re-synthesized coefficients expressed in equivalent surface pressure anomalies are always well below 1 Pa, thereby confirming that tidal variability of upper-air density can be safely neglected for satellite gravimetry applications.

Chapter 6

Simulated Ocean Response to Atmospheric Tides

6.1 Reproduction of Tidal Variability in OGCMs

Periodic changes in atmospheric surface pressure over the oceans pose a time-variable loading to the water column that is not fully compensated isostatically, but excite a periodic motion in the oceans itself that adds to field of lunisolar gravitational ocean tides. The MPIOM simulation used for AOD1B RL06 is forced with atmospheric conditions including atmospheric surface pressure obtained from ECMWF. By doing so, the oceanic response to atmospheric tides is simulated together with the transient non-tidal ocean circulation variability. However, the quality of the simulated tidal fields is affected by a number of limitations in the modeling approach as outlined below:

(i) The atmospheric forcing is applied only every 3 hours and interpolated linearly to the internal model time-step so that atmospheric pressure variability at tidal frequencies is somewhat underestimated in many areas depending on the actual phase of the tidal wave in relation to the time-stepping of the atmospheric forcing. (ii) The spatial resolution of MPIOM is only 1° on average, which is very coarse compared to current state-of-the-art tidal simulations. In particular the dynamics in semi-enclosed seas are often only poorly represented in such a setting. (iii) Currently available model data-sets of the global ocean tides are either based on a combination of observations from satellite altimetry and other sources (GOT4.7, EOT11a); or hydrodynamic simulations that assimilate altimetry, gravimetry, or even tide gauge data (FES2014). MPIOM simulations for AOD1B, instead, do not assimilate any data but are governed by the applied atmospheric forcing only.

In view of those limitations, we remove all tidal variability from the ocean component of AOD1B in the same way as for the atmospheric part. The fitted signals are once more provided as separate sets of coefficients, so that any of the removed signals might be restored.

6.2 Removed Tidal Signals From a Fit Over 2007 – 2014

Tidal variations in ocean bottom pressure in response to the atmospheric tides are strongest for S_1 and in particular S_2, where amplitudes of up to 4 hPa are simulated in various coastal regions of both Pacific and Indian Ocean (Fig. 6.1). Seasonal modulations are strongest for the diurnal solar tides (P_1, K_1) with signals approaching 30 Pa in various regions, but also the ter-diurnal signals (T_3, R_3) reveal large-scale features that are sometimes even stronger than the signal at the central frequency S_3.

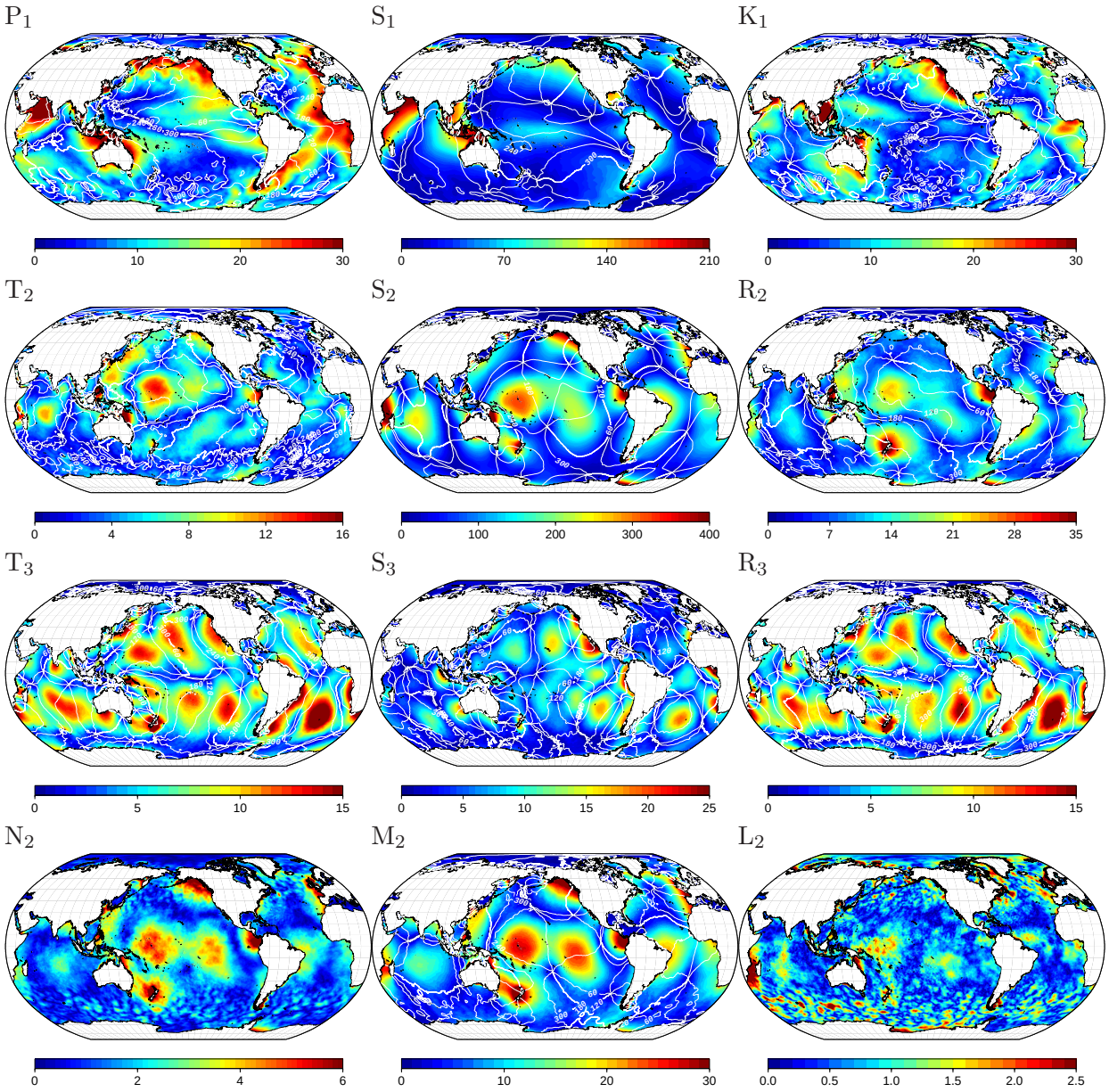

Figure 6.1: Ocean tides simulated in response to the atmospheric tides [Pa] for the triplets (P_1-S_1-K_1), (T_2-S_2-R_2), (T_3-S_3-R_3), and (N_2-M_2-L_2) removed from AOD1B as estimated over the period 2007 – 2014.

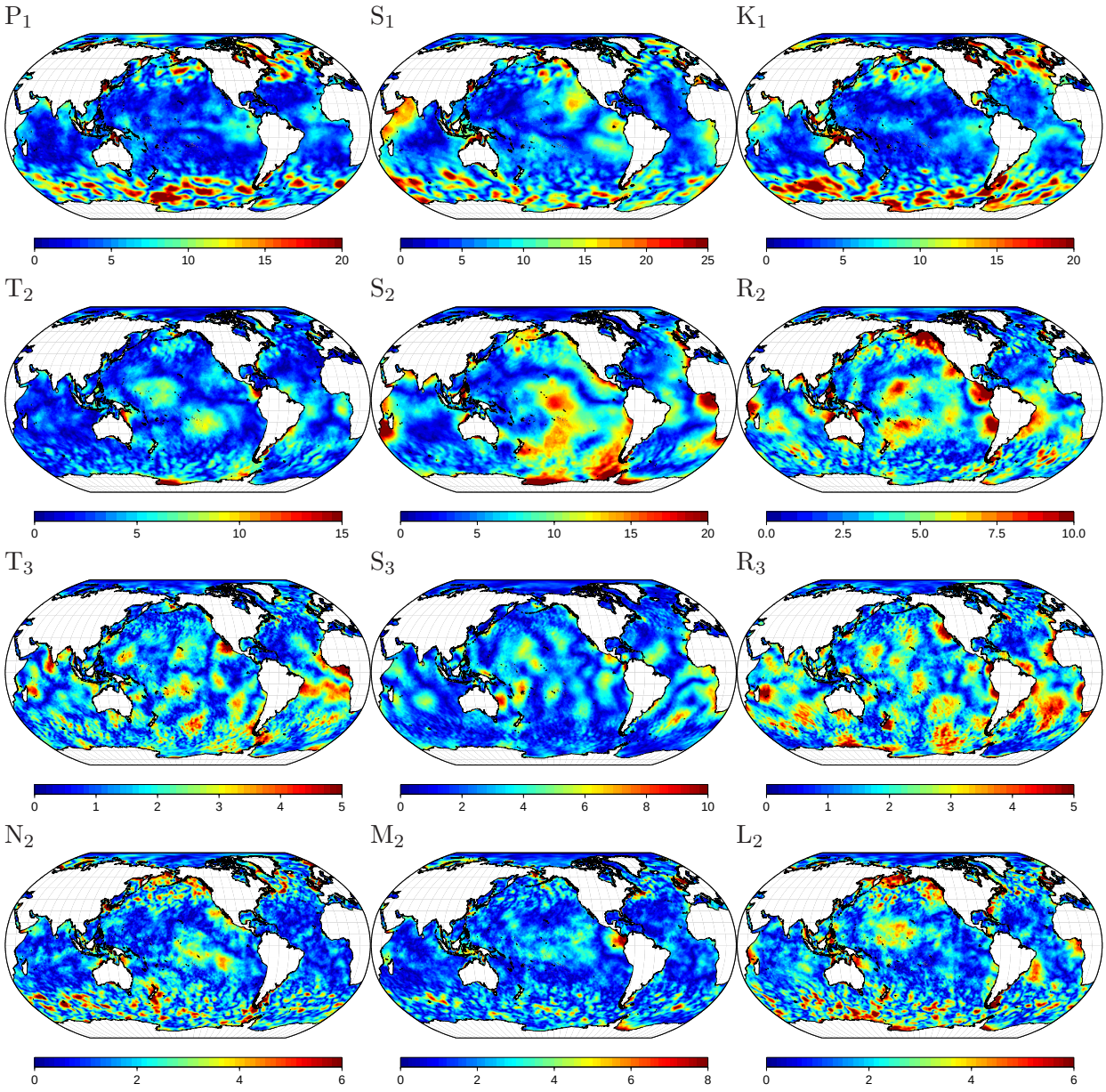

Figure 6.2: Residual ocean tide signals simulated in response to the atmospheric tides [Pa] for the triplets (P_1-S_1-K_1), (T_2-S_2-R_2), (T_3-S_3-R_3), and (N_2-M_2-L_2) contained in AOD1B as estimated over the year 2007.

6.3 Residual Tidal Amplitudes in 2007 and 2015

To test the efficacy of our selected approach to estimate and remove tides, we repeat the tidal analysis on the de-tided pressure grids for the years 2007 (Fig. 6.2) and 2015 (Fig. 6.3) separately. Residual tidal variability is now well below 30 Pa for all frequencies considered and is particularly concentrated in regions of strong high-frequency non-tidal ocean variability. We therefore perceive this remaining variability in the non-tidal AOD1B coefficients as plausible variations in ocean tides in response to the air tides from year to year. Note that residual tidal signals for years prior to 2007 are larger (not shown), so that removing tidal signals for each year individually was indeed necessary.

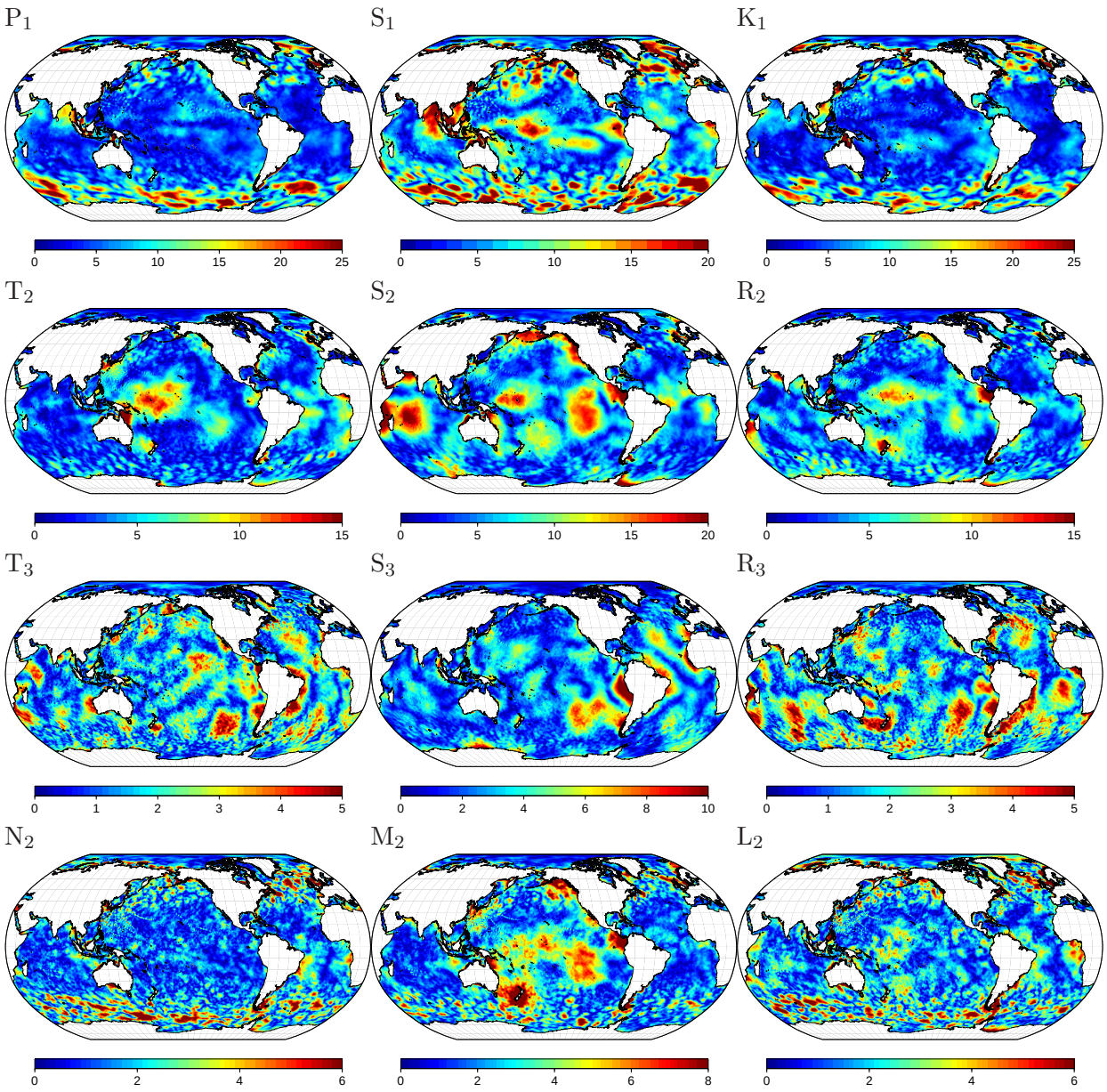

Figure 6.3: Residual ocean tide signals simulated in response to the atmospheric tides [Pa] for the triplets (P_1-S_1-K_1), (T_2-S_2-R_2), (T_3-S_3-R_3), and (N_2-M_2-L_2) contained in AOD1B as estimated over the year 2015.

Chapter 7

AOD1B Low-Degree Stokes Coefficients

7.1 ATM and GAA Stokes Coefficients

The AOD1B non-tidal coefficients are provided in four individual components denoted as ATM, OCN, GLO, and OBA. The effects of the atmosphere are contained in the ATM coefficients that include the contribution of atmospheric surface pressure over the continents (Sect. 2.2); the static contribution of atmospheric pressure to ocean bottom pressure elsewhere (Sect. 2.4); and the much weaker contribution of upper-air density anomalies above both continents and oceans (Ch. 4). The monthly-means of the ATM coefficients are routinely provided together with the GRACE Level-2 gravity fields as GAA products.

Exemplarily, we provide time-series plots of the ATM low-degree spherical harmonic coefficients over the period 1976 – 2015 that are available from AOD1B RL06 (Fig. 7.1, 7.2, and 7.3). Variability in C_{00} is substantially stronger during the years 1976 – 1978 where ERA-40 data has been applied. We further note a gradual increase in atmospheric mass in particular during the 1990'ies, but do not find any apparent jumps or inconsistencies. Similar conclusions are also drawn for the other coefficients.

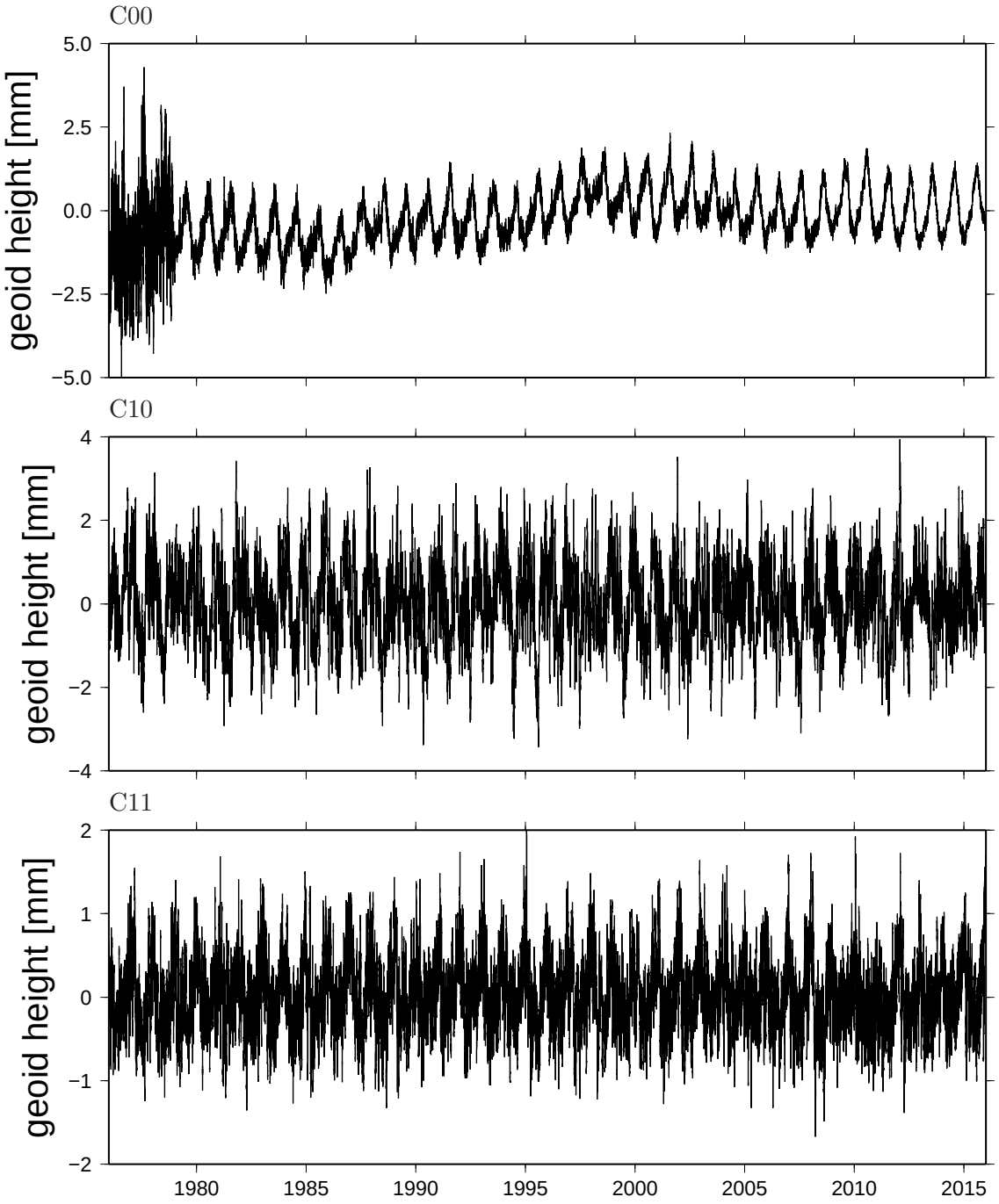

Figure 7.1: Time Series of ATM low-degree Stokes coefficients C_{00}, C_{10} and C_{11} of AOD1B.

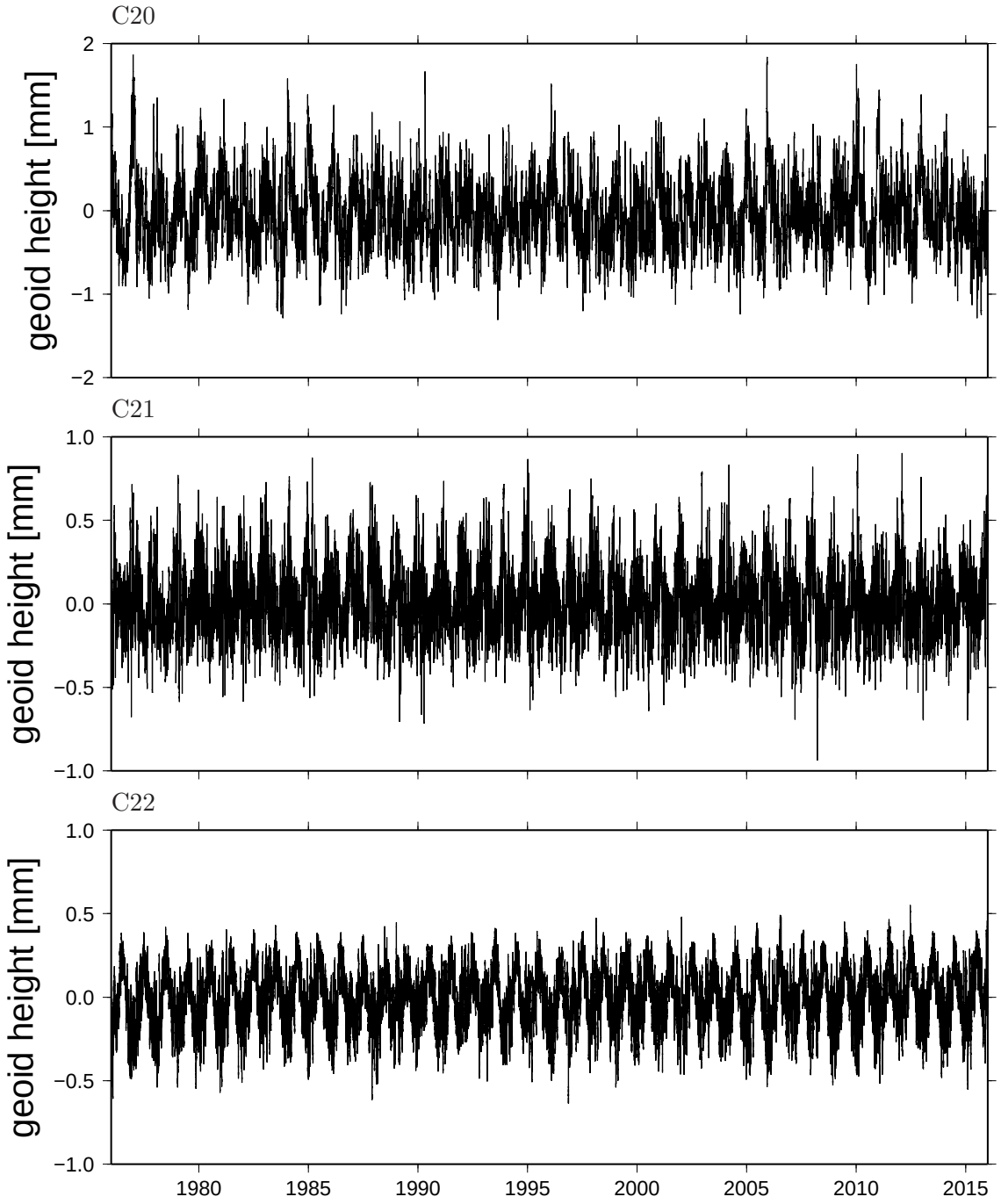

Figure 7.2: Time Series of ATM low-degree Stokes coefficients C_{20}, C_{21} and C_{22} of AOD1B.

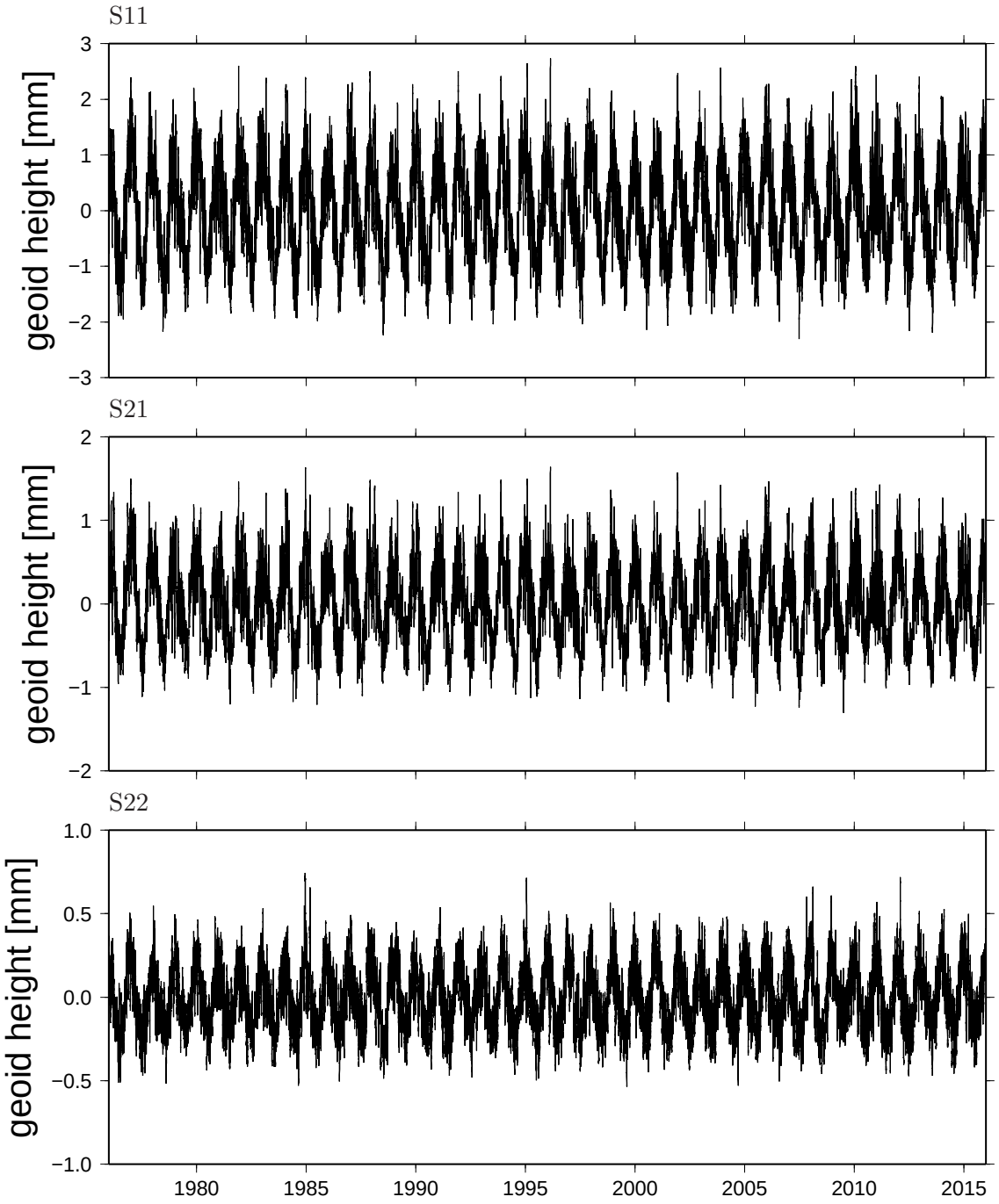

Figure 7.3: Time Series of ATM low-degree Stokes coefficients S_{11}, S_{21} and S_{22} of AOD1B.

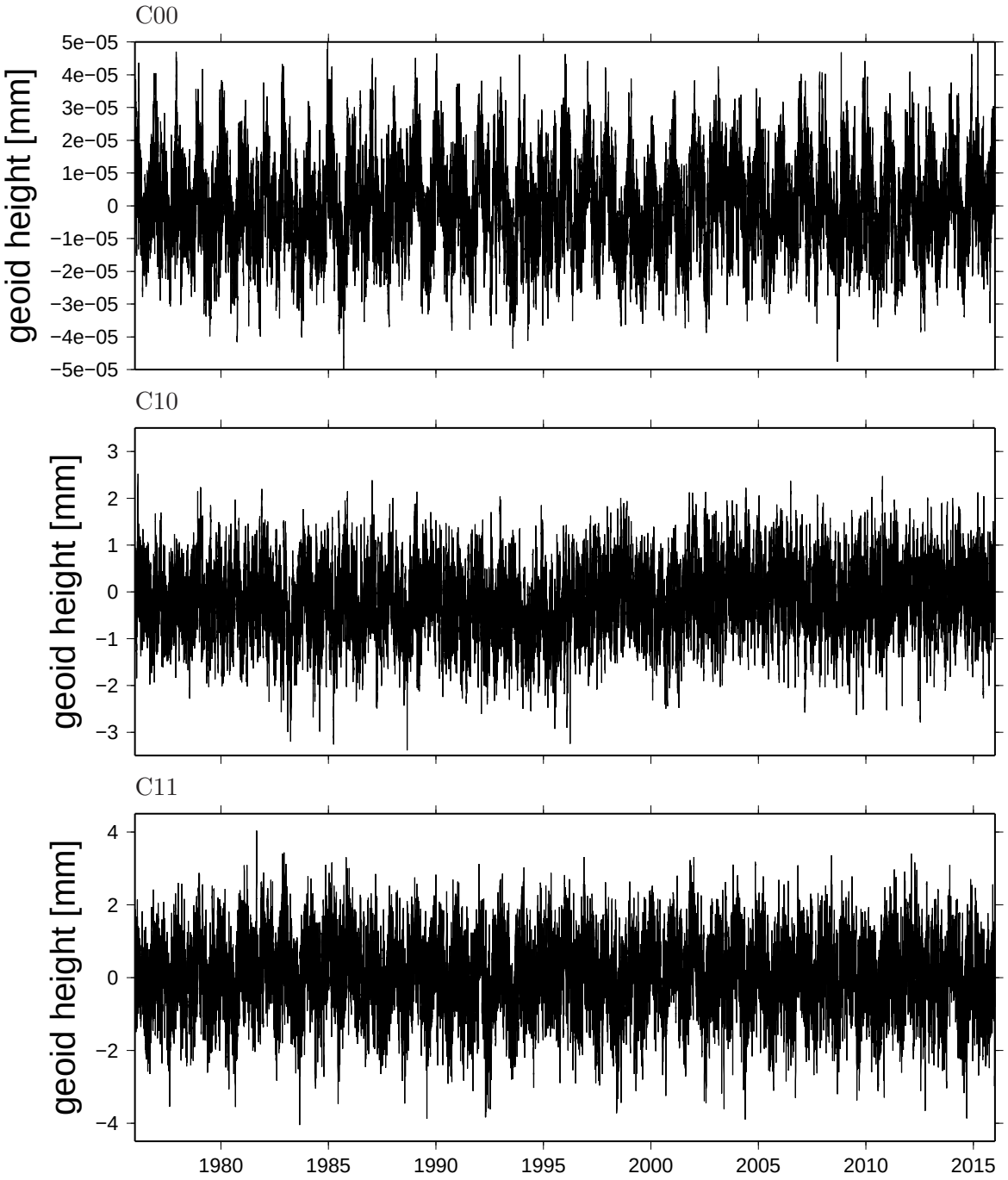

Figure 7.4: Time Series of OCN low-degree Stokes coefficients C_{00}, C_{10} and C_{11} of AOD1B.

7.2 OCN and GAB Stokes Coefficients

The contribution of the dynamic ocean to ocean bottom pressure is provided as OCN as discussed in Ch. 3. The monthly-means of the OCN coefficients are routinely provided together with each GRACE Level-2 gravity field as the GAB product. Note that the static contribution of the atmosphere to ocean bottom pressure is excluded here.

We display time-series plots of the low-degree spherical harmonic coefficients over the period 1976 – 2015 for OCN (Fig. 7.4, 7.5, and 7.6). Variability in C_{00} should be always zero due to the constraint imposed by applying eq. 3.1. Visual inspection of those coefficients displayed does not

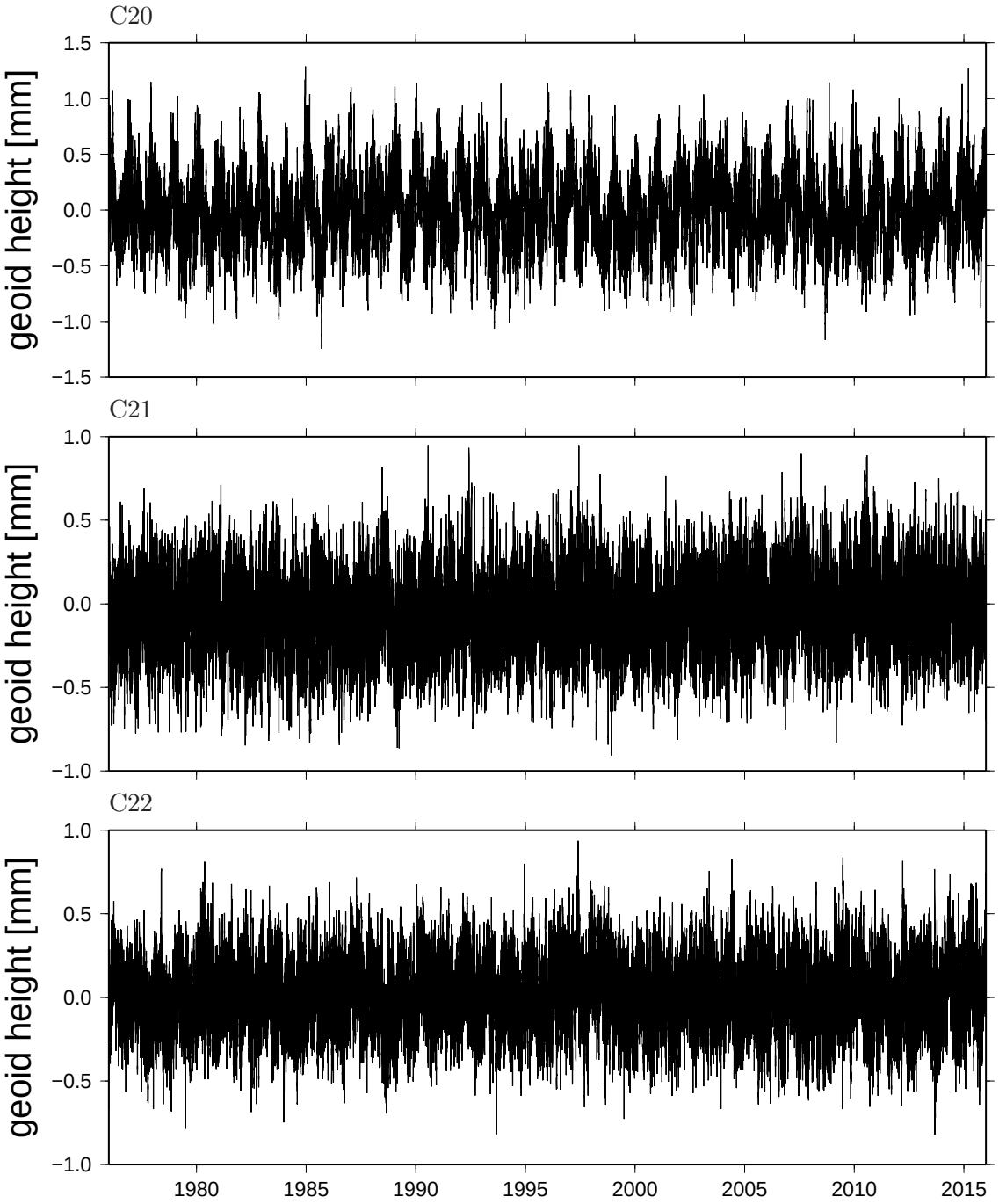

Figure 7.5: Time Series of OCN low-degree Stokes coefficients C_{20}, C_{21} and C_{22} of AOD1B.

reveal any apparent jumps or inconsistencies.

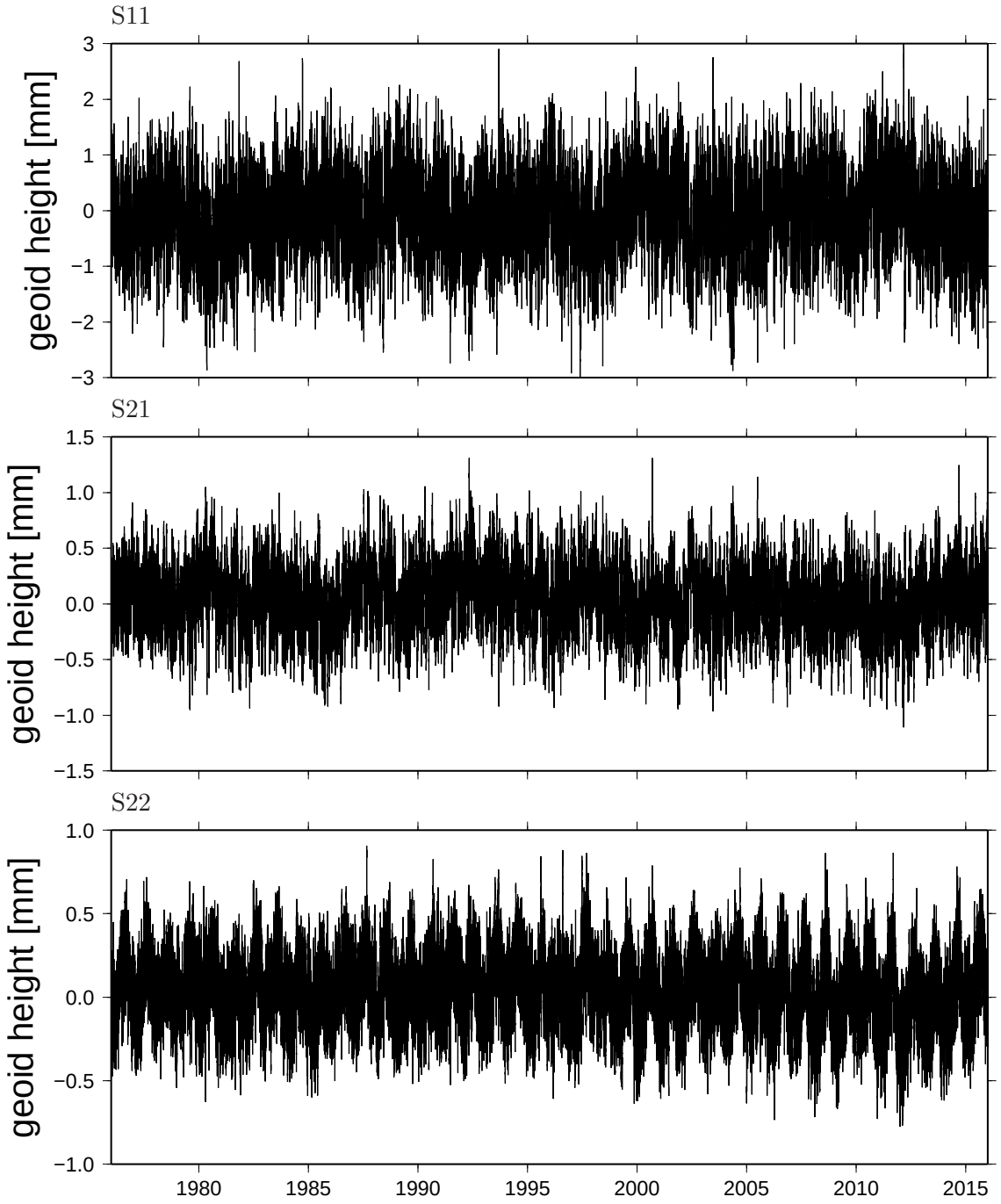

Figure 7.6: Time Series of OCN low-degree Stokes coefficients S_{11}, S_{21} and S_{22} of AOD1B.

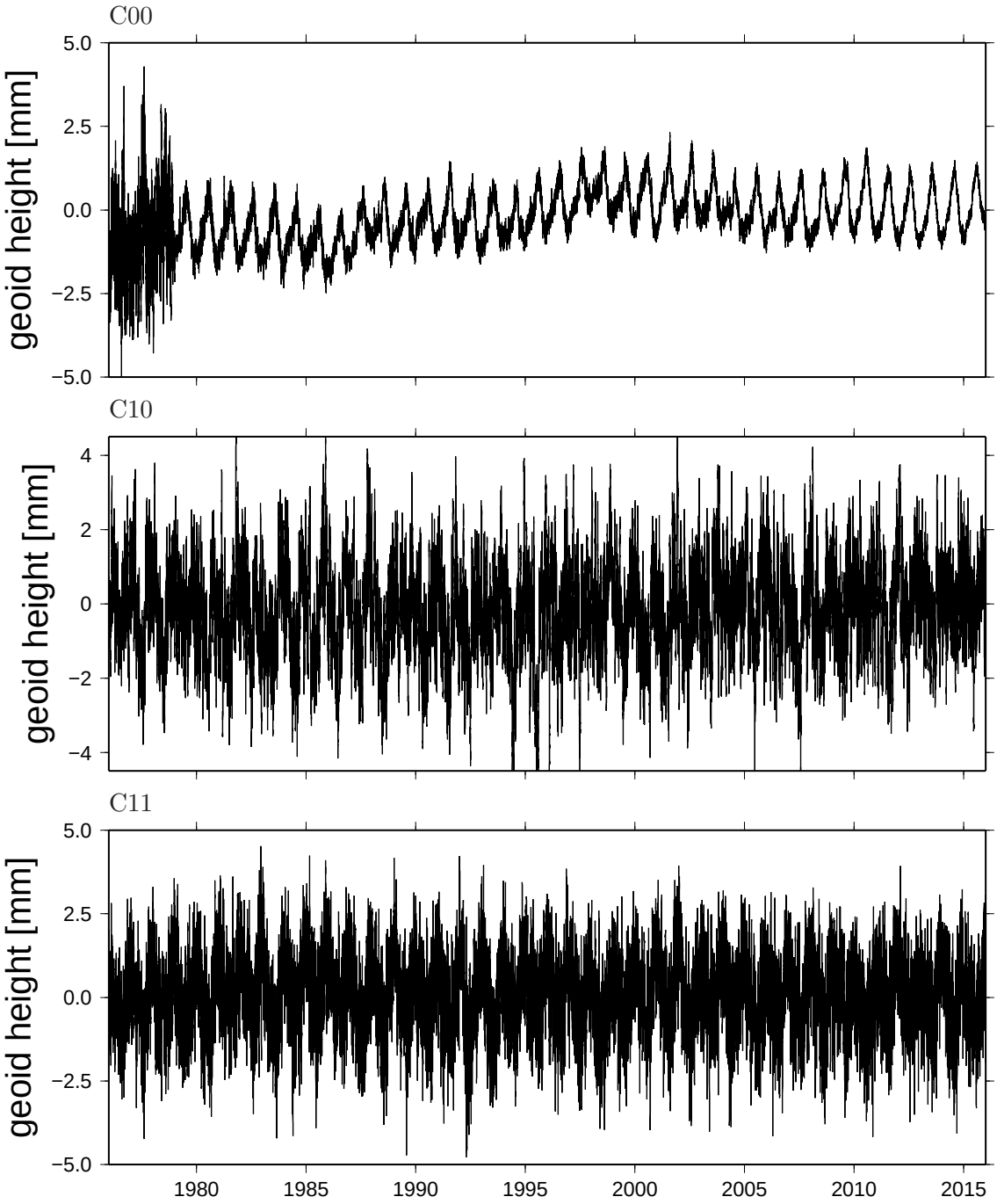

Figure 7.7: Time Series of GLO low-degree Stokes coefficients C_{00}, C_{10} and C_{11} of AOD1B.

7.3 GLO and GAC Stokes Coefficients

The GLO coefficients are obtained from the sum of ATM and OCN at coefficient level. Those coefficients are usually applied in precise orbit determination. The monthly-means of the GLO coefficients are routinely provided together with a GRACE Level-2 gravity fields as GAC products.

We provide here time-series plots of the low-degree spherical harmonic GLO coefficients over the period 1976 – 2015 (Fig. 7.7, 7.8, and 7.9). Variability in C_{00} reflects the time-variable atmospheric mass only. The inspection of the other coefficients displayed does not reveal any artefacts.

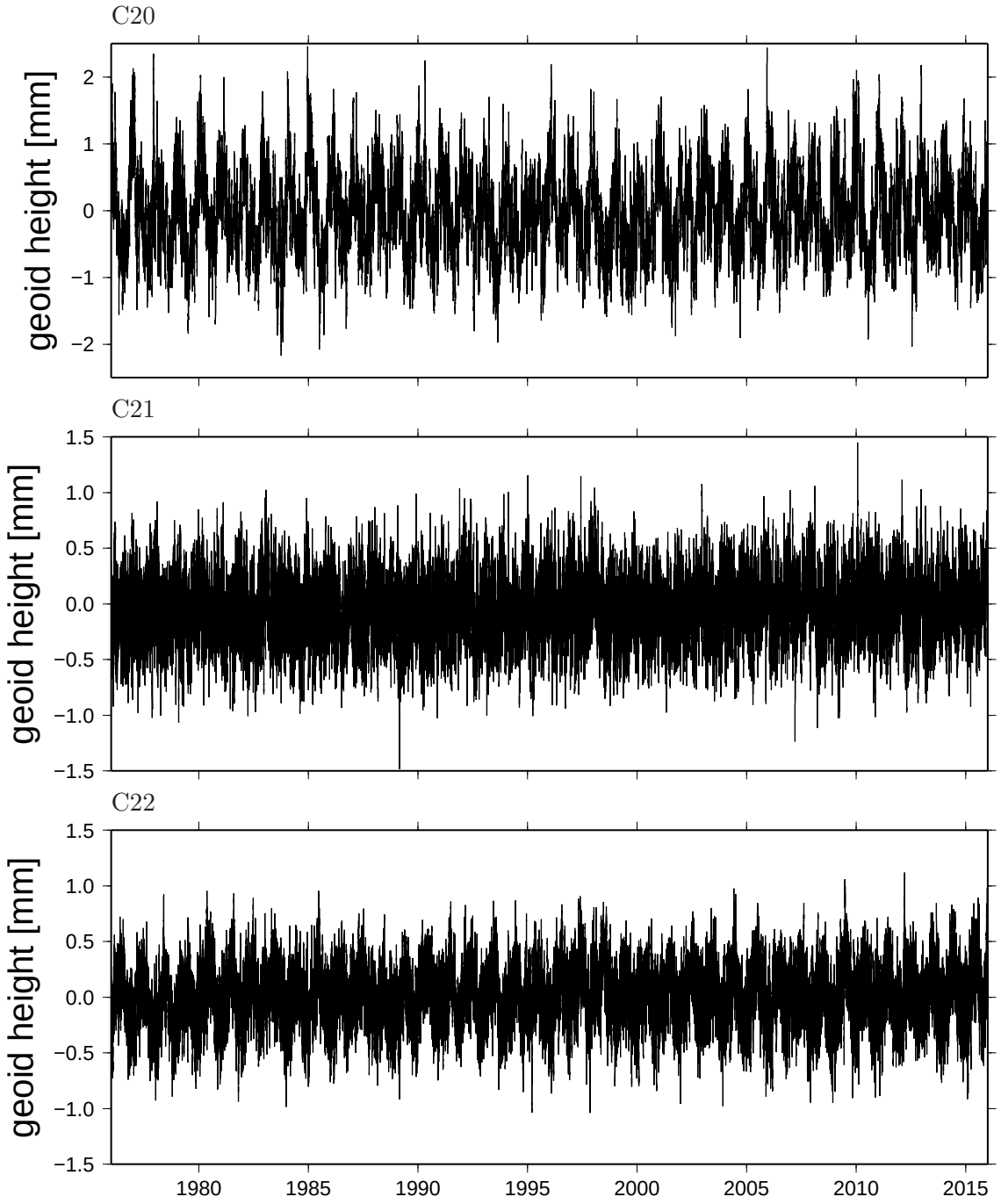

Figure 7.8: Time Series of GLO low-degree Stokes coefficients C_{20}, C_{21} and C_{22} of AOD1B.

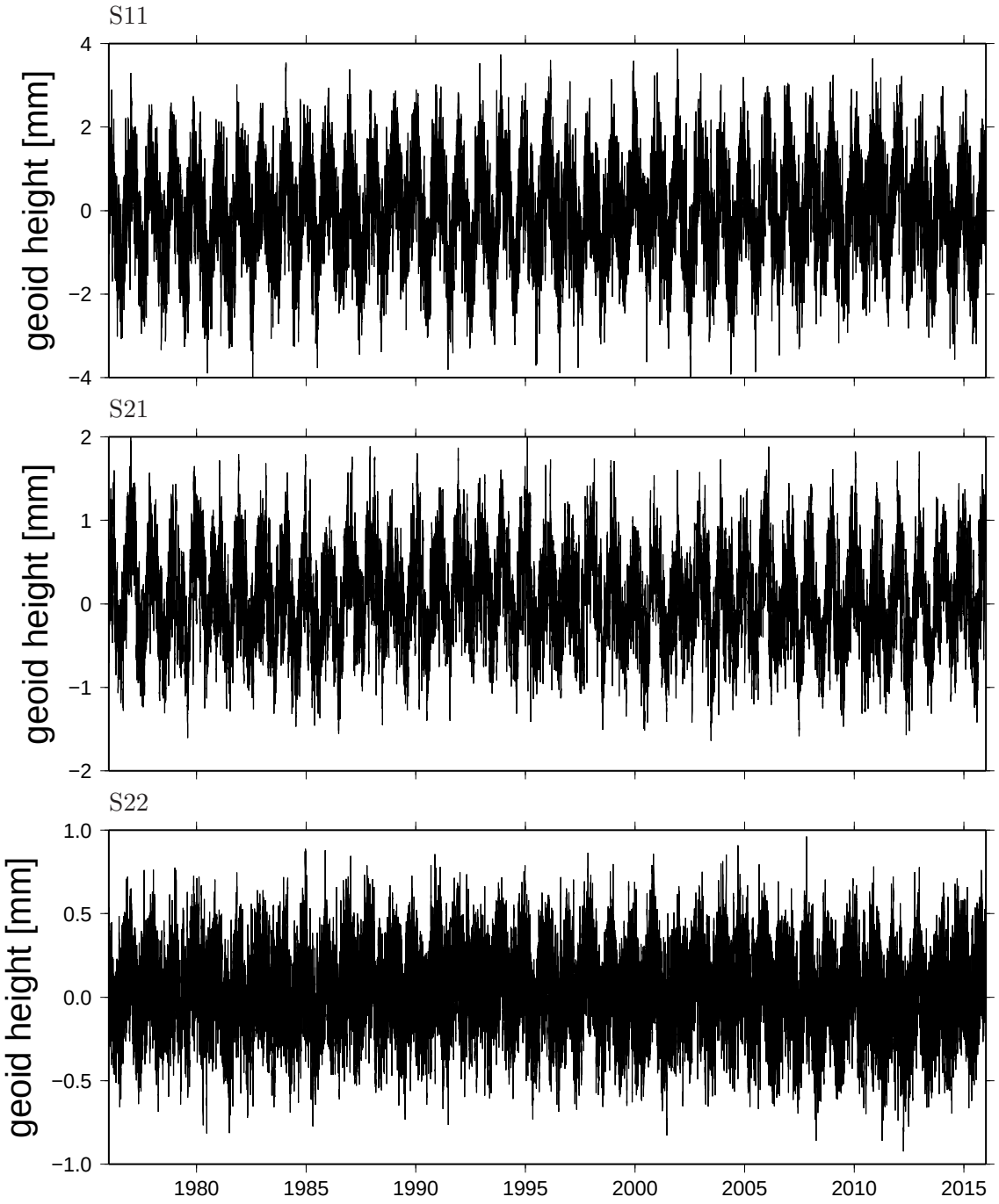

Figure 7.9: Time Series of GLO low-degree Stokes coefficients S_{11}, S_{21} and S_{22} of AOD1B.

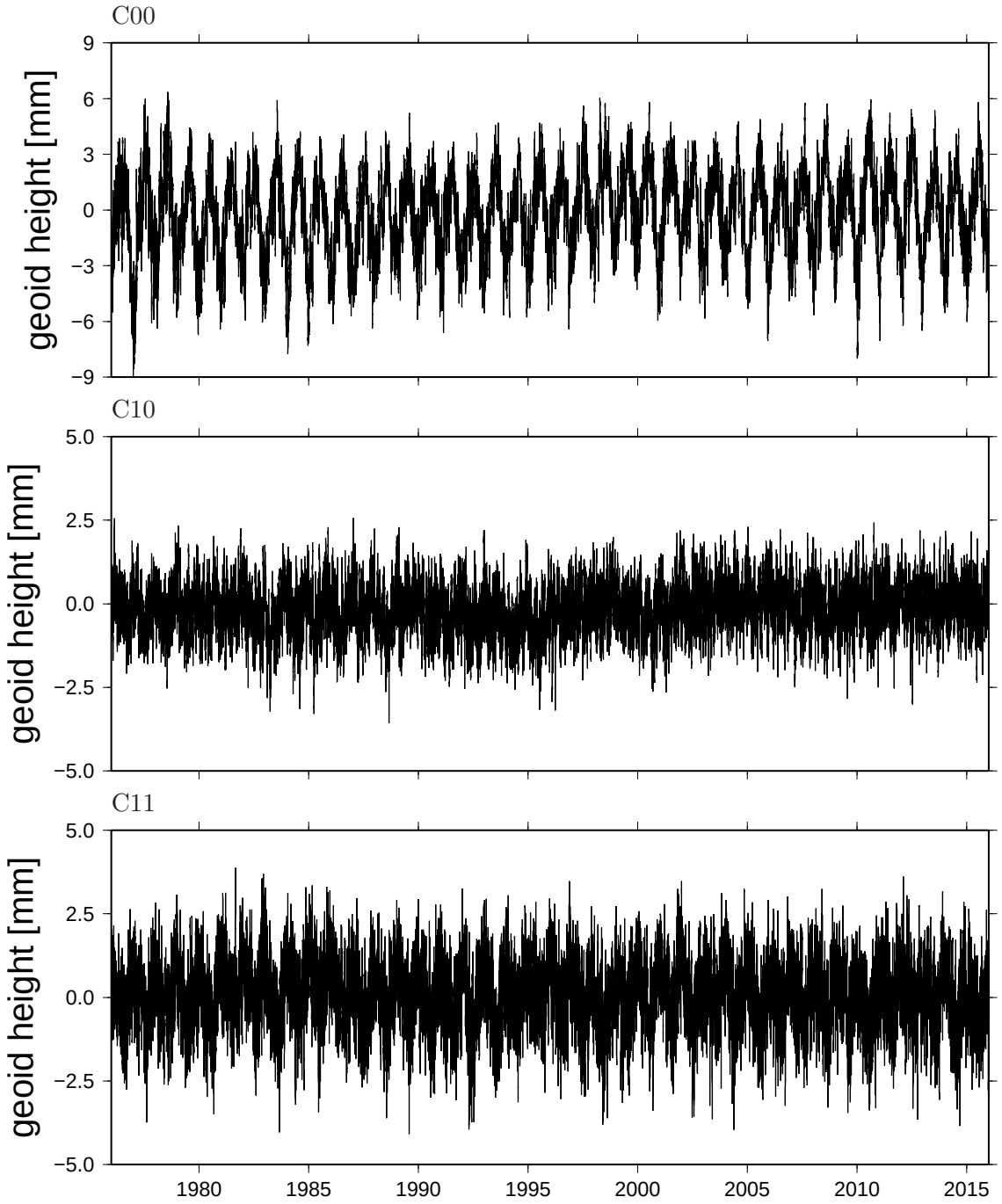

Figure 7.10: Time Series of OBA low-degree Stokes coefficients C_{00}, C_{10} and C_{11} of AOD1B.

7.4 OBA and GAD Stokes Coefficients

The fourth set of AOD1B coefficients, OBA, is zero over the continents and provides the simulated ocean bottom pressure that includes air and water contributions elsewhere. Thus, OBA deviates from GLO over the ocean domain only by disregarding the small contribution of upper-air density anomaly contributions to the external gravity field. The monthly-means of the OBA coefficients are routinely provided together with any GRACE Level-2 gravity field as GAD product.

Time-series plots of the low-degree spherical harmonic coefficients over the period 1976 – 2015 are provided also for OBA (Fig. 7.10, 7.11, and 7.12). No inconsistencies are identified.

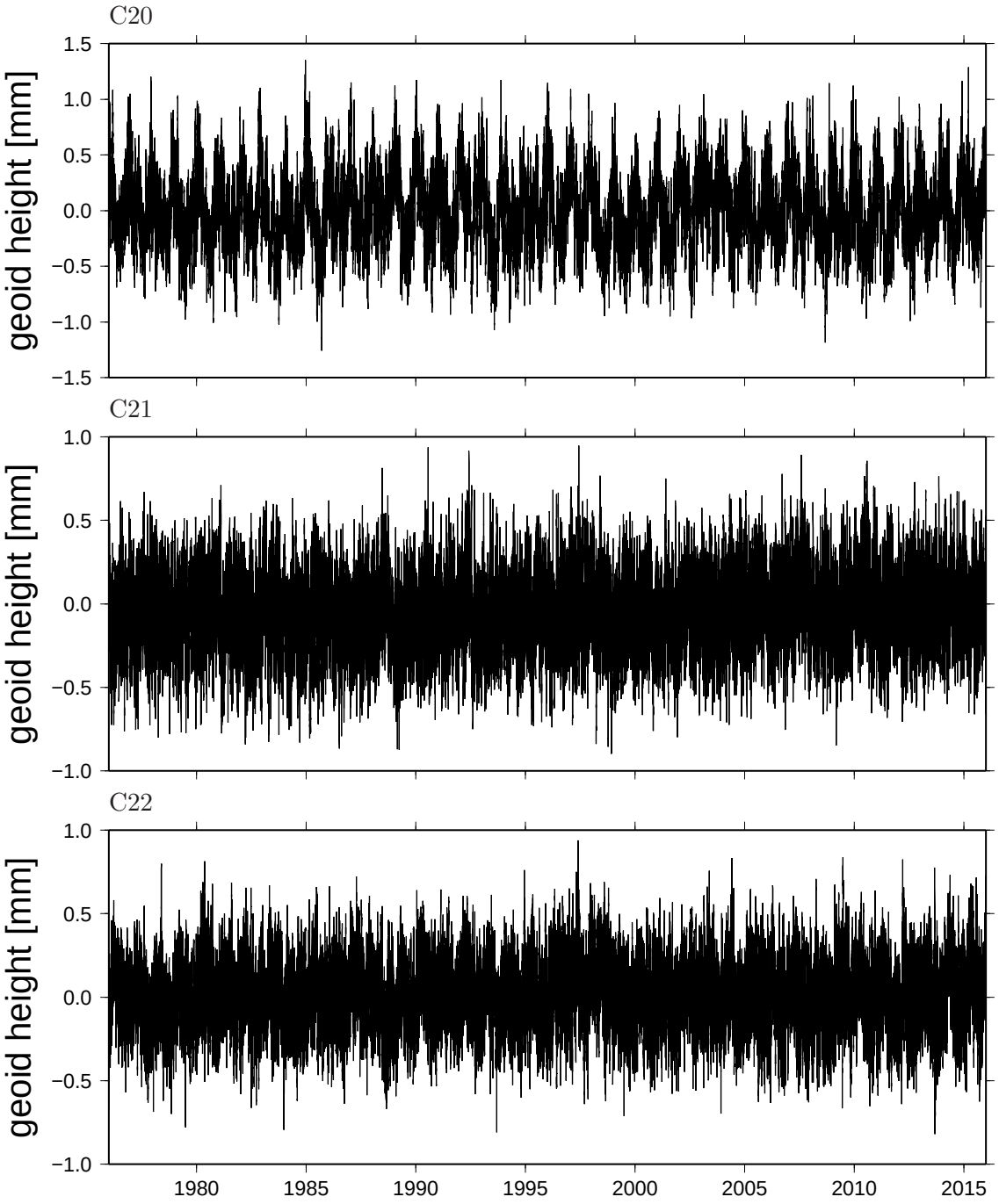

Figure 7.11: Time Series of OBA low-degree Stokes coefficients C_{20}, C_{21} and C_{22} of AOD1B.

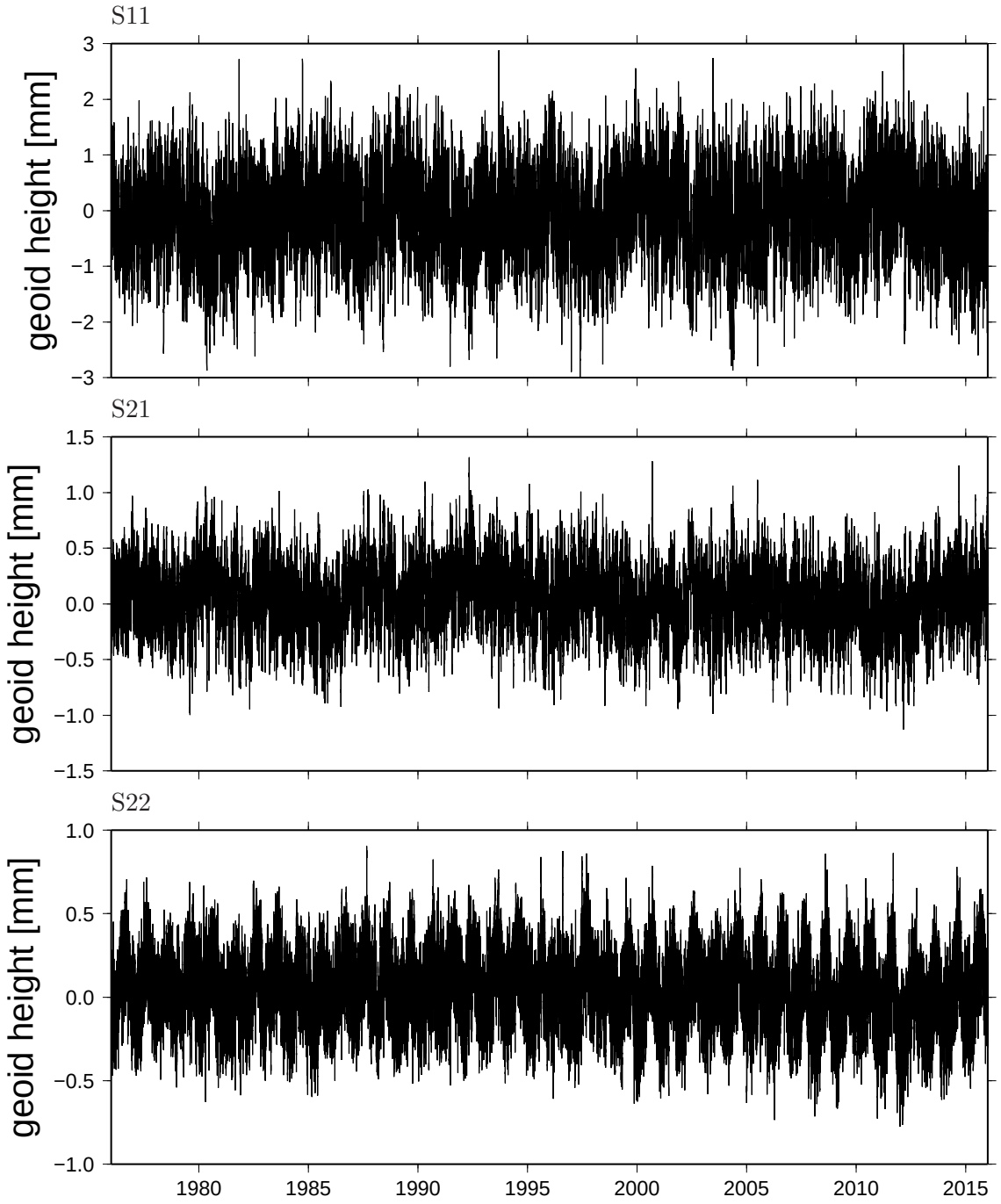

Figure 7.12: Time Series of OBA low-degree Stokes coefficients S_{11}, S_{21} and S_{22} of AOD1B.

Chapter 8

User Recommendations

8.1 AOD1B in Precise Orbit Determination

For the application of AOD1B as a time-variable background model in precise orbit determination, we recommend linear interpolation between two consecutive time-steps of the 3-hourly non-tidal GLO coefficients to arrive at the anomalous gravity field at an arbitrary time epoch.

We further recommend to apply additionally all 12 tidal lines of the atmospheric tides as discussed in Ch. 5. In case that atmospheric tidal models based on surface pressure station observations are readily available for selected frequencies as, e.g., presented by Schindelegger & Ray (2014) for S_1 and S_2, those might be given preference over the tidal signals provided with AOD1B. We do not, however, recommend applying models for time-varying atmospheric tides as discussed by Schindelegger *et al.* (2017), since variations in tidal signals from year to year are still included in the non-tidal AOD1B coefficients as explained in Sect. 5.3.

Generally, we do not recommend applying any of the 12 tidal lines of the oceanic response to atmospheric tides in precise orbit determination. It is assumed that the ocean response to atmospheric tides is part of the tidal signatures observed by satellite altimetry or oceanographic in situ stations like tide gauges or ocean bottom pressure sensors. Those observations are typically assimilated into global ocean tide models, and a global ocean tide model needs to be applied as a separate background model in any case.

8.2 Ocean Bottom Pressure and Sea-Level Variations

Users interested in deriving ocean bottom pressure variations out of the GRACE Level-2 coefficients are advised to re-add GAD to the monthly GSM gravity fields in order to restore the part of the monthly-mean bottom pressure signal removed during de-aliasing. The restore step should be performed only after applying non-isotropic filters as developed by, e.g., Swenson & Wahr (2006) or Kusche (2007) to the GSM coefficients. Note that effects from upper-air atmospheric density anomalies as described in Ch. 4 are not restored in this case, which are part of GAC but not part of GAD over oceanic regions.

In order to estimate mass-induced sea-level variations from the GRACE gravity fields, users should alternatively consider to re-add GAB instead of GAD. By doing so, only the gravitational signals of the ocean water masses are restored, whereas the IB-corrected effects of the atmospheric surface pressure and the contributions of upper-air atmospheric mass variability are kept separated. As recommended before, the restore step should be performed only after applying a non-isotropic filter

from Swenson & Wahr (2006) or Kusche (2007). In any case, we do not recommend restoring any of the tidal signals originating from oceans, atmosphere, or the solid Earth.

8.3 Global Mass Re-Distribution and Atmospheric Applications

Users specifically interested in studying global mass re-distributions in the Earth system including all mass variability in atmosphere and oceans from GRACE gravity fields are advised to re-add GAC to the monthly GSM products. The restore step should be performed only after applying non-isotropic filters as developed by, e.g., Swenson & Wahr (2006) or Kusche (2007) to the GSM coefficients. We do not recommend restoring any of the tidal signals originating from oceans, atmosphere, or the solid Earth.

For studies on atmospheric contributions to the time-variable gravity field, users are advised that the ATM coefficients and the corresponding monthly mean GAA products apply an inverse-barometric correction over the oceans (see Sect. 2.4), and are thus approximately comparable to in situ surface pressure observations only in continental regions away from the coasts.

8.4 Hydrospheric, Cryospheric, and Tectonic Applications

For typical hydrospheric, cryospheric, or tectonic applications, GRACE monthly GSM gravity field products can be used as delivered by the processing centers. There is no need to restore any of the signals removed during the de-aliasing process.

References

Beljaars, A. C. M. (1997). Air-sea interaction in the ECMWF model, Proc. of Seminar on Atmosphere-Surface Interaction, ECMWF, Reading, United Kingdom. 24

Bergmann, I. & Dobslaw, H. (2012). Short-term transport variability of the Antarctic Circumpolar Current from satellite gravity observations, *J. Geophys. Res.*, **117**, 1–12, *DOI*:10.1029/2012*JC*007872. 26

Bettadpur, S., Flechtner, F. & Schmidt, R. (2006). Technical Note 04 - Usage Guidelines for GFZ RL03 and JPL RL02 Grace Gravity Fields & Atmosphere/Ocean Background Models - Version 1.1, www.isdc.gfz-potsdam.de. 9

Blewitt, G. (2003). Self-consistency in reference frames, geocenter definition, and surface loading of the solid Earth, *J. Geophys. Res.*, **108**, *DOI*:10.1029/2002*JB*002082. 17

Boy, J.-P. & Chao, B. F. (2005). Precise evaluation of atmospheric loading effects on Earth's time-variable gravity field, *J. Geophys. Res.*, **110**, 1–10, *DOI*:10.1029/2002*JB*002333. 14

Case, K., Kruizinga, G. & Wu, S. (2002). *GRACE Level 1B Data Product User Handbook*, JPL Publication D-22027. 71, 73

Dee, D. P., Uppala, S. M., Simmons, A. J., Berrisford, P., Poli, P., Kobayashi, S., Andrae, U., Balmaseda, M. A., Balsamo, G., Bauer, P., Bechtold, P., Beljaars, A. C. M., van de Berg, L., Bidlot, J., Bormann, N., Delsol, C., Dragani, R., Fuentes, M., Geer, A. J., Haimberger, L., Healy, S. B., Hersbach, H., Hólm, E. V., Isaksen, L., K, P., Köhler, M., Matricardi, M., McNally, A. P., Monge-Sanz, B. M., Morcrette, J.-J., Park, B.-K., Peubey, C., de Rosnay, P., Tavolato, C., Thépaut, J.-N. & Vitart, F. (2011). The ERA-Interim reanalysis: configuration and performance of the data assimilation system, *Q. J. Roy. Meteor. Soc.*, **137**, 553–597, *DOI*:10.1002/*qj*.828. 10, 11

Dìaz-Argandoña, J., Ezcurra, A., Sáenz, J., Ibarra-Berastegi, G. & Errasti, I. (2016). Climatology and temporal evolution of the atmospheric semidiurnal tide and present-day reanalyses., *DOI*:10.1002/2015*JD*024513. 40

Dobslaw, H. (2016). Homogenizing surface pressure time-series from operational numerical weather prediction models for geodetic applications, *J. Geod. Sci.*, **6**, 61–68, *DOI*:10.1515/*jogs*-2016-0004. 12

Dobslaw, H., Bergmann-Wolf, I., Dill, R., Poropat, L., Thomas, M., Dahle, C., Esselborn, S., König, R. & Flechtner, F. (2017). A New High-Resolution Model of Non-Tidal Atmosphere and Ocean Mass Variability for De-Aliasing of Satellite Gravity Observations: AOD1B RL06, *Geophys. J. Int.*, **211**, 263–269, *DOI*:10.1093/*gji*/*ggx*302. 10

Dobslaw, H., Dill, R., Grötzsch, A., Brzeziński, A. & Thomas, M. (2010). Seasonal polar motion excitation from numerical models of atmosphere, ocean, and continental hydrosphere, *J. Geophys. Res.*, **115**, B10,406, *DOI*:10.1029/2009*JB*007127. 23

Dobslaw, H., Flechtner, F., Bergmann-Wolf, I., Dahle, C., Dill, R., Esselborn, S., Sasgen, I. & Thomas, M. (2013). Simulating high-frequency atmosphere-ocean mass variability for dealiasing of satellite gravity observations: AOD1B RL05, *J. Geophys. Res.*, **118**, 3704–3711, *DOI*:10.1002/*jgrc*.20271. 10, 23

Dobslaw, H. & Thomas, M. (2005). Atmospheric induced oceanic tides from ECMWF forecasts, *Geophys. Res. Lett.*, **32**, L10,615, *DOI*:10.1029/2005*GL*022990. 11

Dobslaw, H. & Thomas, M. (2007). Simulation and observation of global ocean mass anomalies, *J. Geophys. Res.*, **112**, C05,040, *DOI*:10.1029/2006*JC*004035. 9, 23

Dong, D., Gross, R. & Dickey, J. (1996). Seasonal variations of the Earth's gravitational field: An analysis of atmospheric pressure, ocean tidal, and surface water excitation, *Geophys. Res. Lett.*, **23**, 725–728, *DOI*:10.1029/96*gl*00740. 17

Drijfhout, S., Heinze, C., Latif, M. & Maier-Reimer, E. (1996). Mean Circulation and Internal Variability in an Ocean Primitive Equation Model, *J. Phys. Oceanogr.*, **26**, 559–580, *DOI*:10.1175/1520-0485(1996)026<0559:*MCAIVI*>2.0.*CO*;2. 23

Flechtner, F., Thomas, M. & König, R. (2008). *A long-term model for non-tidal atmospheric and oceanic mass redistributions and its implications on LAGEOS-derived solutions of Earth's oblateness (Scientific Technical Report STR ; 08/12)*, *Tech. rep.*, Potsdam: Deutsches GeoForschungsZentrum GFZ, *DOI*:10.2312/*GFZ*.*b*103-08123. 9

Greatbatch, R. (1994). A note on the representation of steric sea level in models that conserve volume rather than mass, *J. Geophys. Res.*, **99**, 12,767–12,771, *DOI*:10.1029/94*JC*00847. 25

Hasselmann, K. (2013). Ernst Maier-Reimer: The discovery of silence, *Nature Geoscience*, **6**, 809–809, *DOI*:10.1038/*ngeo*1953. 23

Heiskanen, W. & Moritz, H. (1967). *Physical Geodesy*, Freeman, San Francisco. 7

Hibler, W. (1979). A Dynamic Thermodynamic Sea Ice Model, *J. Phys. Oceanogr.*, **9**, 815–846, *DOI*:10.1175/1520-0485(1979)009<0815:*ADTSIM*>2.0.*CO*;2. 23

Hirose, N., Fukumori, I., Zlotnicki, V. & Ponte, R. (2001). Modeling the high-frequency barotropic response of the ocean to atmospheric disturbances: Sensitivity to forcing, topography, and friction, *J. Geophys. Res.*, **106**, 30,987–30,995, *DOI*:10.1029/2000*JC*000763. 9

Jungclaus, J. H., Fischer, N., Haak, H., Lohmann, K., Marotzke, J., Matei, D., Mikolajewicz, U., Notz, D. & von Storch, J. S. (2013). Characteristics of the ocean simulations in the Max Planck Institute Ocean Model (MPIOM) the ocean component of the MPI-Earth system model, *Journal of Advances in Modeling Earth Systems*, **5**, 422–446, *DOI*:10.1002/*jame*.20023. 7, 23

Kohyama, T. & Wallace, J. M. (2014). Lunar gravitational atmospheric tide, surface to 50 km in a global, gridded data set, *Geophys. Res. Lett.*, 8660–8665, *DOI*:10.1002/2014*GL*060818. 39

Kuhlmann, J., Dobslaw, H. & Thomas, M. (2011). Improved modeling of sea level patterns by incorporating self-attraction and loading, *J. Geophys. Res.*, **116**, C11,036, *DOI*:10.1029/2011*JC*007399. 23

Kusche, J. (2007). Approximate decorrelation and non-isotropic smoothing of time-variable GRACE-type gravity field models, *J. Geod.*, **81**, 733–749, *DOI*:10.1007/*s*00190-007-0143-3. 65, 66

Levitus, S. (2005). Warming of the world ocean, 1955–2003, *Geophys. Res. Lett.*, **32**, 1–4, *DOI*:10.1029/2004*GL*021592. 24

Maier-Reimer, E. & Mikolajewicz, U. (1992). *The Hamburg Large Scale Geostrophic Ocean General Circulation Model Cycle 1, Tech. Rep. 2*, Deutsches Klimarechenzentrum, Hamburg. 23

Marsland, S. J., Haak, H., Jungclaus, J., Latif, M. & Röske, F. (2003). The Max-Planck-Institute global ocean/sea ice model with orthogonal curvilinear coordinates, *Ocean Modelling*, **5**, 91–127, *DOI*:10.1016/*S*1463-5003(02)00015-*X*. 23

Notz, D., Haumann, F. A., Haak, H., Jungclaus, J. H. & Marotzke, J. (2013). Arctic sea-ice evolution as modeled by Max Planck Institute for Meteorology's Earth system model, *J. Adv. Model. Earth Sy.*, **5**, 173–194, *DOI*:10.1002/*jame*.20016. 23

Petit, G. & Luzum, B. (2010). *IERS Convention (2010) (IERS Technical Note no. 36), Tech. rep.*, Verlag des Bundesamtes für Kartographie und Geodäsie, Frankfurt am Main, URL http://www.iers.org/IERS/EN/Publications/TechnicalNotes/tn36.html. 14, 15

Ray, R. D. (1998). Ocean self-attraction and loading in numerical tidal models, *Marine Geodesy*, **21**, 181–192, *DOI*:10.1080/01490419809388134. 23

Ray, R. D. & Egbert, G. D. (2004). The Global S 1 Tide, *J. Phys. Oceanogr.*, **34**, 1922–1935, *DOI*:10.1175/1520-0485(2004)034<1922:*TGST*>2.0.*CO*;2. 41

Ray, R. D. & Ponte, R. M. (2003). Barometric tides from ECMWF operational analyses, *Annales Geophysicae*, **21**, 1897–1910, *DOI*:10.5194/*angeo*-21-1897-2003. 9

Ray, R. D. & Poulose, S. (2005). Terdiurnal surface-pressure oscillations over the continental United States, *Mon. Weather Rev.*, **133**, 2526–2534, *DOI*:10.1175/*MWR*2988.1. 41

Reigber, C., Balmino, G., Schwintzer, P., Biancale, R., Bode, A., Lemoine, J.-M., Ko, R., Loyer, S., Neumayer, K.-H., Marty, J.-C., Barthelmes, F., Perosanz, F. & Zhu, S. Y. (2002). A High-Quality Global Gravity Field Model from CHAMP GPS Tracking Data and Accelerometry (EIGEN-1S), *Geophys. Res. Lett.*, **29**, 94–97, *DOI*:10.1029/2002*GL*015064. 7

Robertson, F. R., Bosilovich, M. G., Chen, J. & Miller, T. L. (2011). The Effect of Satellite Observing System Changes on MERRA Water and Energy Fluxes, *J. Climate*, **24**, 5197–5217, *DOI*:10.1175/2011*JCLI*4227.1. 40

Röske, F. (2005). *Global oceanic heat and fresh water forcing datasets based on ERA-40 and ERA-15 Reports on Earth System Science, Reports on Earth System Science 13*, Max Planck Institute for Meteorology, URL www.mpimet.mpg.de. 24

Rummel, R., Yi, W. & Stummer, C. (2011). GOCE gravitational gradiometry, *J. Geod.*, **85**, 777–790, *DOI*:10.1007/*s*00190-011-0500-0. 7

Schindelegger, M. & Dobslaw, H. (2016). A global ground trouth view of the lunar air pressure tide L2, *J. Geophys. Res.*, **121**, 95–110, *DOI*:10.1002/2015*JD*024243. 39, 40

Schindelegger, M., Einšpigel, D., Salstein, D. & Böhm, J. (2016). The Global S1 Tide in Earth's Nutation, *Surv. Geophys.*, **37**, 643–680, *DOI*:10.1007/*s*10712-016-9365-3. 40

Schindelegger, M. & Ray, R. D. (2014). Surface Pressure Tide Climatologies Deduced from a Quality-Controlled Network of Barometric Observations, *Mon. Weather Rev.*, **142**, 4872–4889, *DOI*:10.1175/*MWR-D*-14-00217.1. 39, 65

Schindelegger, M., Salstein, D., Einšpigel, D. & Mayerhofer, C. (2017). Diurnal atmosphere-ocean signals in Earth's rotation rate and a possible modulation through ENSO, *Geophys. Res. Lett.*, **44**, 2755–2762, *DOI*:10.1002/2017*GL*072633. 65

Sidorenkov, N. S. (2009). *The Interaction Between Earth's Rotation and Geophysical Processes*, 1–305 p., *DOI*:10.1002/9783527627721, arXiv:1011.1669v3. 41

Sterl, A. (2004). On the (in)homogeneity of reanalysis products, *J. Clim.*, **17**, 3866–3873, *DOI*:10.1175/1520-0442(2004)017<3866:*OTIORP*>2.0.*CO*;2. 40

Swenson, S. & Wahr, J. (2002). Estimated effects of the vertical structure of atmospheric mass on the time-variable geoid, *J. Geophys. Res.*, **107**, *DOI*:10.1029/2000*JB*000024. 14, 15

Swenson, S. C. & Wahr, J. M. (2006). Post-processing removal of correlated errors in GRACE data, *Geophys. Res. Lett.*, **33**, 1–4, *DOI*:10.1029/2005*GL*025285. 65, 66

Tapley, B., Bettadpur, S., Watkins, M. & Reigber, C. (2004). The gravity recovery and climate experiment: Mission overview and early results, *Geophys. Res. Lett.*, **31**, L09,607, *DOI*:10.1029/2004*GL*019920. 7

Thomas, M. & Dobslaw, H. (2004). On the impact of baroclinic ocean dynamics on the Earth's gravity field, in: *Joint CHAMP/GRACE Science Team Meeting, Potsdam*, URL http://gfzpublic.gfz-potsdam.de/pubman/item/escidoc:239639. 9

Thomas, M., Sündermann, J. & Maier-Reimer, E. (2001). Consideration of ocean tides in an OGCM and impacts on subseasonal to decadal polar motion excitation, *Geophys. Res. Lett.*, **28**, 2457–2460, *DOI*:10.1029/2000*GL*012234. 23

Uppala, S., Kallberg, P., Simmons, A., Andrae, U., Bechtold, V. & et al. (2005). The ERA-40 re-analysis, *Q. J. R. Meteorol. Soc.*, **131**, 2961–3012, *DOI*:10.1256/*qj*.04.176. 9, 11

Wahr, J. M., Molenaar, M. & Bryan, F. (1998). Time variability of the Earth's gravity field: Hydrological and oceanic effects and their possible detection using GRACE, *J. Geophys. Res.*, **103**, 30,205, *DOI*:10.1029/98*JB*02844. 14, 18

Wang, H., Wu., P. & Wang, Z. (2006). An approach for spherical harmonic analysis of non-smooth data, *Computer Geosciences*, **32**, 1654–1668, *DOI*:10.1016/*j.cageo*.2006.03.004. 16, 17

Wolff, J.-O., Maier-Reimer, E. & Legutke, S. (1997). *The Hamburg Ocean Primitive Equation Model HOPE*, *Tech. Rep. 13*, URL http://mms.dkrz.de/pdf/klimadaten/models/ReportNo.13.pdf. 23

Wunsch, C. & Stammer, D. (1997). Atmospheric Loading and the Oceanic "Inverted Barometer" Effect, *Rev. Geophys.*, **35**, 79–107, *DOI*:10.1029/96*RG*03037. 13

Yessad, K. (2015). *FULL-POS in the Cycle 41T1 of ARPEGE/IFS*, *Tech. rep.*, Meteo-France, URL http://www.cnrm.meteo.fr/gmapdoc/IMG/pdf/ykfpos41t1.pdf. 11, 12

Appendix A

AOD1B Non-Tidal Coefficients Format Description

Non-tidal AOD1B files are available from the GRACE data repository maintained by GFZ via ftp://isdcftp.gfz-potsdam.de/grace/Level-1B/GFZ/AOD/RL06.

Format and content of the **non-tidal coefficients** of AOD1B are described in the following. The files are updated daily in the GRACE archives by using the GRACE Level-1 filename convention "AOD1B_YYYY-MM-DD_S_RL.EXT.gz" (Case *et al.*, 2002), where "YYYY-MM-DD" is the corresponding date, the GRACE satellite identifier "S" is fixed to X implying that the product is not refering to a particular spacecraft; "RL" is an increasing release number, and EXT is fixed to "asc" indicating that the file is provided in plain text. For data transfer speed-up, the products are gnu-zipped.

Each file consists of a header with a dedicated number of lines (NUMBER OF HEADER RECORDS) and ends with a constant header line (END OF HEADER). The first part of the header is based on the Level-1 instrument product header convention (Case *et al.*, 2002) and gives more general information on the product (header lines PRODUCER AGENCY to PROCESS LEVEL). These lines are followed by a number of header lines describing the de-aliasing product more precisely:

```
PRESSURE TYPE (SP OR VI)        : surface pressure or vertical integration approach
MAXIMUM DEGREE                  : maximum degree of the spherical harmonic series
COEFFICIENT ERRORS (YES/NO)     : yes, if errors are given for each coefficient
COEFF. NORMALIZED (YES/NO)      : yes, if the coefficients are normalized
CONSTANT GM [M^3/S^2]           : GM value used for computation
CONSTANT A [M]                  : semi-major axis value used for computation
CONSTANT FLAT [-]               : flattening value used for computation
CONSTANT OMEGA [RAD/S]          : Earth rotation rate used for computation
NUMBER OF DATA SETS             : number of data fields per product file
DATA FORMAT (N,M,C,S)           : format string to read the data
```

The NUMBER OF DATA SETS is 12 (RL04), 16 (RL05) and 32 (RL06) depending on the temporal resolution and the number of coefficient sets (ATM, OCN, GLO, OBA) considered. The MAXIMUM DEGREE is set to 100 or 180.

The following is an example for a single AOD1B RL06 product file, where for simplification only the two first coefficients of each data set are given:

```
PRODUCER AGENCY                : GFZ
PRODUCER INSTITUTION           : GFZ
FILE TYPE ipAOD1BF             : 999
FILE FORMAT 0=BINARY 1=ASCII   : 1
NUMBER OF HEADER RECORDS       : 30
SOFTWARE VERSION               : atm_ocean_dealise.06
SOFTWARE LINK TIME             : Not Applicable
REFERENCE DOCUMENTATION        : GRACE AOD1B PDD, version 06
SATELLITE NAME                 : GRACE X
SENSOR NAME                    : Not Applicable
TIME EPOCH (GPS TIME)          : 2000-01-01 12:00:00
TIME FIRST OBS(SEC PAST EPOCH): 389102400.000000 (2012-05-01 00:00:00)
TIME LAST OBS(SEC PAST EPOCH) : 389178000.000000 (2012-05-01 21:00:00)
NUMBER OF DATA RECORDS         : 527072
PRODUCT CREATE START TIME(UTC): 2016-07-01 13:52:30
PRODUCT CREATE END TIME(UTC)   : 2016-07-01 13:52:36
FILESIZE (BYTES)               : 21085088
FILENAME                       : AOD1B_2012-05-01_X_06.asc
PROCESS LEVEL (1A OR 1B)       : 1B
PRESSURE TYPE (SP OR VI)       : VI
MAXIMUM DEGREE                 : 180
COEFFICIENT ERRORS (YES/NO)    : NO
COEFF. NORMALIZED (YES/NO)     : YES
CONSTANT GM [M^3/S^2]          :  0.39860044180000E+15
CONSTANT A [M]                 : 0.63781366000000E+07
CONSTANT FLAT [-]              :  0.29825642000000E+03
CONSTANT OMEGA [RAD/S]         : 0.72921150000000E-04
NUMBER OF DATA SETS            : 32
DATA FORMAT (N,M,C,S)          : (2(I3,X),E15.9,X,E15.9)
END OF HEADER
DATA SET 01:   16471 COEFFICIENTS FOR 2012-05-01 00:00:00 OF TYPE atm
  0   0 0.187871629E-10 0.000000000E+00
  1   0 -.179262460E-09 0.000000000E+00
...
DATA SET 02:   16471 COEFFICIENTS FOR 2012-05-01 00:00:00 OF TYPE ocn
  0   0 -.127066233E-14 0.000000000E+00
  1   0 -.347354477E-10 0.000000000E+00
...
DATA SET 03:   16471 COEFFICIENTS FOR 2012-05-01 00:00:00 OF TYPE glo
  0   0 0.187858922E-10 0.000000000E+00
  1   0 -.213997908E-09 0.000000000E+00
...
DATA SET 04:   16471 COEFFICIENTS FOR 2012-05-01 00:00:00 OF TYPE oba
  0   0 0.468956395E-09 0.000000000E+00
  1   0 -.594303481E-10 0.000000000E+00
...
```

Appendix B

AOD1B Tidal Coefficients Format Description

Non-tidal AOD1B files are available from the GRACE data repository maintained by GFZ via ftp://isdcftp.gfz-potsdam.de/grace/Level-1B/GFZ/AOD/RL06/TIDES.

Format and content of the **tidal coefficients** of AOD1B are described in the following. The files are available in the GRACE archives by using the filename convention "AOD1B_DOM_PT_RL.EXT.gz", where "DOM" is "ATM" or "OCN" indicating the spatial domain; "PT" indicates the partial tide according to the Doodson-Warburg convention as discussed in Ch. **??**. "RL" is set to 06 indicating the release number, and "EXT" is fixed to "asc" indicating that the file is provided in plain text.

Each file consists of a header with a dedicated number of lines (NUMBER OF HEADER RECORDS) and ends with a constant header line (END OF HEADER). The first part of the header is based on the level-1 instrument product header convention (Case *et al.*, 2002) and gives more general information on the product (header lines PRODUCER AGENCY to PROCESS LEVEL). These lines are followed by a number of header lines describing the version of the de-aliasing product more precisely:

```
PRESSURE TYPE (ATM or OCN)     : air pressure or sea-water pressure
MAXIMUM DEGREE                 : maximum degree of the spherical harmonic series
COEFFICIENT ERRORS (YES/NO)    : yes, if errors are given for each coefficient
COEFF. NORMALIZED (YES/NO)     : yes, if the coefficients are normalized
CONSTANT GM [M^3/S^2]          : GM value used for computation
CONSTANT A [M]                 : semi-major axis value used for computation
CONSTANT FLAT [-]              : flattening value used for computation
CONSTANT OMEGA [RAD/S]         : Earth rotation rate used for computation
NUMBER OF DATA SETS            : number of data fields per product
DATA FORMAT (N,M,C,S)          : format to read the data (depending on header line)
```

The NUMBER OF DATA SETS is 2 since cos and sin terms are provided separately. The MAXIMUM DEGREE is set to 180.

The following is an example for a single AOD1B product file containing tidal coefficients, where for simplification only the two first coefficients of each data set are given:

```
PRODUCER AGENCY                : GFZ
PRODUCER INSTITUTION           : GFZ
```

```
FILE TYPE ipAOD1BF             : 999
FILE FORMAT 0=BINARY 1=ASCII   : 1
NUMBER OF HEADER RECORDS       : 27
SOFTWARE VERSION               : atm_ocean_dealise.06
SOFTWARE LINK TIME             : Not Applicable
REFERENCE DOCUMENTATION        : GRACE AOD1B PDD, version 06
SATELLITE NAME                 : GRACE X
SENSOR NAME                    : Not Applicable
PARTIAL TIDE                   : K1
TIME FIRST OBS (YEAR START)    : 2007
TIME LAST OBS (YEAR END)       : 2014
NUMBER OF DATA RECORDS         : 32942
FILENAME                       : AOD1B_ATM_K1_06.asc
PROCESS LEVEL (1A OR 1B)       : 1B
PRESSURE TYPE (ATM OR OCN)     : ATM
MAXIMUM DEGREE                 : 180
COEFFICIENT ERRORS (YES/NO)    : NO
COEFF. NORMALIZED (YES/NO)     : YES
CONSTANT GM [M^3/S^2]          :  0.39860044180000E+15
CONSTANT A [M]                 : 0.63781366000000E+07
CONSTANT FLAT [-]              :  0.29825642000000E+03
CONSTANT OMEGA [RAD/S]         : 0.72921150000000E-04
NUMBER OF DATA SETS            : 2
DATA FORMAT (N,M,C,S)          : (2(I3,X),E15.9,X,E15.9)
END OF HEADER
DATA SET 01:   16471 COEFFICIENTS OF TYPE cos
  0   0 -.111112137E-12 0.000000000E+00
  1   0 -.348696653E-11 0.000000000E+00
...
DATA SET 02:   16471 COEFFICIENTS OF TYPE sin
  0   0 0.161679694E-11 0.000000000E+00
  1   0 0.740852733E-12 0.000000000E+00
...
```

Appendix C

Acronyms

AOD1B	Atmosphere and Ocean De-Aliasing Level-1B Product
ECMWF	European Centre for Medium Weather Forecasts
DWD	Deutscher Wetterdienst - German Meteorological Service
GFZ	Deutsches GeoForschungsZentrum - German Research Centre for Geosciences
GRACE	Gravity Recovery And Climate Experiment
HOPE	Hamburg Ocean Primitive Equation Model
IFS	Integrated Forecasting System of the ECMWF
ISDC	Information System and Data Center at GFZ
JPL	Jet Propulsion Laboratory
LSG	Large-Scale Geostrophic Model
NCEP	National Centers for Environmental Prediction
NWP	Numerical Weather Prediction
MPIOM	Max-Planck-Institute for Meteorology Ocean Model
OGCM	Ocean General Circulation Model
OMCT	Ocean Model for Circulation and Tides
PO.DAAC	Physical Oceanography Distributed Active Archive Center at JPL
PPHA	Barotropic ocean model code named after its main developers R. Pacanowski, R. Ponte, N. Hirose, and A. Ali
WMO	World Meteorological Organization